AN INVESTIGATION INTO THE USE OF BALANCE IN OPERATIONAL NUMERICAL WEATHER PREDICTION

David J.J. Devlin

A Thesis Submitted for the Degree of PhD
at the
University of St. Andrews

2011

AN INVESTIGATION INTO THE USE OF BALANCE IN OPERATIONAL NUMERICAL WEATHER PREDICTION

David J.J. Devlin

A thesis submitted for the degree of Doctor of Philosophy at the

University of St Andrews

26th January 2011

Abstract

Presented in this study is a wide-ranging investigation into the use of properties of balance in an operational numerical weather prediction context.

Initially, a joint numerical and observational study is undertaken. We used the Unified Model (UM), the suite of atmospheric and oceanic prediction software used at the UK Met Office (UKMO), to locate symmetric instabilities (SIs), an indicator of imbalanced motion. These are areas of negative Ertel potential vorticity (in the Northern hemisphere) calculated on surfaces of constant potential temperature. Once located, the SIs were compared with satellite and aircraft observational data. As a full three-dimensional calculation of Ertel PV proved outwith the scope of this study we calculated the two-dimensional, vertical component of the absolute vorticity, to assess the inertial stability criterion. We found that at the synoptic scale in the atmosphere, if there existed a symmetric instability, it was dominated by an inertial instability.

With the appropriate observational data, evidence of inertial instability from the vertical component of the absolute vorticity, predicted by the UM was found at $12km$ horizontal grid resolution. Varying the horizontal grid resolution allowed the estimation of a grid length scale, above which, the inertial instability was not captured by the observational data, of approximately $20km$. Independently, aircraft data was used to estimate that horizontal grid resolutions above 20-25km should not model any features of imbalance providing a real world estimate of the

lower bound of the grid resolution that should be employed by a balanced atmospheric prediction model. A further investigation of the UM concluded that the data assimilation scheme and time of initialisation had no effect on the generation of SIs.

An investigation was then made into the robustness of balanced models in the shallow water context, employing the contour-advective semi-Lagrangian (CASL) algorithm, Dritschel & Ambaum (1997), a novel numerical algorithm that exploits the underlying balance observed within a geophysical flow at leading order. Initially two algorithms were considered, which differed by the prognostic variables employed. Each algorithm had their three-time-level semi-implicit time integration scheme de-centred to mirror the time integration scheme of the UM. We found that the version with potential vorticity (PV), divergence and acceleration divergence, $\mathrm{CA}_{\delta,\gamma}$, as prognostic variables preserved the Bolin-Charney balance to a much greater degree than the model with PV, divergence and depth anomaly $\mathrm{CA}_{\tilde{h},\delta}$, as prognostic variables. This demonstrated that $\mathrm{CA}_{\delta,\gamma}$ was better equipped to benefit from de-centring, an essential property of any operational numerical weather prediction (NWP) model.

We then investigate the robustness of $\mathrm{CA}_{\delta,\gamma}$ by simulating flows with Rossby and Froude number $\mathcal{O}(1)$, to find the operational limits of the algorithm. We also investigated increasing the efficiency of $\mathrm{CA}_{\delta,\gamma}$ by increasing the time-step Δt employed while decreasing specific convergence criteria of the algorithm while preserving accuracy. We find that significant efficiency gains are possible for predominantly mid-latitude flows, a necessary step for the use of $\mathrm{CA}_{\delta,\gamma}$ in an operational NWP context.

The study is concluded by employing CASL in the non-hydrostatic context under the Boussinesq approximation, which allows weak stratification to be considered, a step closer to physical reality than the shallow water case. CASL is compared to the primitive equation pseudospectral (PEPS) and vorticity-based pseudospectral (VPS) algorithms, both as the names suggest, spectral-based algorithms, which again differ by the prognostic variables employed. This comparison is drawn to highlight the computational advantages that CASL has over common numerical methods used in many operational forecast centres. We find that CASL requires significantly less artificial numerical diffusion than its pseudospectral counterparts in simulations of Rossby number $\sim \mathcal{O}(1)$. Consequently, CASL obtains a much less diffuse, more accurate solution, at a lower resolution and therefore lower computational cost. At low Rossby number, where the flow is strongly influence by the Earth's rotation, it is found that CASL is the most cost-effective method. In addition, CASL also preserves a much greater proportion of balance, diagnosed with nonlinear quasigeostrophic balance (NQG), another significant advantage over its pseudospectral counterparts.

Acknowledgements

I would like to offer sincere thanks to my supervisor Jean Reinaud who has, over the course of my study, exhibited the patience of a saint and the endurance of an Olympic marathon runner.

Special thanks are also due to David Dritschel and members of the Vortex Dynamics group in St Andrews, past and present, who I have been fortunate to know, and to Mike Cullen and Marek Wlasak at the UK Met Office for giving me a taste of a world outside of St Andrews.

I would also like to thank my partner Nicole Judd for her unwavering support.

Last but not least, I would also like to thank my mother, Sandra Mason, for absolutely everything.

I am grateful to the EPSRC and the UK Met Office for their financial support.

Declaration

I, David James John Devlin, hereby certify that this thesis, which is approximately 40,000 words in length, has been written by me, that it is the record of work carried out by me and that it has not been submitted in any previous application for a higher degree.

I was admitted as a research student in September 2005 and as a candidate for the degree of PhD in September 2005; the higher study for which this is a record was carried out in the University of St Andrews between 2005 and 2009.

Date: .... **Signature of Candidate:**..

I hereby certify that the candidate has fulfilled the conditions of the Resolution and Regulations appropriate for the degree of PhD in the University of St Andrews and that the candidate is qualified to submit this thesis in application for that degree.

Date: .... **Signature of Supervisor:**..

In submitting this thesis to the University of St Andrews we understand that we are giving permission for it to be made available for use in accordance with the regulations of the University Library for the time being in force, subject to any copyright vested in the work not being affected thereby. We also understand that the title and abstract will be published, and that a copy of the work may be made and supplied to any bona fide library or research worker, that my thesis will be electronically accessible for personal or research, and that the library has the right to migrate my thesis into new electronic forms as required to ensure continued access to the thesis. We have obtained any third-party copyright permissions that may be required in order to allow such access and migration.

The following is an agreed request by candidate and supervisor regarding the electronic publication of this thesis:

Access to printed copy and electronic publication of thesis through the University of St Andrews.

Date: ....

Signature of Candidate:..

Signature of Supervisor:..

"Yesterday it thundered, last night it lightened, and at three this morning I saw the sky as red as a city in flames could have made it. I have a leech in a bottle, my dear, that foretells all these prodigies and convulsions of nature: no, not as you will naturally conjecture by articulate utterance of oracular notices, but by a variety of gesticulations, which here I have not room to give account of. Suffice it to say, that no weather change surprises him, and that in point of the earliest and most accurate intelligence, he is worth all the barometers in the world."

William Cowper - Letter to Lady Hesketh,

10th November 1787

Contents

List of Figures

List of Tables

List of symbols

a	arrival point
b	buoyancy
c_p	specific heat of dry air at constant pressure
cf	cloud ice
cl	cloud water
d	departure point, diffusion operator
f	Coriolis frequency
h	depth
$\tilde{h}$	depth perturbation
$\mathbf{k}$	unit vector in the vertical direction
m_X	mixing ratio of moist quantities
n	time-level
(n_x, n_y, n_z)	grid resolution in the x, y and z directions
p	pressure, de-centring parameter
p_h	hydrostatic pressure
p_{nh}	non-hydrostatic pressure
q	shallow water potential vorticity
r	radial distance in spherical coordinates
tol	tolerance
$\mathbf{u} = (u, v, w)$	Eastward, Northward & upward component of velocity field
u_g	zonal geostrophic wind

u_{max}	maximum zonal velocity
va	vapour
x, y, z	Eastward, Northward & upward directions
A	Robert-Asselin filter coefficient
B	Bernoulli pressure
C	Courant number, pseudospectral damping rate
D	Laplacian damping operator
E	energy
F_r	Froude number
H	mean depth
J	Jacobian
$\mathbf{L}$	general linear term
(L_x, L_y, L_z)	domain length in the x, y and z dimensions
M	surface of absolute momentum
$\mathbf{N}$	general non-linear term
N	Brunt-Väisälä frequency
P	physical parameterisations
Q	quasigeostrophic potential vorticity
R	universal gas constant
R_{dry}	universal gas constant for dry air
R_o	Rossby number
R_{va}	gas constant for vapour
T	temperature
T_V	virtual temperature
$\mathbf{X}$	general position term
Δ	horizontal grid spacing
Π	Exner pressure, Ertel potential vorticity

Π'	Exner pressure increment
Π_θ	isentropic Ertel potential vorticity
Υ	general field
Φ	geopotential
Ξ	Bolin-Charney balance variable
$\boldsymbol{\varphi} = (\boldsymbol{\varphi}_h, \phi)$.	vector potential
α	time-weighting coefficient, specific volume, perturbation angle
β	northward gradient of Coriolis frequency
γ	acceleration divergence
δ	divergence
ϵ	ratio of gas constant of dry air to gas constant of vapour
ζ_θ	vertical vorticity component evaluated on isentropic surface
θ	potential temperature
θ_V	virtual potential temperature
κ	ratio of gas constant to specific heat at constant pressure
λ	longitude, Eastward
ν	diffusion coefficient
ρ	density
ρ_{dry}	density (dry)
ρ_0	mean background density
ρ'	density anomaly
$\bar{\rho}$	mean linear density
ϕ	latitude, Northward
χ	velocity potential
ψ	streamfunction
$\omega = (\xi, \eta, \zeta)$	vorticity
∇	directional derivative
∇_h	horizontal directional derivative

∇^2	Laplacian operator
ϖ	non-hydrostatic PV anomaly
$\mathcal{A}_h$	ageostrophic, non-hydrostatic vorticity
$\mathcal{D}$	isopycnal displacement
$\mathcal{L}_{qg}$	linear quasigeostrophic operator

Characteristic scales

B	buoyancy
f_0	Coriolis frequency
H	vertical length
N_0	Brunt-Väisälä frequency
L	horizontal length
P	pressure
T	time
U	horizontal velocity
W	vertical velocity

Units

E	East
GHz	gigahertz
K	Kelvin
kg	kilogram
km	kilometre
m	metre
N	North
s	seconds
t	time
W	West

Constants

a	mean radius of the Earth (6.37 x $10^6 m$)
g	gravitational acceleration at sea-level ($9.81 ms^{-2}$)
p_0	standard pressure at sea-level ($1013.25 hPa$)
R	universal gas constant (8.314 x $10^3 JK^{-1} kmol^{-1}$)
R_{dry}	gas constant for dry air ($287 JK^{-1} kg^{-1}$)
Ω	planetary rotation rate (7.292 x $10^{-5} rads^{-1}$)

Abbreviations

4D-VAR	four dimensional variational assimilation
AC	analysis correction
BADC	British atmospheric data centre
C-SIP	convective storm initiation project
CASL	contour-advective semi-Lagrangian
CPU	central processing unit
ECMWF	European centre for medium-range weather forecasting
FAAM	facility for airborne atmospheric measurement
FASTEX	fronts and Atlantic storm tracking experiment
FFT	fast Fourier transform
IAU	incremental analysis updating
IGW	inertia-gravity wave
JMA	Japanese meteorological agency
LAM	limited area model
MAP	mesoscale alpine project
MetDB	Met Office observational database
MODIS	moderate resolution imaging spectroradiometer
MSG	Meteosat second generation (satellite)

NAE	North Atlantic and European
NHD	non-hydrostatic deep (set of equations)
NQG	non-linear quasi-geostrophic
NWP	numerical weather prediction
PEPS	primitive equation pseudospectral
PV	potential vorticity
PVU	potential vorticity unit
RAF	royal air force
SAE	spontaneous-adjustment emission
SI	symmetric instability
TM	trademark
VPS	vorticity-based pseudospectral
UK	United Kingdom
UKMO	United Kingdom Meteorological Office
UM	Unified Model
UTC	coordinated universal time
VPS	vorticity-based pseudospectral

Chapter 1

Introduction

1.1 Motivation

The set of all the phenomena in the Earth's atmosphere at any given time, including days into the future, is commonly referred to as the weather. Over longer periods of time, ranging from months to decades, these same phenomena can be averaged out. These averaged motions are generally referred to as the Earth's climate.

The weather influences the lives of almost everybody on Earth, on a daily basis, directly and indirectly. Therefore, it is natural to wish to know what the weather will be like in the future, be it the rock-climber who wishes to avoid possible life or death conditions when climbing, or the individual who wishes to know if they should take an umbrella outside with them while they walk the dog. Industry, transport, government, health and defence are sectors which have a vested interest in accurate weather and climate prediction. The movement of people and goods around the globe is affected by the weather and in some extreme circumstances the weather can tragically be a killer. Crops grown in different parts of the globe have been chosen to suit certain climates. Unusual weather conditions can affect productivity and will have greater economic impact in underdeveloped regions.

Currently, there is great debate in both the scientific and non-scientific communities about how the Earth's climate will change in the decades to come and what impact this will have on the lives of future generations. Scientific models that predict future climates offer the best hope for providing the information that will allow the world's policy-makers to make informed decisions on the future of the Earth. Most people are aware that the Earth's climate is undergoing changes, almost certainly due to man-made effects/influence. A key question for the future of the planet is how the Earth will react to increasing levels of carbon dioxide in the atmosphere.

During the eruption of the Eyjafjallajökull volcano in Iceland in March and April 2010, the weather of Northern Europe proved hazardous to people due to ash particles in the air and placed restrictions on aircraft flight paths, grounding many flights. Prediction models were able to assess where the ash cloud would disperse to and what the intensity would be. There can be little doubt that this knowledge helped to save lives and prevent unnecessary risk.

Very few individuals have the ability to produce their own weather or climate forecasts. A first port of call is usually a forecasting agency. At such an agency, the UK Met Office (UKMO), the same short-range prediction models are employed to study the long-term climate of the Earth.

Currently, the majority of conventional prediction models use so-called spectral-based methods. Forecast centres that employ these methods include the European centre for medium-range weather forecasting (ECMWF), Persson & Grazzini (2005), which is generally recognised as one of, if not the top performing numerical weather prediction (NWP) centre in the world. Another is the Japanese meteorological agency (JMA), home of the 'Earth Simulator 2' which achieves very high resolution in it's global prediction models. Although these models are invaluable, there is always room for improvement, to allow better decision making for the individual and the collective good.

Prediction models will always become more efficient as the computing resources available increase, giving an equivalent degree of accuracy in less time. Another avenue available for increased efficiency is to improve the numerical methods used and the assumptions that motivate them. This is the main theme of this thesis, the investigation of such an assumption, namely that geophysical flows are close to *balance*, and how models constructed under this assumption can potentially improve the efficiency of prediction models in an operational NWP context.

Key to the understanding of NWP is the notion of what a geophysical fluid is and this is outlined in the next section.

1.2 Geophysical flows

One of the major challenges when constructing a numerical model with which to simulate geophysical flows is the differing spatial and temporal scales that coexist in the motions of the atmosphere and ocean. Any modeller concerned with such flows should attempt to model the dominant large-scale motion correctly before any other.

Geophysical flows are constrained by two features: the Earth's rotation and the overall stable density stratification of the flow. Rotation alone tends to form columnar vortices with negligible vertical variation, like cigars, known as Taylor columns, Taylor (1923) and Proudman (1916). On the other hand, stratification tends to order the flow into two-dimensional horizontal layers, like pancakes, exhibiting relatively weak vertical velocities, Taylor (1923) and Proudman (1916).

The impact of rotation and stratification on a geophysical flow can be parameterised by the Rossby and Froude numbers where

$$Ro = \frac{U}{fL}, \quad Fr = \frac{U}{\sqrt{gH}}, \tag{1.1}$$

where U, L and H are the characteristic velocity, length and depth scales of the flow, f is the Coriolis parameter and g is the acceleration due to gravity.

A scale analysis reveals typical mid-latitude values of Ro, Fr to be approximately 0.1 and 0.01 in the atmosphere and ocean respectively Pedlosky (2004), and Vallis (2006).

1.3 Balance

A defining characteristic of geophysical flows is the interaction between different phenomena, characterised by differing spatial and temporal scales. In geophysical flows interaction occurs principally between low frequency vortical-based motions and the relatively higher frequency inertia-gravity waves (IGWs). An example of each type of motion is shown in figure 1.1.

Although these two types of motion are fundamentally different they are observed to co-exist and interact. In fact, vortical motions are thought to generate IGWs by 'spontaneous-adjustment emission' (SAE), Ford *et al.* (2000), Dritschel & Vanneste (2006).

The concept of balance arises from the observation that large-scale geophysical flows are dominated by vortical motions. This allows the simplification of the equations that describe the evolution of the balanced component of the flow. Computationally, these simplified equations are solved much more efficiently. Therefore, balanced models are of practical interest to meteorologists, particularly in weather forecasting as vortical motions can be more accurately simulated

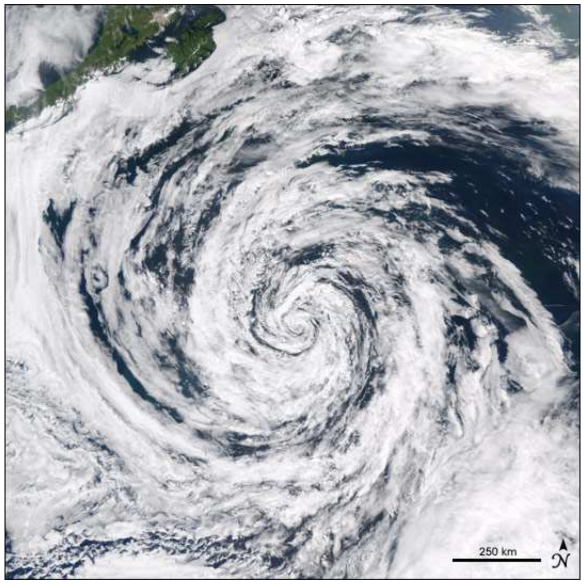

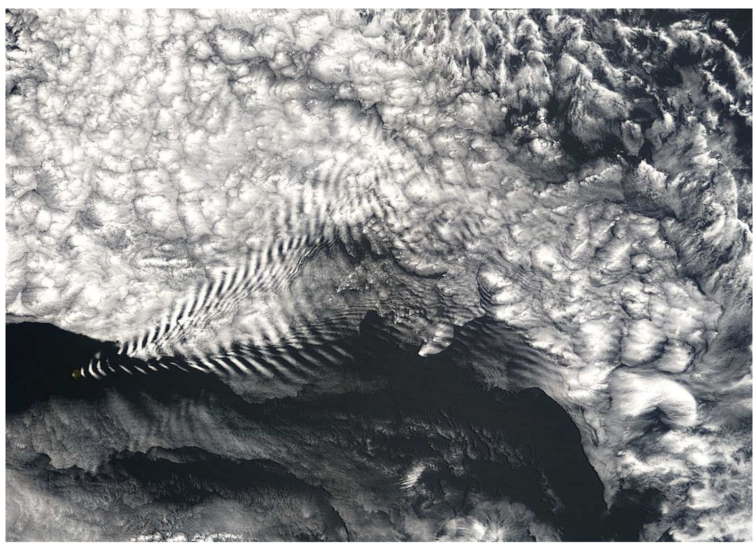

Figure 1.1: Examples of the two main types of motion observed in geophysical flows. *Top*: a large low pressure system spinning in the Gulf of Alaska, on Aug 17 2004. *Bottom* an example of orographic forcing to create a wave pattern by the flow of air over and around Amsterdam Island in the Indian Ocean, captured Dec 19 2005. Both images are from the MODIS (moderate resolution imaging spectroradiometer) instrument and available at http://visibleearth.nasa.gov .

than the IGWs. In NWP, IGWs contribute what is mostly considered to be 'noise' to the numerical solution and are a potentially catastrophic source of numerical contamination to forecasts.

Mathematically, balance implies that a single scalar master variable controls the evolution of the flow with a set of diagnostic balance relations that calculate the imbalanced variables. This control is defined through the balance relations, the most common of which are geostrophic and hydrostatic balance which respectively equate the horizontal pressure gradient to the Coriolis acceleration and the vertical pressure gradient to the buoyancy. These balances are observed to hold approximately in the atmosphere. It is possible to use other balance relations to define balance, depending on the regime of interest, Mohebalhojeh & Dritschel (2001).

While there exists a need to suppress the false generation of IGWs the mathematical justification of balance is not straightforward. In practice there are limits to what extent ideas of balance can be relied upon when attempting to describe a geophysical flow. Observations and numerical simulations both demonstrate that balance will break down with the spontaneous emission of IGWs. In the shallow water context, Leith (1980), introduced the concept of a 'slow manifold', a set of solutions that do not contain IGWs. The theory was that if a flow was initialised within this slow manifold then the solutions would remain in this slow manifold for all time. Evidence from Ford (1994), Ford *et al.* (2000), Dritschel & Vanneste (2006), suggests that such a manifold almost certainly does not exist and that the effects of the imbalanced motion on the flow are negligible but potentially disastrous numerically. This means that there are limitations to the long-term suitability of balanced models in an operational NWP context.

1.3.1 Potential vorticity

A master variable relating to vortical motions which controls the large-scale evolution of a geophysical flow is the potential vorticity (PV), which is materially invariant for inviscid, adiabatic flows. In conjunction with appropriate balance relations, PV can be 'inverted' to find the instantaneous velocity, buoyancy, temperature and pressure fields, more commonly known as PV inversion, Hoskins *et al.* (1985), McIntyre & Norton (2000). Thus PV has the important property that all the significant dynamical information of the flow is contained within it.

A statement of PV was first derived by Ertel in 1942, denoted by Π,

$$\Pi = \frac{\zeta^a}{\rho} \cdot \nabla\theta, \tag{1.2}$$

where ρ is the fluid density, ζ^a is the absolute vorticity and θ is the potential temperature. In the absence of friction and diabatic effects PV is conserved materially within the flow with

$$\frac{D\Pi}{Dt} \equiv \frac{\partial\Pi}{\partial t} + \mathbf{u} \cdot \nabla\Pi = 0, \tag{1.3}$$

which means that for a parcel of fluid within a flow, PV will be unchanged as the parcel moves and deforms with the flow, a very useful property.

As the flow can be described by the evolution of this single equation, (1.3), coupled with the appropriate diagnostic imbalance relations, the resulting system of equations becomes much more simple to solve.

1.4 Numerical simulation of a balanced flow

The basic idea of numerical weather prediction (NWP) is to sample the state of a geophysical flow at a given time and use the equations of thermo- and fluid dynamics to estimate the state of the flow at some time in the future. The equations are non-linear and are, in general, impossible to solve exactly. However, different numerical methods allow approximate solutions to be generated with certain desirable properties.

At field-leading institutions like the UKMO the resolutions available in their operational prediction models are many orders of magnitude coarser than those required to solve the equations accurately. Gill (1982) estimates that a horizontal grid size of the order of $1mm$ would be required to adequately capture all scales of motion present in the atmosphere and oceans. As a compromise, the equations are averaged in space and time and one hopes that the numerical solution approximates the averaged solution of the equations. Within this averaging, IGW motions that cannot be resolved in space are damped artificially and their effects are parameterised within the model. The problem with this compromise is that these effects can be harmful due to the non-selectiveness of the parametrisation scheme.

The geometry of geophysical flows is shallow. The atmosphere has a horizontal scale of hundreds of thousands of kilometres and a vertical scale of tens of kilometres. Therefore, a natural place to investigate to what extent fluid motion can be described by balanced flow is the shallow water equations, the simplest set of equations describing a geophysical flow that permits IGWs as a mode of solution.

The shallow water equations can be re-formulated to take account of the leading order scale separation between vortical-based and IGW motion. This separation is by no means exact, but the dominance of the vortical, balanced component of the flow suggests that this is a valid assumption to make.

We also consider the non-hydrostatic model under the Boussinesq approximation which differs from the shallow water model by allowing accelerations in the vertical direction. This model is also a balanced model.

The numerical techniques employed to solve these models also plays a role in the accurate representation of the balanced component of the flow. Many numerical techniques mis-represent the balanced component of the flow by not treating the imbalanced component adequately.

This research is undertaken to examine the robustness of methods employed in the numerical modelling of geophysical flows. New contour-advective based numerical methods developed recently have been demonstrated to benefit the accuracy of balanced and unbalanced components of a geophysical flow. These methods employ a transformation of prognostic variables so that a greater amount of each component is captured.

1.5 Overview

This thesis will be organised as follows. In chapter §2 we introduce the governing equations for the models that will be used in this study. These are the suite of atmospheric and oceanic prediction software used at the UK Met Office (UKMO) known as the Unified Model (UM), the shallow water model and the non-hydrostatic model under the Boussinesq approximation. Also provided in this chapter are details of the numerical methods used in the solution of these models.

Chapter §3 presents the results of an joint observational and numerical study aimed at investigating at what scale in the atmosphere features of imbalance manifest. This allows the estimation of the horizontal scales balanced models of the atmosphere may be valid on. In addition, a study of the UM is undertaken to assess what role, if any, the UM plays in generating features of imbalance, spurious or otherwise.

Chapter §4 then looks at an example of a balanced model, the shallow water model, solved by contour-advective semi-Lagrangian (CASL) algorithm, with two different sets of prognostic variables. We investigate de-centring the three-time-level semi-implicit time integration scheme in anticipation of potential use in an operational NWP context. A further general investigation is made of the Rossby and Froude number parameter space to assess the practical operational limits of CASL.

As chapter §4 considers a barotropic atmosphere chapter §5 presents CASL employed in a baroclinic atmosphere, specifically the non-hydrostatic model under the Boussinesq approximation. Simulations are undertaken that compare CASL to two similar pseudospectral algorithms. The value of this comparison comes from the fact that spectral-based methods in general are used by a number of operational numerical weather prediction centres around the world.

Conclusions are drawn and further work is discussed in chapter §6.

Chapter 2

Mathematical formulation and numerical methodology

2.1 Introduction

In this chapter the governing equations for a geophysical fluid are introduced. Details of the full non-balanced equations of the UM are provided. Furthermore, the simplifications of the Navier-Stokes equations that are required to obtain the barotropic, shallow water model and the baroclinic, non-hydrostatic model under the Boussinesq approximation are outlined. We then discuss the reformulation of the shallow water and non-hydrostatic equations to obtain prognostic variables that better distinguish between the different scales of motions that co-exist in geophysical flows.

In section §2.4 we outline a normal-mode analysis of the shallow water equations to illustrate the frequency separation that distinguishes vortical and IGW components of the flow.

We also outline the numerical methods used to solve each of the models that have been introduced.

2.2 The Unified Model

2.2.1 Governing equations

The Unified Model (UM) is the name given to the suite of atmospheric and oceanic modelling software developed and used at the UK Meteorological Office (UKMO). A complete and comprehensive description of the UM from the continuous equations of the dynamical core to the finite difference schemes and techniques used in the numerical integration of those equations is provided in Staniforth *et al.* (2006). A condensed version of that document can be found in Davis *et al.* (2005).

Following Davis *et al.* (2005), the governing equations, namely, the compressible Euler equations, mass conservation equation, the first law of thermodynamics and the equation of state are

$$\frac{D\mathbf{u}}{Dt} + 2\mathbf{\Omega} \times \mathbf{u} + c_p\theta_V \nabla\Pi + g\mathbf{r} = P^{\mathbf{u}}, \tag{2.1a}$$

$$\frac{\partial \rho_{dry}}{\partial t} + \nabla \cdot (\rho_{dry}\mathbf{u}) = 0, \tag{2.1b}$$

$$\frac{D\theta}{Dt} = P^{\theta}, \tag{2.1c}$$

$$\frac{Dm_X}{Dt} = P^{m}, \tag{2.1d}$$

$$\kappa\Pi\theta_V\rho = \tfrac{p}{c_p}, \tag{2.1e}$$

where the three-dimensional velocity $\mathbf{u} = (u, v, w)$, density (dry) ρ_{dry}, Exner pressure Π, potential temperature θ, and the mixing ratios of moist quantities m_X, where

$$m_X = \frac{\rho_X}{\rho_{dry}}, \tag{2.2}$$

are the prognostic variables of the UM. In m_X, the subscript X denotes certain phases of water, namely, vapour (va), cloud water (cl) and cloud ice (cf). c_p is the specific heat of air at constant pressure and R is the universal gas constant with $\kappa = R/c_p \approx 0.286$. Pressure and density are denoted by p and ρ respectively. Here, ρ takes the form $\rho = \rho_{dry}(1+m_{va}+m_{cl}+m_{cf})$. Exner pressure is defined as $\Pi = (p/p_0)^\kappa$ where $p_0 = 1013.25Pa$ is a reference pressure. Potential temperature is defined as $\theta \equiv T/\Pi$ where T is the temperature. When moisture effects are taken into account, the virtual potential temperature is $\theta_V \equiv T_V/\Pi$, with

$$T_V = T\left(\frac{1+m_{va}/\epsilon}{1+m_{va}+m_{cl}+m_{cf}}\right), \tag{2.3}$$

where $\epsilon \equiv R_{dry}/R_{va}(\cong 0.622)$ where R_{dry} and R_{va} are the gas constants for dry air and vapour respectively.

In (2.1), the P terms represents physical parametrisations within the UM. These cover physical processes that manifest on the sub-grid scale. Typical examples are turbulence within the boundary layer and convective processes. P terms also represent ancillary fields within the UM, for example, the effects of orography, hydrology and the land-sea mask, which contains the proportion of land within a grid box. Equations (2.1) are solved in a spherical polar coordinate system (λ,ϕ,r) with the origin at the centre of the Earth. They are written in a reference frame rotating with the Earth's angular velocity Ω. The material derivative $D/Dt \equiv \partial/\partial t + \mathbf{u}\cdot\nabla$ and $\mathbf{r}$ is the unit vector in the radial direction.

The system of governing equations of the UM was chosen to avoid unnecessary approximations and to conserve key quantities such as energy, dry mass, momentum, potential temperature, potential vorticity and moisture. Adhering to this criteria, the governing equations are fully compressible, non-hydrostatic, with a height-based terrain-following vertical coordinate. A deep-atmosphere formulation is also made which affords a full representation of the Coriolis force in the momentum equations. The only approximation made to the governing equations is the spherical geopotential approximation with gravitational acceleration g, acting normal to geopotential (spherical) surfaces. At the time of formulation, the only known form of the fully compressible formulation that fulfilled this criteria was the so-called non-hydrostatic deep (NHD) equations. A fuller discussion of this system of equations can be found in White *et al.* (2005).

2.2.2 Key numerics

Equations (2.1) are discretised horizontally on a staggered Arakawa C-grid, Arakawa & Lamb (1977). This grid choice represents the geostrophic adjustment process well and is predisposed to work better than other grids with semi-implicit time integration schemes. In the vertical a Charney-Phillips grid, Arakawa & Konor (1996), is used with irregular spacing to allow a higher grid resolution near the Earth's surface. A terrain-following vertical coordinate allows lower boundary conditions to be applied relatively easily. As the height of the coordinate surfaces increase they tend to flatten out so that upper level surfaces become horizontal. Figure 2.1 shows the UM grid staggerings. This figure is reproduced from appendix D of Bannister & Cullen (2006).

Again, following Davies *et al.* (2005), the general form of a prognostic equation from (2.1) is

$$\frac{D\mathbf{X}(\mathbf{x},t)}{Dt} = \mathbf{L}(\mathbf{x},t,\mathbf{X}) + \mathbf{N}(\mathbf{x},t,\mathbf{X}), \tag{2.4}$$

where $\mathbf{X}$ is any prognostic variable. $\mathbf{L}$ and $\mathbf{N}$ represent the linear and non-linear terms in $\mathbf{X}$, $\mathbf{x}$ and t represent position and time respectively. A two-time-level semi-implicit semi-Lagrangian time integration scheme is employed by the dynamical core of the UM to solve these equations. Applied to (2.1) they take the form

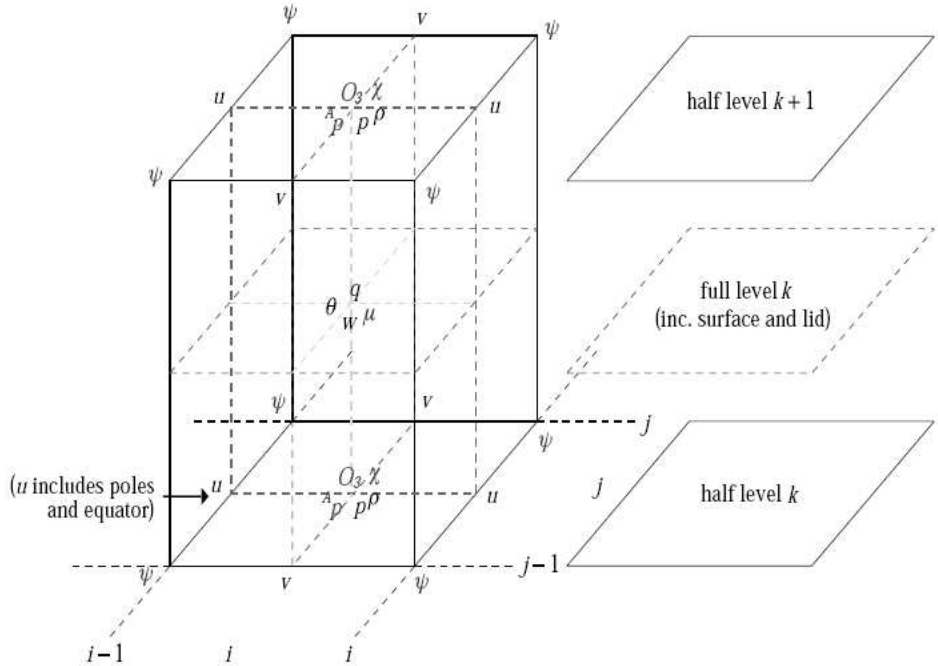

Figure 2.1: Grid staggering of the Unified Model: Arakawa C-grid horizontally and Charney-Phillips vertically. Reproduced from appendix D of Bannister & Cullen (2006).

$$\frac{\mathbf{X}^{n+1} - \mathbf{X}_d^n}{\Delta t} = \alpha(\mathbf{L}(\mathbf{X}^{n+1}) + \mathbf{N}(\mathbf{X}^{n+1})) + (1-\alpha)(\mathbf{L}+\mathbf{N})_d^n, \tag{2.5}$$

where n is the time-level, Δt is the time step, subscript d denotes evaluation at the departure point and α is a time-weighting coefficient.

The interpolation used to locate the departure point, which is generally not on a grid point, is quintic for moisture variables and cubic for all other variables. A graphic representation is given in figure 2.2. The time integration scheme is second-order accurate, $\mathcal{O}(\Delta t^2)$, if $\alpha = 1/2$ and is referred to as centred. When $\alpha \neq 1/2$ the time integration scheme is first-order accurate, $\mathcal{O}(\Delta t)$, and is referred to as off-centred, un-centred or de-centred. α is assigned a value based on which term it is associated, according to different behaviours of the flow. Equation (2.5)

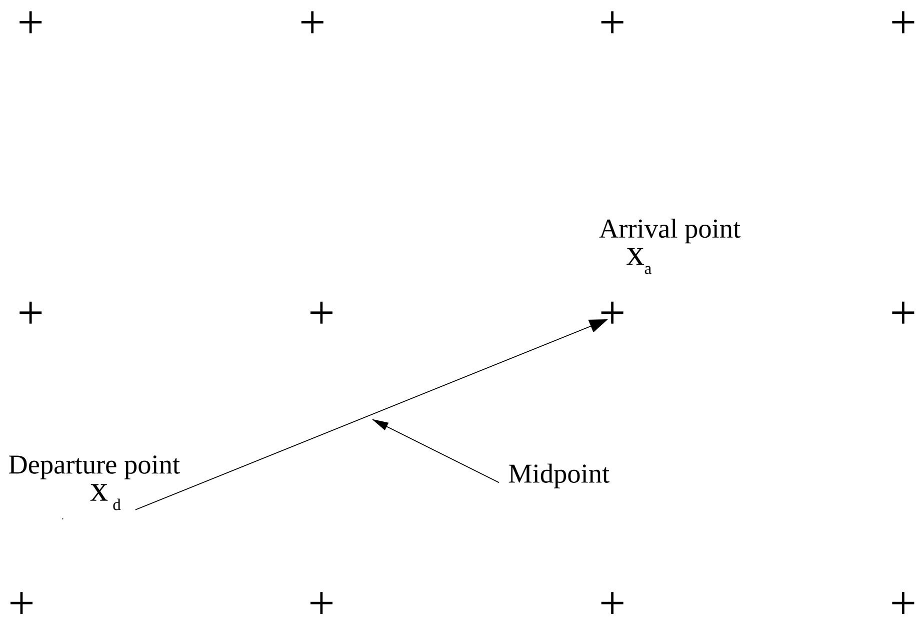

Figure 2.2: A two-dimensional representation of departure and arrival points for the integration scheme. The arrival point $\mathbf{X}_a$ is always a grid point while the departure point $\mathbf{X}_d$ is not in general. The available gridded data is used to locate $\mathbf{X}_d$ and interpolate the advected fields to it. Note that the parcel is displaced between $\mathbf{X}_d$ and $\mathbf{X}_a$ in a time Δt.

can be re-expressed as

$$\mathbf{X}^{n+1} - \alpha \Delta t \mathbf{L}(\mathbf{X}^{n+1}) = [\mathbf{X} + (1-\alpha)\Delta t(\mathbf{L} + \mathbf{N})]_d^n + \alpha \Delta t \mathbf{N}(\mathbf{X}^{n+1}). \tag{2.6}$$

An equation of this form needs to be solved for each prognostic variable (apart from ρ_{dry} which is solved by an *Eulerian* semi-implicit scheme to enforce exact mass conservation). Equation (2.6) cannot be solved easily due to the non-linear term on the right-hand-side that is required at time-level $n+1$. A solution is found by reducing the non-linear implicit coupling and then deriving an elliptic boundary value problem. To do this a predictor-corrector scheme is used. The predictor step uses values at time level n, where values from time-level $n+1$ are required, so the initial approximation to $\mathbf{X}$ is

$$\mathbf{X}^{(1)} = \mathbf{X}_d^n + (1-\alpha)\Delta t(\mathbf{L}+\mathbf{N})_d^n + \alpha\Delta t\mathbf{L}^n + \alpha\Delta t\mathbf{N}^n, \tag{2.7}$$

where the superscript value in brackets denotes the estimate. The corrector step then uses this initial approximation for the full calculation of (2.6) by

$$\mathbf{X}^{n+1} - \alpha\Delta t\mathbf{L}(\mathbf{X}^{n+1}) = [\mathbf{X} + (1-\alpha)\Delta t(\mathbf{L}+\mathbf{N})]_d^n + \alpha\Delta t\mathbf{N}(\mathbf{X}^{(\mathbf{1})}). \tag{2.8}$$

After the predictor-corrector step has been implemented on each prognostic equation, a linear, coupled set of implicit equations result. A solution is found by forming a single elliptic equation, of Helmholtz type, which is solved iteratively, for an unknown pressure increment Π'. At this stage the density (dry) ρ_{dry} at the evaluation time level $n+1$ can be found. Conservation of moisture mixing quantities, potential temperature and momentum can then be achieved by a high order Priestley scheme, Priestley (1993). From this point, prognostic variables at time-level $n+1$ can readily be found.

Formulation of the governing equations of the UM is fully compressible, so acoustic waves in the solution have to be considered. As the time integration scheme is semi-implicit, restrictive time-steps associated with acoustic modes can be overcome to allow adequate modelling of relatively lower frequency motions associated with meteorological features of interest.

A sensible, stable time-step is determined by setting the Courant number $C \equiv U\Delta t/\Delta \simeq 0.3$ where U=$10ms^{-1}$ is the typical flow speed and Δ is a measure of grid size. This results in a Δt of $30s$ and $9000s$ at $1km$ and $300km$ horizontal grid resolution respectively.

As the UM is a grid point model with a longitude-latitude grid in the horizontal direction the same code can be used to run a limited-area model (LAM) anywhere on the globe. The spherical polar coordinate system can be rotated with the equator coinciding with the target area to give as uniform a grid as possible over the area of the LAM.

In this research the atmospheric prediction component of the UM is employed. Table 2.1 outlines details of the two components of the UM used in this investigation. They are the global model, and a LAM, the North Atlantic and European (NAE) model. [Henceforth, the global and NAE components of the UM will be referred to as the global model and the NAE.] The domain of the NAE is shown in figure 2.3. The use of these components of the UM allows investigation of part of the atmosphere at two different horizontal resolutions, $40km$ and $12km$ allowing the evaluation of atmospheric flows at different horizontal resolutions.

Version	Grid spacing	no. x-nodes	no. y-nodes	Vert lvls	Δt
Global	$40km$	640	481	50	$15min$
NAE	$12km$	600	360	38	$5min$

Table 2.1: Technical details of the global and NAE components of the UM.

2.3 The shallow water model

The shallow water equations describe a thin layer of barotropic fluid in hydrostatic balance, that may or may not be rotating, bounded from below by a rigid surface and above by a free surface. The name derives from the assumption that the typical length scale of the fluid being considered is much greater than the typical height scale. It is one of the most useful basic models in geophysical fluid dynamics due to modes of solution containing both slow and relatively fast components.

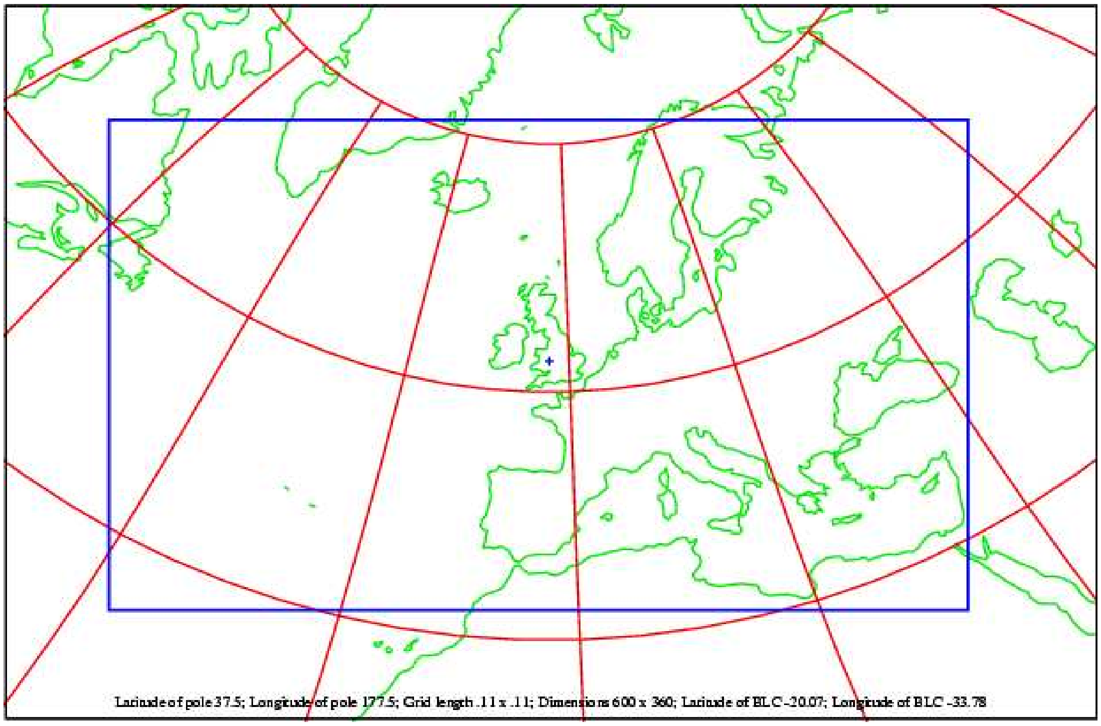

Figure 2.3: Domain of the NAE component of the UM.

The derivation of the shallow water equations is covered extensively in text-books such as Gill (1982), Pedlosky (2004) and Vallis (2006) and many others. As such, only a broad outline of the derivation is presented here.

The assumption of incompressibility and constant density removes thermodynamic considerations from the model and the statement of mass conservation (cf. (2.1b)) is just the isochoric condition:

$$\nabla \cdot \mathbf{u} = 0, \tag{2.9}$$

where $\mathbf{u} \equiv (u, v, w)$ is the velocity. The expression of conservation of momentum (cf. (2.1a) is

$$\frac{D\mathbf{u}}{Dt} + 2\Omega \times \mathbf{u} = -\frac{1}{\rho}\nabla p + \nabla\Phi, \tag{2.10}$$

where $D/Dt \equiv \partial/\partial t + \mathbf{u} \cdot \nabla$, is the material derivative, ρ is the density, p is the pressure and Φ is the geopotential which expresses the combined effects of the centripetal acceleration and gravity. The surface of the sphere is a good approximation to a surface of constant Φ, so here $\nabla\Phi \equiv (0, 0, -g)$.

Equations (2.9) and (2.10) will be the basis for modelling a thin layer of fluid on the sphere and can be more commonly identified as the incompressible Navier-Stokes equations. For simplicity it is common to express (2.10) in local Cartesian coordinates, White (2002) gives more detail on the full spherical shallow water equations. In local Cartesian coordinates the components of (2.10) are

$$\frac{Du}{Dt} + 2\Omega(w\cos\phi - v\sin\phi) = -\frac{1}{\rho}\frac{\partial p}{\partial x}, \tag{2.11a}$$

$$\frac{Dv}{Dt} + 2\Omega u\sin\phi = -\frac{1}{\rho}\frac{\partial p}{\partial y}, \tag{2.11b}$$

$$\frac{Dw}{Dt} + 2\Omega u\cos\phi = -\frac{1}{\rho}\frac{\partial p}{\partial z} - g. \tag{2.11c}$$

It is noted that $2\Omega u\cos\phi$, from (2.11c), from the horizontal variation of Ω is negligible. For energy conservation considerations the corresponding $2\Omega w\cos\phi$ term in (2.11a) must also be neglected, White (2002). A scale analysis of (2.11c) reveals that the vertical and Coriolis acceleration terms are small compared to the pressure gradient and gravitational acceleration. The result is the hydrostatic approximation

$$\frac{1}{\rho}\frac{\partial p}{\partial z} = -g. \tag{2.12}$$

Equation (2.12) can be integrated vertically from the bottom to the top of the fluid, $z = 0$ to $z = h$ to obtain

$$p(z) = \rho g(h - z) + p_0, \tag{2.13}$$

with the boundary condition $p(x, y, h) = p_0$. Differentiating (2.13) with respect to x and y gives

$$\begin{aligned} \frac{\partial p}{\partial x} &= \rho g \frac{\partial h}{\partial x}, && (2.14a) \\ \frac{\partial p}{\partial y} &= \rho g \frac{\partial h}{\partial y}. && (2.14b) \end{aligned}$$

These relations imply that the horizontal pressure gradients are independent of z. Substituting (2.14a) and (2.14b) into the horizontal momentum equations (2.11a) and (2.11b) gives

$$\begin{aligned} \frac{Du}{Dt} - fv &= -g \frac{\partial h}{\partial x}, && (2.15a) \\ \frac{Dv}{Dt} + fu &= -g \frac{\partial h}{\partial y}, && (2.15b) \end{aligned}$$

where $f = 2\Omega \sin \phi$ is the Coriolis parameter.

A scale analysis of (2.15a) and (2.15b) reveal that the horizontal acceleration terms are small compared to the horizontal pressure gradients and Coriolis acceleration terms. The result is the geostrophic approximation

$$\begin{aligned} -fv &= -g \frac{\partial h}{\partial x}, && (2.16a) \\ fu &= -g \frac{\partial h}{\partial y}. && (2.16b) \end{aligned}$$

Vertically integrating the incompressibility condition, (2.9) from the lower boundary, $z = 0$ to the height of the fluid $z = h$, gives

$$h\left(\frac{\partial u}{\partial x} + \frac{\partial v}{\partial y}\right) + w(h) - w(0) = 0. \qquad (2.17)$$

The vertical velocity at the lower boundary $w(0) = 0$ as the velocity normal to the boundary must be zero by the no slip condition. At the free surface the velocity is just the change in h in time, $w(h) = Dh/Dt$, giving

$$h(\nabla \cdot \mathbf{u}) + \frac{Dh}{Dt} = 0, \tag{2.18}$$

which can be re-expressed in vector form as

$$\frac{\partial h}{\partial t} + \nabla \cdot (h\mathbf{u}) = 0. \tag{2.19}$$

Similarly, the horizontal momentum equations (2.11a) and (2.11b) can be expressed in vector form as

$$\frac{D\mathbf{u}}{Dt} + f\mathbf{k} \times \mathbf{u} = g\nabla h. \tag{2.20}$$

Equations (2.19) and (2.20) are commonly known as the shallow water equations with prognostic variables $(\mathbf{u}, h)$, the horizontal velocity components and the depth.

2.4 Normal mode analysis

Following Cullen (2006), a linear analysis of the shallow water equations is outlined to demonstrate the modes of solution and the associated frequency separation. This is done by introducing relatively small sinusoidal disturbances to the basic state of the flow so that the stability of the flow can be investigated. Formally, we seek general solutions of (2.19) and (2.20) of the form

$$u = u', \quad v = v', \quad h = H + h'. \tag{2.21}$$

where H is the mean height of the fluid and the primes denote a small perturbation from the mean. Primed quantities that are non-linear are disregarded leaving the set of linearised equations as

$$\frac{\partial u'}{\partial t} + g\frac{\partial h'}{\partial x} - fv' = 0, \tag{2.22a}$$

$$\frac{\partial v'}{\partial t} + g\frac{\partial h'}{\partial y} + fu = 0, \tag{2.22b}$$

$$\frac{\partial h'}{\partial t} + \frac{\partial}{\partial x}(Hu') + \frac{\partial}{\partial y}(Hv') = 0. \tag{2.22c}$$

We now seek solutions of the form

$$u' = \hat{u}e^{i(kx+ly-\omega t)}, \quad v' = \hat{v}e^{i(kx+ly-\omega t)}, \quad h' = \hat{h}e^{i(kx+ly-\omega t)} \tag{2.23}$$

so that $\frac{\partial}{\partial t} \equiv -i\omega$, $\frac{\partial}{\partial x} \equiv ik$ and $\frac{\partial}{\partial y} \equiv il$. The resulting equations can be expressed in matrix form as

$$\begin{pmatrix} -i\omega & -f & gik \\ f & -i\omega & gil \\ ikH & ilH & -i\omega \end{pmatrix} \begin{pmatrix} \hat{u} \\ \hat{v} \\ \hat{h} \end{pmatrix} = 0. \tag{2.24}$$

A trivial solution of (2.24) is $\hat{u} = \hat{v} = \hat{h} = 0$. Non-trivial solutions are found if the determinant

$$\begin{vmatrix} -i\omega & -f & gik \\ f & -i\omega & gil \\ ikH & ilH & -i\omega \end{vmatrix} = 0. \tag{2.25}$$

A solution to this can be expressed as the cubic equation

$$i\omega(-\omega^2 + gH(k^2 + l^2) + f^2) = 0. \tag{2.26}$$

The roots of (2.26) are

$$\omega = 0, \pm\sqrt{gH(k^2 + l^2) + f^2}. \tag{2.27}$$

These roots correspond to the eigenvalues of the matrix

$$\begin{pmatrix} 0 & -f & gik \\ f & 0 & gil \\ ikH & ilH & 0 \end{pmatrix}. \tag{2.28}$$

By examining this eigenvalue problem, the nature of the roots of (2.26) can be obtained. The eigenfunction associated with the root $\omega = 0$ takes the form

$$\begin{pmatrix} \hat{u} \\ \hat{v} \\ \hat{h} \end{pmatrix} = \alpha \begin{pmatrix} -gil \\ gik \\ f \end{pmatrix}, \tag{2.29}$$

where α is a constant. This eigenfunction is geostrophic, with

$$g\frac{\partial h'}{\partial x} - fv' = 0, \tag{2.30a}$$

$$g\frac{\partial h'}{\partial y} + fu' = 0, \tag{2.30b}$$

and non-divergent, with

$$\frac{\partial}{\partial x}(Hu') + \frac{\partial}{\partial y}(Hv') = 0. \tag{2.31}$$

This solution represents the low frequency vortical motion and describes the large-scale behaviour of the flow that is observed to be in approximate geostrophic and hydrostatic balance and almost non-divergent. The eigenfunction associated with the other eigenvalues are

$$
\begin{pmatrix} \hat{u} \\ \hat{v} \\ \hat{h} \end{pmatrix} = \alpha \begin{pmatrix} gk\varpi - gilf \\ -gl\varpi - gikf \\ gH(k^2 + l^2) \end{pmatrix}, \tag{2.32}
$$

where

$$
\varpi = \sqrt{gH(k^2 + l^2) + f^2}, \tag{2.33}
$$

where α is a constant. These eigenfunctions are neither geostrophic nor non-divergent and this mode of solution represents the relatively faster IGWs. A consequence of (2.33) is that

$$
|\omega_{IGW}| = |\sqrt{gH(k^2 + l^2) + f^2}| \geq f, \tag{2.34}
$$

implying a distinct frequency separation between this root and the $\omega = 0$ root.

2.5 Transformation of the shallow water equations

Next we outline a transformation of the shallow water equations and formulate the two models that will be investigated in this study, namely $\mathrm{CA}_{\tilde{h},\delta}$ and $\mathrm{CA}_{\delta,\gamma}$.

2.5.1 $\mathbf{CA}_{\tilde{h},\delta}$

It is common for the shallow water equations (2.19) and (2.20) to be expressed in a vorticity-divergence (ζ-δ) configuration where

$$\zeta = \frac{\partial v}{\partial x} - \frac{\partial u}{\partial y}, \tag{2.35a}$$

$$\delta = \frac{\partial u}{\partial x} + \frac{\partial v}{\partial y}. \tag{2.35b}$$

Taking the curl ($\nabla\times$) and the divergence ($\nabla\cdot$) of (2.20) and reformulating equation (2.19) in terms of $\tilde{h} = h'/H$, where H is the mean depth of the fluid and h' is a deviation from the mean depth, gives

$$\frac{\partial \zeta}{\partial t} + f\delta = -\nabla \cdot (\mathbf{u}\zeta), \tag{2.36a}$$

$$\frac{\partial \delta}{\partial t} + c^2\nabla^2\tilde{h} - f\zeta = -\nabla \cdot (\mathbf{u} \cdot \nabla\mathbf{u}), \tag{2.36b}$$

$$\frac{\partial \tilde{h}}{\partial t} + \delta = -\nabla \cdot (\mathbf{u}\tilde{h}). \tag{2.36c}$$

Equations (2.36a) and (2.36c) can be manipulated to demonstrate the material conservation of PV

$$\frac{Dq}{Dt} = \frac{\partial q}{\partial t} + \mathbf{u} \cdot \nabla q = 0, \tag{2.37}$$

where

$$q = \frac{\zeta + f}{1 + \tilde{h}}, \tag{2.38}$$

is the shallow water potential vorticity. Equation (2.37) has the advantage over (2.36a) that it contains no IGW motion and determines only the vortical component of the flow.

Equations (2.36b), (2.36c) and (2.37) form a closed system of equations with prognostic variables $(q, \delta, \tilde{h})$. This model will be referred to as $\mathrm{CA}_{\tilde{h},\delta}$, Dritschel *et al.* (1999), Smith & Dritschel (2006) and Mohebalhojeh & Dritschel (2007). To recover the primitive variables $(\mathbf{u}, h)$ we solve Poisson equations, with ζ calculated from (2.38), to determine the streamfunction ψ and the velocity potential χ from

$$\nabla^2 \psi = \zeta, \tag{2.39a}$$

$$\nabla^2 \chi = \delta, \tag{2.39b}$$

with the Helmholtz decomposition

$$\mathbf{u} = \mathbf{k} \times \nabla\psi + \nabla\chi, \tag{2.40}$$

enabling the horizontal velocity components to be obtained through

$$u = \frac{\partial \chi}{\partial x} - \frac{\partial \psi}{\partial y}, \tag{2.41}$$

$$v = \frac{\partial \chi}{\partial y} + \frac{\partial \psi}{\partial x}. \tag{2.42}$$

The depth field can be recovered from (2.36c) and the definition of $\tilde{h}$.

2.5.2 $\mathbf{CA}_{\delta,\gamma}$

To construct $\mathrm{CA}_{\delta,\gamma}$ we introduce the acceleration divergence γ, where

$$\gamma = \nabla \cdot \frac{D\mathbf{u}}{Dt} = f\zeta - \beta u - c^2 \nabla^2 \tilde{h}, \tag{2.43}$$

with $\beta = df/d\phi = 2\Omega\cos\phi$. Note that for a constant background rotation, γ/f is the ageostrophic vorticity. Geostrophic flow corresponds to $\gamma = 0$, cf. (2.30).

The new choice of variables discards $\tilde{h}$ in favour of γ. The motivation for the formulation of $\mathrm{CA}_{\delta,\gamma}$ is to select prognostic variables which better distinguish between balanced and IGW motion. The main problem with $\text{CA}_{\tilde{h},\delta}$ stems from the depth field containing mainly balanced, geostrophic motion making $\tilde{h}$ not the ideal choice of imbalance variable. The idea is to choose variables that represent the departure from balance by the selection of 'wave variables', Mohebalhojeh & Dritschel (2000), (2001).

The prognostic equation for δ, (2.36b) can be re-expressed to include γ, which, along with a prognostic equation for γ are, in spherical coordinates

$$\frac{\partial \delta}{\partial t} - \gamma = -|\mathbf{u}|^2 - 2\left[\frac{\partial u}{\partial \phi}\left(\frac{\partial u}{\partial \phi} + \zeta\right) + \frac{\partial v}{\partial \phi}\left(\frac{\partial v}{\partial \phi} - \delta\right)\right] - \nabla \cdot (\delta \mathbf{u}), \tag{2.44}$$

$$\frac{\partial \gamma}{\partial t} - c^2 \nabla^2 \delta = c^2 \nabla^2 \{\nabla \cdot [\tilde{h}\mathbf{u}]\} + 2\Omega \frac{\partial B}{\partial \lambda} - \nabla \cdot (Z\mathbf{u}), \tag{2.45}$$

where $B \equiv c^2 \tilde{h} + \frac{1}{2}|\mathbf{u}|^2$ is the Bernoulli pressure and $Z \equiv f(\zeta + f)$. Equations (2.37), (2.44) and (2.45) form a closed system which we will refer to as $\text{CA}_{\delta,\gamma}$, Smith & Dritschel (2006), Mohebalhojeh & Dritschel (2007).

To recover the primitive variables a slightly different procedure than that followed in $\text{CA}_{\tilde{h},\delta}$ is used. The primitive variables $(\mathbf{u}, \tilde{h})$ can be found from (q,δ,γ) by the following inversion. The divergence potential χ is found from (2.39b). To find ψ, the non-divergent component of (2.40), ζ is needed, which depends on q and $\tilde{h}$ through the definition of q

$$\zeta = (1 + \tilde{h})q - f, \tag{2.46}$$

which can be substituted into the definition of γ from (2.43) to give

$$c^2 \nabla^2 \tilde{h} - fq\tilde{h} = f(q - f) - \beta u - \gamma, \tag{2.47}$$

which can be expressed as in terms of $\tilde{h}$ and solved iteratively in the form

$$(c^2\nabla^2 - f^2)\tilde{h}^{n+1} = f(\zeta - f\tilde{h}^n) - \beta u - \gamma. \tag{2.48}$$

Typically, only a few iterations are needed to achieve convergence, as the point-wise difference between successive iterations of $\tilde{h}$ becomes less than 10^{-8}. Once $\tilde{h}$ is known ζ can be found, which in turn allows the solution of (2.39a) which allows the horizontal velocity components to be found from (2.40).

The numerics involved in the solution of $\mathrm{CA}_{\tilde{h},\delta}$ and $\mathrm{CA}_{\delta,\gamma}$ will be outlined in section §2.7.

2.6 Non-hydrostatic model under the Boussinesq approximation

Another model that we will investigate in this thesis is the non-hydrostatic model under the Boussinesq approximation. This model exhibits a weak background stratification, allowing accelerations in the vertical direction, properties which move a step closer to physical reality from the shallow water model. An important limit of this system of equations is the quasigeostrophic limit. A derivation of the relationship between the non-hydrostatic and quasigeostrophic equations is covered in appendix A.

2.6.1 Governing equations

We consider an incompressible, inviscid, rotating and stably stratified fluid under the Boussinesq approximation where the density ρ varies weakly in the vertical direction from a mean background value ρ_0, given by

$$\rho(\mathbf{x}, t) = \rho_0 + \bar{\rho}(z) + \rho'(\mathbf{x}, t), \tag{2.49}$$

where $\bar{\rho} = \varrho_z z$ is the mean linear density ($\varrho_z < 0$ is a constant) and $\rho'(\mathbf{x}, t)$ is the density anomaly with $|\varrho_z z|$ and $|\rho'| \ll \rho_0$. Under this approximation the governing equations, in terms of the velocity $\mathbf{u} = (u, v, w)$ and the buoyancy b, can be written as

$$\frac{D\mathbf{u}}{Dt} + f\mathbf{k} \times \mathbf{u} = -\frac{\nabla p}{\rho_0} + b\mathbf{k}, \tag{2.50a}$$

$$\frac{Db}{Dt} + N^2 w = 0, \tag{2.50b}$$

$$\nabla \cdot \mathbf{u} = 0, \tag{2.50c}$$

where $D/Dt \equiv \partial/\partial t + \mathbf{u} \cdot \nabla$ is the material derivative, p is the pressure, N and f are the buoyancy and Coriolis frequencies respectively, $\mathbf{k}$ is the unit vector in the vertical direction, and the buoyancy anomaly $b = -g\rho'/\rho_0$, where g is the acceleration due to gravity. The mean buoyancy is $N^2 z$, where $N^2 \equiv -g\varrho_z/\rho_0$. For the sake of simplicity, as in many previous studies, we take both f and N to be constant.

The non-hydrostatic equations can be reformulated with prognostic variables of the PV anomaly, $\varpi \equiv \Pi - 1$ and $\mathcal{A}_h$, the horizontal components of the ageostrophic vorticity $\mathcal{A}$, where

$$\Pi = (\mathbf{k} + \boldsymbol{\omega}/f) \cdot (\mathbf{k} - \nabla \mathcal{D}), \tag{2.51a}$$

$$\mathcal{D} \equiv -b/N^2, \tag{2.51b}$$

$$\mathcal{A} \equiv \boldsymbol{\omega}/f + \boldsymbol{\nabla} b/f^2, \tag{2.51c}$$

where $\boldsymbol{\omega} = (\xi, \eta, \zeta)$ is the three-dimensional vorticity field and $\mathcal{D}$ is the isopycnal displacement field. The prognostic equations are

$$
\begin{aligned}
\frac{D\varpi}{Dt} &= 0, & (2.52)\\
\frac{D\mathcal{A}}{Dt} &= -f\mathbf{k}\times\mathcal{A} + (1+c^2)\nabla w + \frac{\boldsymbol{\omega}}{f}\cdot\nabla\mathbf{u} + c^2\nabla\mathbf{u}\cdot\nabla\mathcal{D}, & (2.53)
\end{aligned}
$$

where $c \equiv N/f$. Only the horizontal components of (2.53) are considered in this model, Dritschel & Viúdez (2003). The primitive variables $\mathbf{u}$ and b are recovered from a vector potential defined through $\mathcal{A} = \nabla^2\boldsymbol{\varphi}$, with $\boldsymbol{\varphi} = \boldsymbol{\varphi}_h + \phi\mathbf{k}$. $\boldsymbol{\varphi}_h$ is obtained by inverting a Laplacian operator on $\mathcal{A}_h$ while ϕ is obtained from ϖ through the solution of a double Monge-Ampère equation

$$
\mathcal{L}_{qg}\phi = \varpi + (1-c^{-2})\Theta_z - c^{-2}\mathcal{N}(\boldsymbol{\varphi}), \qquad (2.54)
$$

where $\mathcal{L}_{qg}$ is the QG operator defined by

$$
\begin{aligned}
\mathcal{L}_{qg}\phi &\equiv \phi_{xx} + \phi_{yy} + c^{-2}\phi_{zz}, & (2.55)\\
\Theta &\equiv \nabla_h\cdot\boldsymbol{\varphi}_h, & (2.56)\\
\mathcal{N}(\boldsymbol{\varphi}) &\equiv \nabla(\nabla\cdot\boldsymbol{\varphi})\cdot[\nabla^2\boldsymbol{\varphi} - \nabla(\nabla\cdot\boldsymbol{\varphi})]. & (2.57)
\end{aligned}
$$

The velocity and displacement fields can then be recovered from

$$
\mathbf{u} = -f\nabla\times\boldsymbol{\varphi}, \qquad (2.58)
$$

$$
\mathcal{D} = -c^{-2}\nabla\cdot\boldsymbol{\varphi}. \qquad (2.59)
$$

2.7 Numerics

We now outline how the shallow water model and non-hydrostatic model under the Boussinesq approximation are solved numerically by the CASL algorithm.

We also provide a brief outline of the formulation and numerical methods used to solve the (vorticity-based pseudospectral) VPS and (Primitive equation pseudospectral) PEPS algorithms, to compare with the non-hydrostatic CASL algorithm.

2.7.1 CASL algorithm

The contour-advective semi-Lagrangian (CASL) algorithm, Dritschel & Ambaum (1997), is a hybrid Lagrangian-Eulerian numerical method that uses contour advection in the description of PV. CASL is novel in the way that it explicitly treats PV in a fully Lagrangian way and can represent PV well below the corresponding Eulerian sub-grid scale.

As discussed previously, PV is materially invariant for inviscid, adiabatic flows. In CASL, the PV is discretised into levels separated by contours that represent a jump in the PV field. These contours are held by a set of nodes that are simply advected by the flow. Curved regions of each contour have the highest density of nodes for a more accurate representation. This means that filamentary structures can be resolved with widths much less than the grid scale. This filamentary scale can be retained down to a length scale of the modellers choice, whereupon the contours need to be regularised in a process called 'contour surgery', Dritschel (1989). The density of nodes per contour depends on the curvature of the contour. Nodes can also be removed from the contour when they are no longer required. Typically PV is resolved to a tenth of the grid scale before surgery.

We shall outline in turn how CASL solves the shallow water models $\mathrm{CA}_{\tilde{h},\delta}$ and $\mathrm{CA}_{\delta,\gamma}$, and how it solves the non-hydrostatic model under the Boussinesq approximation.

Shallow water CASL

Dritschel *et al.* (1999) introduced the CASL algorithm for the f-plane shallow water equations. This method was extended to the sphere in Dritschel (2004) and Smith & Dritschel (2006). In this study we shall be solving the shallow water equations on the sphere.

PV is represented in a fully Lagrangian way as contours with the other variables held on a grid. A semi-spectral approach is employed to solve with 4th order finite differencing in latitude and a Fourier series representation in longitude. A higher resolution is afforded in latitude to compensate for the higher errors in the finite differencing scheme as opposed to the Fourier representation, so specifically, an equal number of grid points are chosen in each direction. Below is a summary of the shallow water CASL algorithm:

(1) **Initialisation**: PV is distributed in terms of a set of contours on the horizontal layer. Each contour is defined by nodes connected by a cubic spline to define the shape of the contour.

(2) **Contour-to-grid PV conversion**: PV contours from **(1)** are converted to a relatively fine gridded field via a 'fast-fill' procedure, (see Dritschel & Ambaum (1997)). PV is represented on a grid typically four times finer than the horizontal velocity grid. PV is then averaged from the fine grid to the coarse grid.

(3) **Inversion**: In both $\mathrm{CA}_{\tilde{h},\delta}$ and $\mathrm{CA}_{\delta,\gamma}$, the Poisson equations (2.39a) and (2.39b) are inverted by a fourth-order compact difference procedure, Mohebalhojeh & Dritschel (2007). In addition $\mathrm{CA}_{\delta,\gamma}$ has to solve a modified Helmholtz equation (2.48), iteratively.

(4) **Contour Advection**: The gridded velocity field is bi-linearly interpolated to get the velocity at each node, on each PV contour. These nodes are then advected using the interpolated velocity.

(5) **Contour Surgery**: Every other time-step ‘surgery’ is performed to remove filaments from the PV field that are smaller than a certain width prescribed by the modeller, typically a tenth of the grid scale. At the end of this step the nodes are redistributed on the PV contours to provide the highest possible accuracy where contours have high curvature.

The time integration scheme employs a standard semi-implicit leapfrog scheme, Ritchie (1988), with a Robert-Asselin filter used to ensure stability by damping the computational mode introduced by the time-level decoupling, Robert (1966) and Asselin (1972). In practice, this filter replaces a field Υ at time t with a combination of the field at times $t - \Delta t$, t and $t + \Delta t$ as

$$\Upsilon(x,t) \equiv \Upsilon(x,t) + A[\Upsilon(x,t-\Delta t) - 2\Upsilon(x,t) + \Upsilon(x,t+\Delta t)], \tag{2.60}$$

where A is the Robert-Asselin filter coefficient. Artificial numerical diffusion is added for stability. For the $\tilde{h}$ and δ fields a Broutman spectral filter is used (cf. Dritschel & Viúdez (2003)) which is applied in longitude only, of the form $F(m)$ =exp$[-\alpha(\eta/r)^{10}]$ for $m \geq 2$, where $\eta = (m+2)/(M-2)$, $M = n_\lambda/2$, where n_λ is the number of grid points in the longitudinal direction and α is chosen so that $F(M) = 10^{-14}$. This filter essentially removes all azimuthal variations shorter than two grid lengths at the equator. In latitude the non-linear tendencies are damped using a discrete Laplacian operator at a very small rate $D = 0.01$ per day. Smith & Dritschel (2006) demonstrate that the flow is insensitive to this coefficient.

Non-hydrostatic CASL

The development of CASL for use in modelling non-hydrostatic rotating, stably stratified flows is covered in detail in Dritschel & Viúdez (2003) and McKiver & Dritschel (2008). CASL has been used in previous studies of flows with Ro, $Fr \leq \mathcal{O}(1)$ to examine atmospheric jet-streaks, Dritschel & Viúdez (2003), (2007) and Viúdez (2006), which are observed around the tropopause and have a major impact on the upper level circulation of the atmosphere. In the oceans, the motion of cyclonic and anti-cyclonic vortices and their associated weak vertical velocities have been investigated by Viúdez & Dritschel, (2003). Such vortices are important in the deep ocean for transporting vital nutrients to the photic zone. Here we only review the key points of the method. Below is a summary of the non-hydrostatic CASL algorithm.

(1) Initialisation PV is distributed in terms of a set of contours in each horizontal layer. Each contour is defined by nodes connected by a cubic spline to define the shape of the contour.

(2) Contour-to-grid PV conversion PV contours from **(1)** are converted to a relatively fine gridded field via a 'fast-fill' procedure, (see Dritschel & Ambaum (1997)). PV is represented on a grid typically four times finer than the horizontal velocity grid and a vertical grid typically four times the number of grid points than isopycnal layers. PV is then averaged from the fine grid to the coarse grid.

(3) Inversion The horizontal components of the vector potential $\boldsymbol{\varphi}_h$ are recovered by inverting the Laplacian operator in spectral space using (Fast Fourier transform) FFTs. The vertical component of $\boldsymbol{\varphi}$ can be found through the solution of a double Monge-Ampère equation which is solved iteratively. Once $\boldsymbol{\varphi}$ is known the primitive variables can be recovered.

(4) **Contour Advection** The gridded velocity field is bi-linearly interpolated to get the velocity at each node, on each PV contour. These nodes are then advected using the interpolated velocity. The PV advection is carried out by a third-order three time-level Adams-Bashforth integration procedure. The wave variables are evolved using a standard explicit leap-frog scheme.

(5) **Contour Surgery** Every other time-step 'surgery' is performed to remove filaments from the PV field that are smaller than a certain width prescribed by the modeller, typically a tenth of the grid scale. At the end of this step the nodes are redistributed on the PV contours to provide the highest possible accuracy where contours have high curvature.

2.7.2 Pseudospectral algorithms

We now present details on the formulation of the pseudospectral algorithms and how they are solved numerically. The prognostic equations are solved by computing all derivatives in Fourier space while computing non-linear products in physical space. FFTs are used to transfer information between these representations.

Vorticity-based pseudospectral (VPS) algorithm

The VPS algorithm is described in the appendix of Dritschel & Viúdez (2003). It is a purely pseudospectral method developed to allow direct comparison with CASL. The prognostic variables of VPS are the three components of the vector $\mathcal{A}$ in (2.53) with VPS taking no explicit account of PV. The primitive variables of this system are recovered in a similar fashion as in CASL, though now all three components of $\boldsymbol{\varphi}$ are found by inverting Laplace's operator on $\mathcal{A}$.

Primitive-equation pseudospectral (PEPS) algorithm

The PEPS algorithm is a pseudospectral algorithm developed to allow a comparison with VPS. In practice, PEPS solves prognostic equations in terms of $\mathbf{u}$ and ρ':

$$\frac{\partial b}{\partial t} = -N^2 w - \nabla \cdot (b\mathbf{u}), \tag{2.61}$$
$$\frac{\partial \mathbf{u}}{\partial t} = -\nabla \cdot (\mathbf{u}\mathbf{u}^T) - f\mathbf{k} \times \mathbf{u} - \frac{\nabla p}{\rho_0} + b\mathbf{k}, \tag{2.62}$$

where $\mathbf{u}^T$ is the transpose of the velocity $\mathbf{u}$ and $p \equiv (p_h + p_{nh})$ is the specific pressure, where the subscripts h and nh refer to the hydrostatic and non-hydrostatic components. The terms $\nabla \cdot (b\mathbf{u})$ and $\nabla \cdot (\mathbf{u}\mathbf{u}^T)$ can be expressed in this form due to the isochoric condition, (2.50c). The solution of (2.62) requires p, the pressure field. The hydrostatic component is diagnosed from the hydrostatic balance equation

$$\frac{\partial p_h}{\partial z} = b. \tag{2.63}$$

Taking the divergence of (2.62) and cancelling terms involving the hydrostatic balance relation yields an expression for the non-hydrostatic component of the pressure

$$p_{nh} = \nabla^{-2}(-\nabla_h^2 p_h - \nabla \cdot (\nabla \cdot (\mathbf{u}\mathbf{u}^T)) + f\zeta). \tag{2.64}$$

Hence, the full pressure field can be found, allowing the solution of (2.62). Note, $\nabla \cdot \mathbf{u}$ remains zero here.

Following the introduction of the mathematical models and how they will be solved in this thesis, we present the results of the investigation beginning with a joint observational and numerical study in chapter §3.

Chapter 3

Balance and the Unified Model

3.1 Introduction

In this chapter we investigate the balance properties of the Unified Model (UM), the operational weather and climate prediction model of the United Kingdom Meteorological Office (UKMO). The main question that we try to answer is at what horizontal grid resolution the atmosphere exhibits features of imbalance. The UM is not a balanced model but developers and users would prefer the UM to render a balanced flow at the synoptic scale (a horizontal length on the order of $1000km$ or more). An assessment is made as to whether or not the UM does indeed produce a balanced flow at those scales. This is done by diagnosing symmetric instabilities (SIs), and the mechanisms causing them, within the UM. SIs correspond to areas in the atmosphere that are unbalanced, in the sense that a balanced model of the atmosphere would not be able to capture these features. More specifically, an area of negative Ertel PV on a surface of constant potential temperature or θ-surface, in the northern hemisphere (and positive PV on a θ-surface in the southern hemisphere) is a criterion under which a SI may theoretically occur, Hoskins (1974). Previous studies, Bennetts & Hoskins (1979), Emanuel (1988), have demonstrated the meteorological significance of the SI and its role in the formulation of frontal rain-bands and slantwise convection.

Different forms of assessment are used to ascertain whether or not these SIs predicted by the UM exist in physical reality.

The most valuable comparison method available is the sole use of observational data from aircraft and satellites to compare with UM model output. This is the highest form of truth available to the model developer.

Another form of assessment available is to assess the impact of data assimilation on the SIs. This combines model predictions and observational data to generate the initial conditions of the model run.

Lastly, an assessment is made between different versions of the UM to see if each has any impact on the properties of the SIs generated. For additional verification an inter-model comparison of the UM is made. This assesses global and NAE components of the UM and how they model SIs.

Additionally, observational data is employed in an attempt to quantify at which horizontal grid scale vortical motions in the atmosphere become coherent. High resolution aircraft data is used to investigate the properties of balanced vortical motion at a relatively fine scale. This is an important question in the context of at which horizontal scale in the atmosphere vorticity-based balanced models such as CASL may be employed in an operational context as this can only sensibly occur when there is little small-scale variation in the velocity field, avoiding sharp gradients when calculating the vorticity.

3.1.1 Symmetric instabilities

Two basic types of parcel instability that manifest in the atmosphere (and ocean) are static and inertial. A complete discussion of parcel instabilities and the derivation of their stability criteria can be found in Holton (2004). Static instability criterion assesses whether or not a flow can become turbulent due to the effects of buoyancy through the variation of potential temperature θ with height within a flow. The criterion for static instability is

$$\frac{d\theta}{dz} < 0. \tag{3.1}$$

Therefore, if there is a region where the value of θ decreases with increasing height, then the flow is statically unstable to perturbations in the vertical direction. On the synoptic scale, the atmosphere is always stably stratified because any unstable regions that develop are quickly stabilised by convective overturning.

Inertial instability criterion assesses whether or not a flow can become turbulent due to inertial effects. A measure of inertial instability is the sign of the absolute vorticity of the basic flow. It is convenient to express this criterion in terms of M ($\equiv fy - u_g$), a surface of absolute momentum, where f is the Coriolis frequency, y is the northward direction and u_g is a zonal geostrophic wind. The criterion for an inertial instability is

$$f\frac{\partial M}{\partial y} = f\left(f - \frac{\partial u_g}{\partial y}\right) = f\left(f + \zeta\right) < 0, \tag{3.2}$$

where ζ is the vertical component of the relative vorticity. Therefore, in the northern hemisphere, where $f > 0$, if there is an area where the absolute vertical vorticity ($\equiv f + \zeta$) of the basic flow is negative, then the flow is inertially unstable to perturbations in the horizontal direction. An inertial instability on the synoptic scale would trigger unstable motions which would mix the fluid laterally until the vertical component of absolute vorticity was positive again.

A more general form of parcel instability within a flow is the conditional symmetric instability or just the symmetric instability (SI), about which more detailed information can be found in Schultz & Schumacher (1999). This corresponds to a parcel of fluid that has been displaced in a slantwise direction, rather than strictly in the horizontal or vertical direction. This displacement is generally aligned with θ-surfaces. Holton (2004) derives the SI stability criterion by analysing the dynamics of a front. This criterion depends upon the relative orientation of surfaces of absolute momentum M- and θ-surfaces and can be interpreted as an isentropic inertial instability. Based on the inertial instability criterion from (3.2), the criterion for a SI within a general flow is

$$f\left(\frac{\partial M}{\partial y}\right)_{\theta} < 0. \tag{3.3}$$

This states that the flow is unstable with respect to displacements along constant θ-surfaces. This may occur in regions with a very strong horizontal temperature gradient and weak vertical stability. Stability criterion for a SI can be satisfied without static and inertial criteria being satisfied. The only difference from the inertial stability criterion is that the derivative of M with respect to y is taken along a θ-surface. Multiplying (3.3) by $-g(\partial\theta/\partial p)$ gives the criterion in the simple form

$$f\Pi_{\theta} < 0, \tag{3.4}$$

where

$$\Pi_{\theta} \equiv (\zeta_{\theta} + f)\left(-g\frac{\partial\theta}{\partial p}\right), \tag{3.5}$$

where Π_{θ} is the isentropic coordinate form of Ertel PV, hereafter referred to as Π, with ζ_{θ} is the vertical component of the relative vorticity evaluated on an isentropic surface. Thus if Ertel PV is positive at all locations in the atmosphere initially, then the atmosphere of the northern hemisphere is symmetrically stable. More importantly this implies that a SI cannot arise due to adiabatic motions as

Ertel PV is materially conserved in the atmosphere, so would remain positive for all time. This is a key requirement for a global balanced model and illustrates why an accurate representation of Ertel PV in any numerical model is so crucial.

3.1.2 Unified Model calculation of potential vorticity

The diagnostic field required to assess areas of imbalance within the UM is the Ertel PV field

$$\Pi = \alpha(2\mathbf{\Omega} + \nabla \times \mathbf{u}) \cdot \nabla\theta, \tag{3.6}$$

where α is the specific volume, Ω is the Earth's angular velocity, $\mathbf{u}$ is the three dimensional velocity vector relative to the rotating Earth and θ is the potential temperature. Equation (3.6) is evaluated on a θ-surface and is approximated by

$$\Pi = \alpha\Bigg[\frac{1}{a\cos\phi}\frac{\partial v}{\partial z}\frac{\partial\theta}{\partial\lambda} + \frac{1}{a}\frac{\partial u}{\partial z}\frac{\partial\theta}{\partial\phi}$$

$$+\left(2\Omega\sin\phi + \frac{1}{a\cos\phi}\left(\frac{\partial v}{\partial\lambda} - \frac{\partial(u\cos\phi)}{\partial\phi}\right)\right)\frac{\partial\theta}{\partial z}\Bigg], \tag{3.7}$$

from Anderson & Roulstone (1993). In this approximation, $2\Omega\cos\phi$, some metric terms and vertical acceleration have been neglected. Units of Ertel PV are $m^2s^{-1}Kkg^{-1}$. Typically $1 \times 10^{-6}m^2s^{-1}Kkg^{-1}$=$1PVU$.

The Ertel PV is calculated using a centred finite difference method on model ρ-levels. Linear interpolation is used to assign θ at Ertel PV locations, then values of Ertel PV are interpolated onto θ-surfaces. An example of the Ertel PV from the global model at θ=$310K$ is shown in figure 3.1. The green structure between the UK and Ireland is an area of negative Ertel PV indicating an area of imbalance, characterised by the presence of a SI. This is the procedure that is

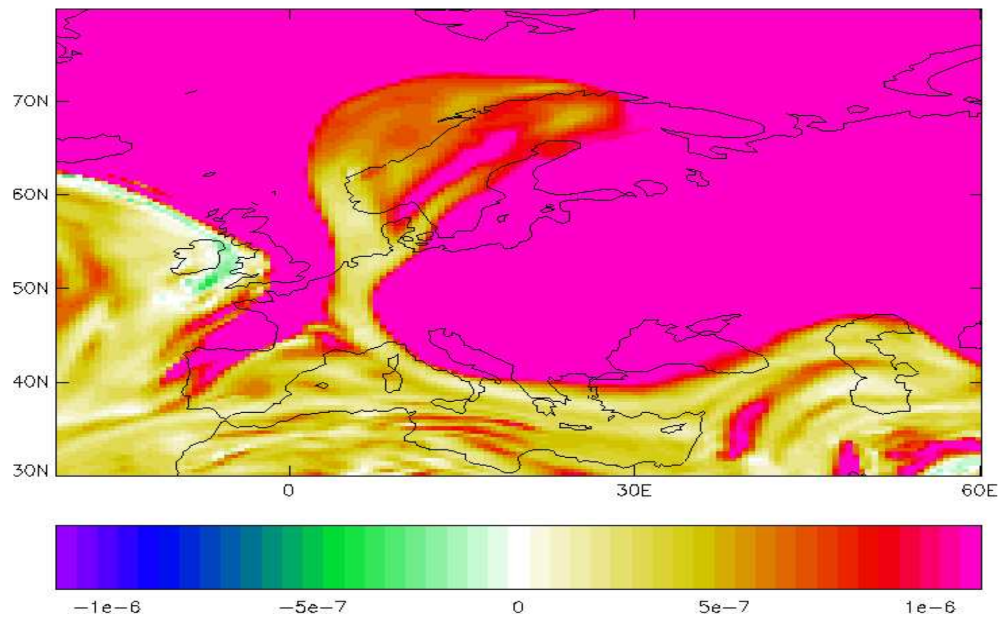

Figure 3.1: Ertel PV at θ=310K from the global model at 2100UTC on 11 Feb 2006 from initial data at 0000UTC on 11 Feb 2006.

used to discover the nature and quantity of SIs predicted by the UM.

3.1.3 Symmetric instabilities and evidence of imbalance

Initially, a case on 01 August 2006 was investigated to ascertain which effect, static or inertial, played the dominant role in the occurrence of the SI. Consider the Ertel PV from the previous chapter, (3.7). Scaling arguments suggest that the vertical component of the absolute vorticity is the dominant term due to the Coriolis frequency f=$2\Omega\sin\phi$. This component of Ertel PV within the UM, from (3.7) can be decomposed as

$$2\Omega\sin\phi + \frac{1}{a\cos\phi}\left(\frac{\partial v}{\partial\lambda} - \frac{\partial(u\cos\phi)}{\partial\phi}\right), \tag{3.8}$$

and

$$\frac{\partial \theta}{\partial z}. \tag{3.9}$$

They are the vertical component of the absolute vorticity and the vertical derivative of potential temperature. By calculating these quantities an assessment of the contribution of each to the vertical component and thus full Ertel PV can be made.

Simulations were undertaken within the NAE to obtain the Ertel PV field on θ=320K at 0000UTC on 01 August 2006. Figure 3.2 shows the full Ertel PV field and (3.8), the vertical component of the absolute vorticity. There are six areas common to each field that have been highlighted in a thick black outline. The contribution to the areas of negative Ertel PV field are from areas of negative absolute vertical vorticity suggesting that the atmosphere is also inertially unstable in this area or that the instability is closely related to inertial effects. The source of the noise in the lower part of the NAE plot is most likely due to a combination of orographic effects from the Atlas mountains and proximity to the domain boundary.

Also highlighted in figure 3.2 in thick white outline are areas where the atmosphere is predicted to be inertially unstable, but no evidence of instability is found in the corresponding area of the Ertel PV field to indicate the presence of a SI.

Figure 3.3 shows the calculation of (3.9) and demonstrates that the UM predicts that the atmosphere is statically stable on the synoptic scale as expected. Therefore, in this instance the mechanism behind the evidence of the SI is inertially rather than statically dominated. This behaviour was found in general. This may be expected as the stability criterion of a SI is similar to that of an inertial instability from (3.2).

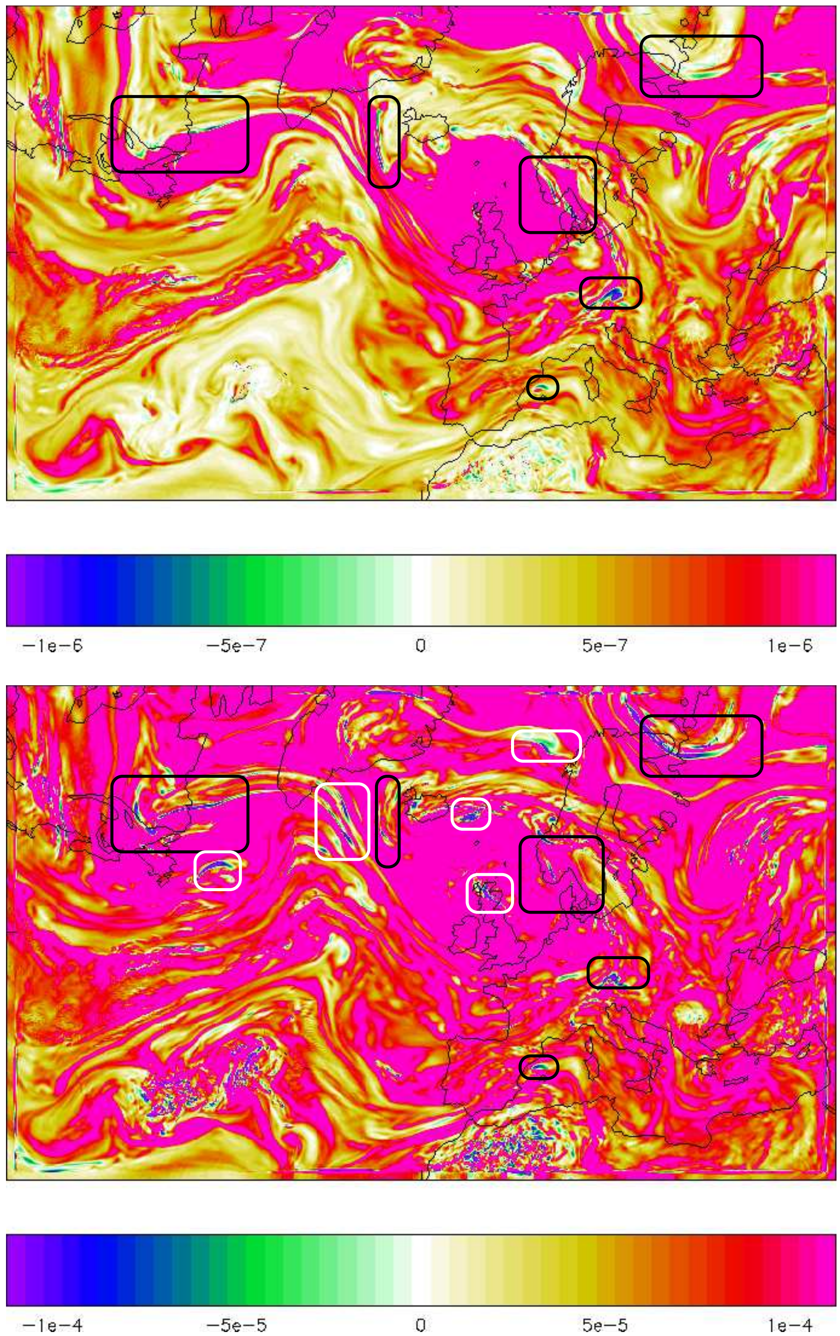

Figure 3.2: *Top*: Ertel PV and *bottom*: Absolute vertical vorticity, at θ=320K from the NAE, at 0000UTC on 01 Aug 2006 from initial data at 0000UTC on 31 Jul 2006. Note the different values of scales.

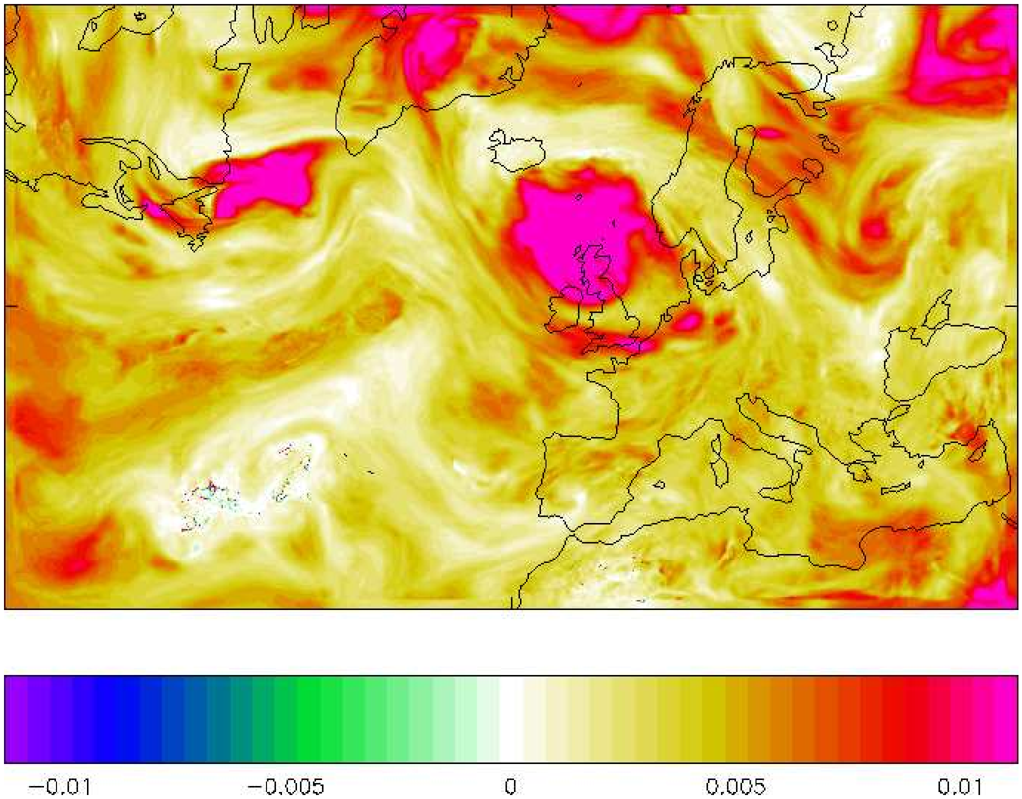

Figure 3.3: $\partial\theta/\partial z$ at θ=320K from the NAE at 0000UTC on 01 Aug 2006 from initial data at 0000UTC on 31 Jul 2006.

3.2 Results

3.2.1 Observational and model comparison

Diagnostic output from a numerical weather prediction production model can only be truly validated by comparison with observational data as fully realistic, exact solutions to the equations solved by the dynamical core of the model are not available. In this spirit an attempt is made to discover whether or not evidence of negative Ertel PV in the atmosphere can be calculated directly from observational data to compare with the UM.

The initial aim is to undertake a calculation of Ertel PV from (3.7) at differing horizontal grid scales approximately $40km$ and $12km$ so that a direct comparison could be drawn with the corresponding global and NAE diagnostic output. A direct calculation from observational data requires horizontal velocity components u, v, pressure p and temperature T. θ can be obtained from the relation

$$\theta = T\left(\frac{p_o}{p}\right)^{\kappa}, \tag{3.10}$$

where p_o is the standard atmospheric pressure taken to be $1013.25hPa$ in this case and $\kappa{=}R/c_p \approx 0.286$.

One source of atmospheric observations was the Meteorological Office observational database (MetDB). The primary purpose of the MetDB is to provide observational data that will be used in the data assimilation procedures discussed in section §3.2.5. Observational data sources available were from commercial and non-commercial aircraft and the Meteosat Second Generation (MSG) satellite, Schmetz *et al.* (2002). A region of interest chosen was the southern part of the UK, the domain covered approximately in figure 3.5. This area was chosen due to the relative abundance of aircraft traffic and the availability of different LAMs within the UM for this region. Lack of satellite coverage over this region meant that the use of satellite data was not feasible for this project leaving aircraft data as the only option. A major drawback to using aircraft data is that aircraft tend to fly along levels of constant height so a vertical profile of data was difficult to achieve.

After a detailed investigation it became evident that finding a three-dimensional region that had enough observational data so that the interpolation problem was overdetermined was practically impossible. Two-dimensional quantities proved easier to calculate than three-dimensional quantities. That said, horizontally, the finest two-dimensional gridded observational data available was at a resolution of approximately $54km$ squared. A quantity that was able to be calculated with relative ease was the vertical component of the absolute vorticity. As discussed in section §3.1.3, this quantity is significant as regions where the atmosphere was found to be inertially unstable corresponded in the main to areas where the atmosphere was symmetrically unstable.

To obtain observational data at a finer scale a single flight on a BAe 146-301 atmospheric research aircraft was undertaken from the Facility for Airborne Aircraft Measurements (FAAM) at RAF Cranfield. On this flight a very fine horizontal resolution of observational data was available along with dropsonde data to give a vertical profile of the atmosphere.

It should be remarked that targeted studies that included a significant observational component such as the Mesoscale Alpine Project (MAP), Bougealt *et al.* (2001), Fronts and Atlantic Storm Track Experiment (FASTEX), Joly *et al.* (1997) and the Convective Storm Initiation project (C-SIP), Browning *et al.* (2007) required a very large number and variety of observational apparatus that was unfortunately not available within the confines of this study.

Next, two case studies are presented, each with observational data from differing sources where a calculation of absolute vertical vorticity is undertaken in an attempt to gain dynamical knowledge of a SI and thus evidence of imbalanced motion.

3.2.2 Case study: 15 July 2007

To locate potential areas where negative Ertel PV may occur a survey of atmospheric pressure charts was undertaken to decide which dates would be suitable for further investigation. Criteria required that a front or atmospheric feature of interest be present over southern England. This area corresponded to where the greatest density of aircraft observations were available. A survey of atmospheric pressure charts indicated the following dates were suitable for further

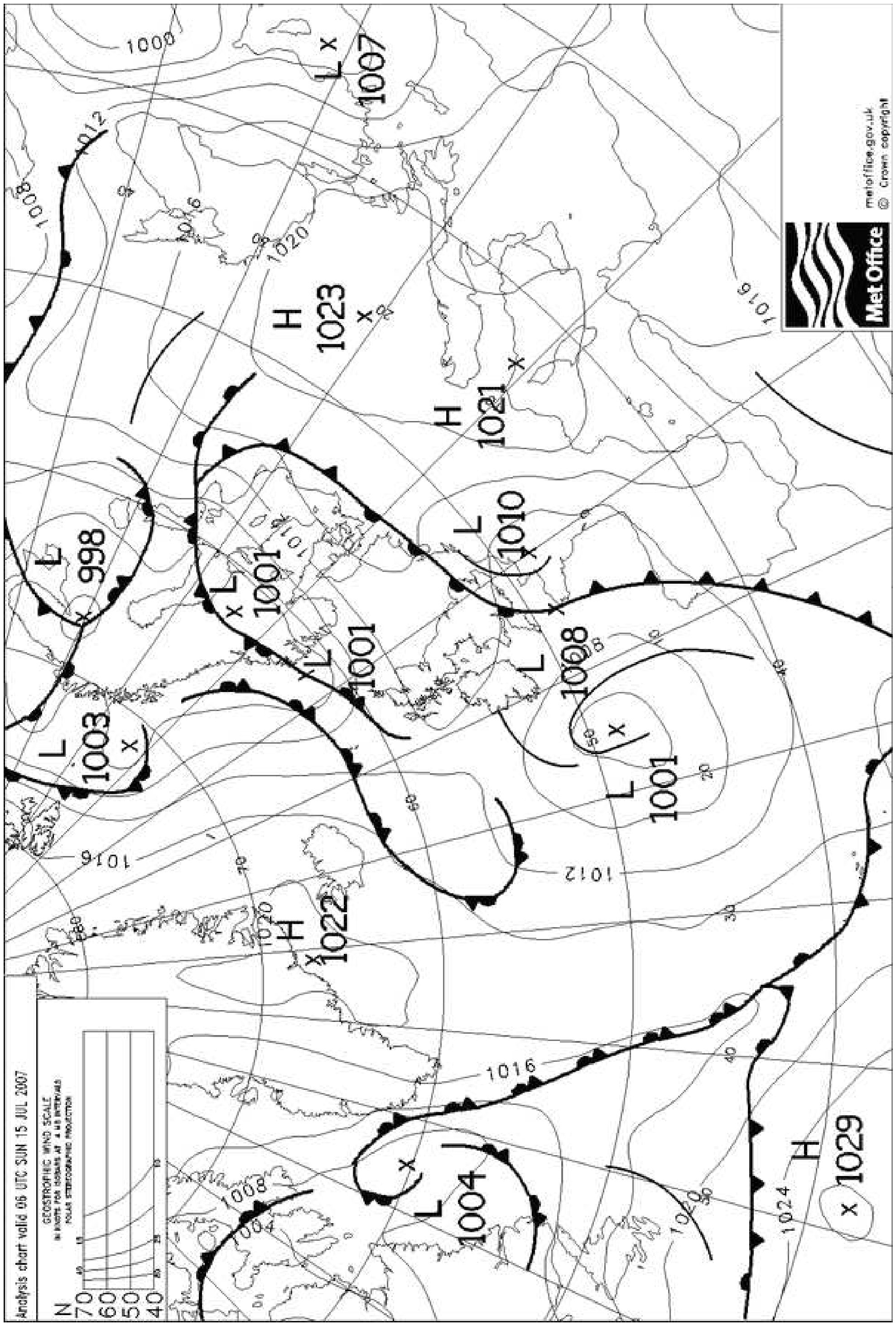

Figure 3.4: Analysis chart displaying the pressure field corrected for sea-level on 15 Jul 2007 at 0600UTC.

investigation

2006:	Feb 11, 14	Jul 30-31	Aug 01
	Sep 14	Oct 19-20	Nov 17, 19-20, 30
	Dec 03, 09, 12		
2007:	Jan 24	Feb 09, 11-12, 25	Mar 03, 06
	May 15, 27	Jun 20-22, 25	Jul 13, 15, 18, 27, 30
	Aug 14-15		

In total 35 days spanning 19 months.

The NAE was used as a diagnostic tool to locate areas of negative Ertel PV. The $40km$ horizontal resolution of the global model was deemed too coarse and therefore not *as* reliable in modelling the parcel instability, which is by nature a high resolution feature. Simulations of the NAE were undertaken on the following dates

2006:	Feb 14	Jul 30-31	Dec 03
2007:	Mar 06	Jun 21-22, 25	Jul 13, 15, 18, 27, 30
	Aug 14-15		

15 days in total. In each case evidence of Ertel PV was located.

There were two main obstacles to obtaining a meaningful comparison of UM output and observational data. Firstly, negative Ertel PV was found in the diagnostic output of the NAE on all the dates listed, but the location, size and persistence of each structure found varied markedly, and secondly, regular observational data was generally not available to coincide with areas of negative Ertel PV predicted by the NAE.

The 15th July 2007 case provided the best opportunity where a comparison between the NAE and observational data could be made. This set of circumstances proved to be the exception. Figure 3.4 displays an atmospheric pressure chart produced at 0600UTC on 15 July 2007 containing the pressure field corrected for sea-level. Of note across the southern part of the UK is a warm front advancing from mainland Europe, a thicker line with semi-circular markings. This meteorological phenomenon may indicate the presence of an area of negative Ertel PV.

Figure 3.5 contains the Ertel PV field at θ=330K which is an altitude of approximately 10km, from an NAE simulation on 15 July 2007 at 0700. Evidence of negative Ertel PV can be found over East Anglia. Also, a ribbon-like arc of negative Ertel PV is located in the Irish sea. Both areas indicate the possible presence of a SI, which is evidence of imbalance.

As mentioned previously calculations of the Ertel PV field proved challenging. To gain dynamical knowledge from observational data a calculation of the inertial stability criterion was made. To do this, horizontal velocity vectors are required on a single height level, allowing a more simple calculation than of the three-dimensional Ertel PV. The inertial stability criterion was not the original target, but should still provide important information from observational data alone, regarding the dynamics of the areas of negative Ertel PV found in the diagnostic output of the UM.

The observations retrieved were irregularly spaced and were interpolated linearly to a regular grid with resolution $\Delta\phi$, $\Delta\lambda$ of approximately 55km, comparable to the scale of the global model for a synoptic scale calculation.

A second-order centred finite difference calculation was made of (3.8) using IDL software. In total there were 200 observations in a domain bounded in longitude by (3.87W, 5.95E) and in latitude by (49.02N, 54.97N) centred on coordinates (λ=1.04E, ϕ=51.99N). This area of the domain is approximately a

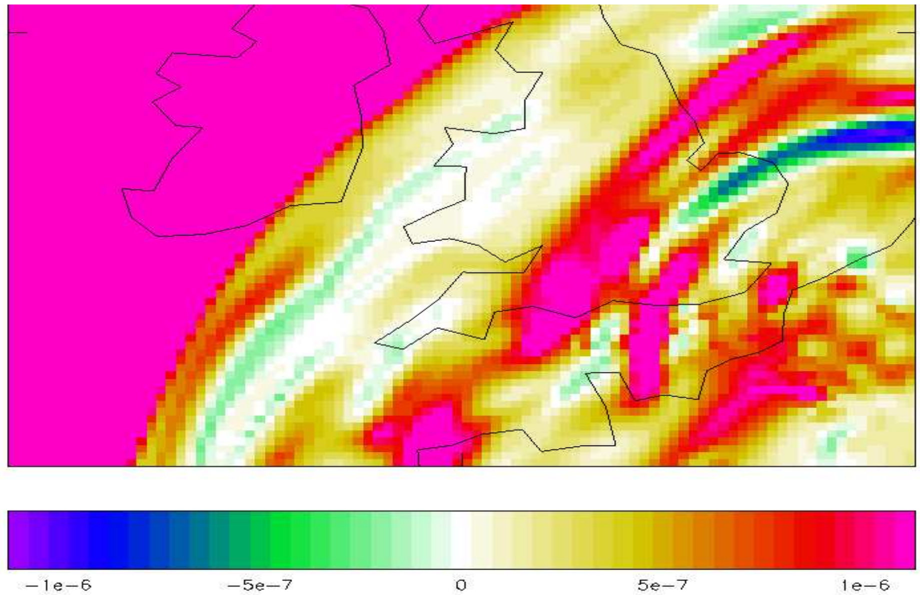

Figure 3.5: Ertel PV at θ=330K from the NAE at 0700UTC on 15 Jul 2007 from initial data at 0000UTC on 15 Jul 2007.

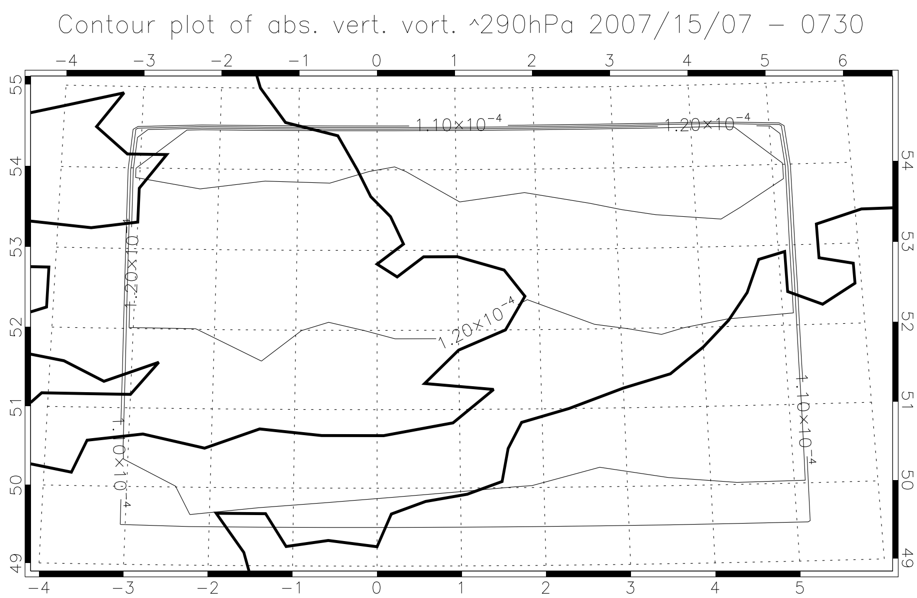

Figure 3.6: Vertical component of absolute vorticity from observational data at 0730UTC on 15 Jul 2007.

square with edge length $700km$. The absolute vertical vorticity field calculated from observations is shown in figure 3.6.

The absolute vertical vorticity is dominated by the Coriolis frequency, f, as the field displays a banded structure in latitude. Two conclusions are possible, one being that the SI predicted by the UM is spurious but a more likely explanation is that there was not enough observational data available to make a meaningful calculation. This case study really illustrated just how challenging it is to reconstruct vorticity fields over a relatively vast area, near the height of the tropopause.

3.2.3 Case study: 14 August 2008

As the use of data from the MetDB had not proved successful a single flight on a research aircraft was planned to harvest high resolution data.

Figure 3.7 displays an atmospheric pressure chart produced at 1200UTC on 14 August 2008 containing the pressure field corrected for sea-level. There is an area of low pressure centred on the west coast of Scotland with an occluded front just to the south of this low pressure centre. This meteorological phenomenon may indicate the presence of an area of negative Ertel PV giving confidence that this would be an appropriate area to conduct the research flight.

Figures 3.12, 3.14 and 3.16 display the Ertel PV field on θ-surfaces at 1200UTC, 1300UTC and 1400UTC respectively on 14 August 2008, from the NAE. There is clear evidence of low or negative areas of Ertel PV which would suggest that the absolute vorticity is also low in this area confirming the analysis of the surface pressure chart.

On flight B395 on 14 August 2008 the FAAM observational aircraft obtained high resolution observations horizontally along flight tracks over an area of approximately $100km$ squared, centred on $(56N,\ 8W)$ at 3 different height levels,

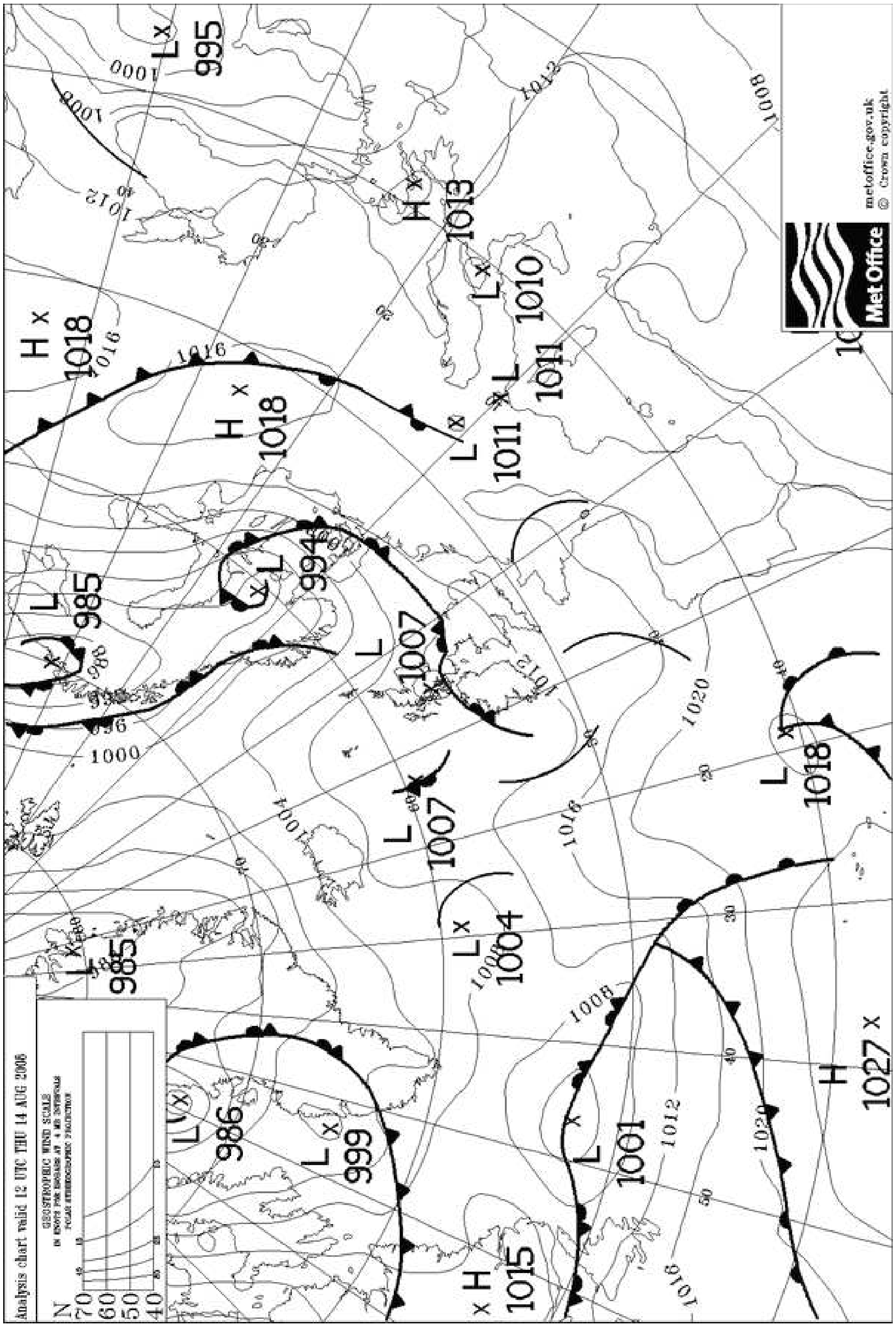

Figure 3.7: Analysis chart displaying the pressure field corrected for sea-level on 14 Aug 2008 at 1200UTC.

and vertically from a dropsonde device. Runs 1, 2 and 3 corresponded to height levels of approximately $7.9km$, $9.2km$ and $10.4km$ respectively. Sonde 1 dropped at the end of run 2 at location ($56.2N$, $8.3W$). Sonde 2 dropped at the end of run 3 at location ($56.1N$, $6.3W$). The spiral pattern for each of the three levels is shown in figure 3.8. The forecast model with interpretation from the Meteorological Office Chief Forecaster Anthony Astbury, predicted in situ that the structure of interest was moving eastwards so an allowance was made to allow the aircraft to drift with the structure.

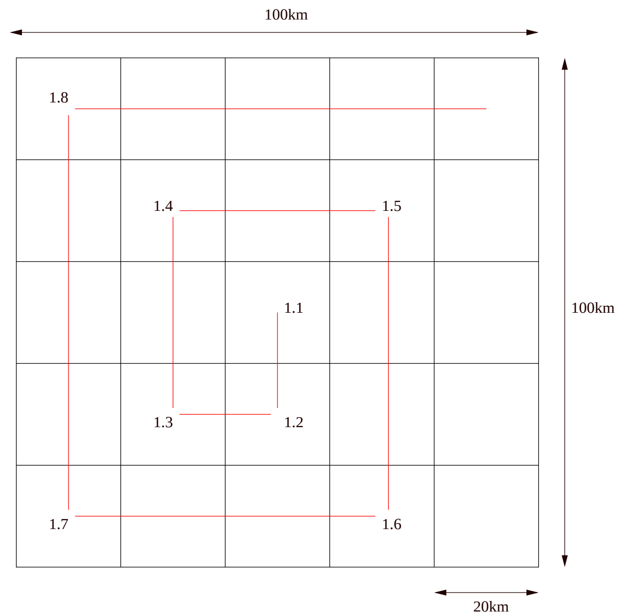

Figure 3.8: Flight Plan for flight B395. This formation was followed at each height level. Height level 1 is given here.

This resulted in the domains of each run (height level) of; run 1 - ($8.79W$, $7.39W$, $55.6N$, $56.3N$), run 2 - ($8.38W$, $6.88W$, $55.44N$, $56.35N$) and run 3 - ($7.85W$, $6.33W$, $55.52N$, $56.44N$).

Figures 3.9 and 3.10 show the horizontal velocity fields for runs 1 and 3 respectively, interpolated to $5km$ horizontal grid resolution, demonstrating a clear signature of anti-cyclonic flow, giving confidence that we would discover low or negative values of the vertical component of the absolute vorticity, satisfying the criterion for an inertial instability.

As outlined previously in section §3.2.1 it is challenging to obtain a full three-dimensional calculation of the Ertel PV field as the vertical derivative of potential temperature is almost impossible to calculate from the observational data available. So, the vertical component of the absolute vorticity was calculated as we had found that when the atmosphere was symmetrically unstable it was usually inertially unstable. Again, this quantity was not the original target, but nonetheless provided important dynamical information.

The observational data was interpolated linearly to a grid spacing $\Delta\phi$, $\Delta\lambda$ of approximately $12km$, to compare with an NAE simulation, on each height level. The absolute vertical vorticity fields, at each level are shown in figures 3.13, 3.15 and 3.17.

At each height level the vertical component of the absolute vorticity field shows evidence of an inertial instability, at the equivalent resolution as predicted by the NAE which is encouraging as it demonstrates that the UM is not spuriously producing evidence of an SI at this resolution. The key fact here is that evidence of the inertial instability has been found, rather than trying to match the UM output with observations exactly.

Also, data was available from two dropsondes, so that an estimate of $\partial\theta/\partial z$ could be made to ascertain if there was a contribution to the value of negative or low Ertel PV from this term. As expected, in the main the atmosphere was statically stable where dropsonde measurements were undertaken. Figure 3.11 shows potential temperature plotted against height for both dropsonde 1 and dropsonde 2.

The next question to ask was at which horizontal scale did evidence of the inertial instability cease to exist. This was done by decreasing the resolution of

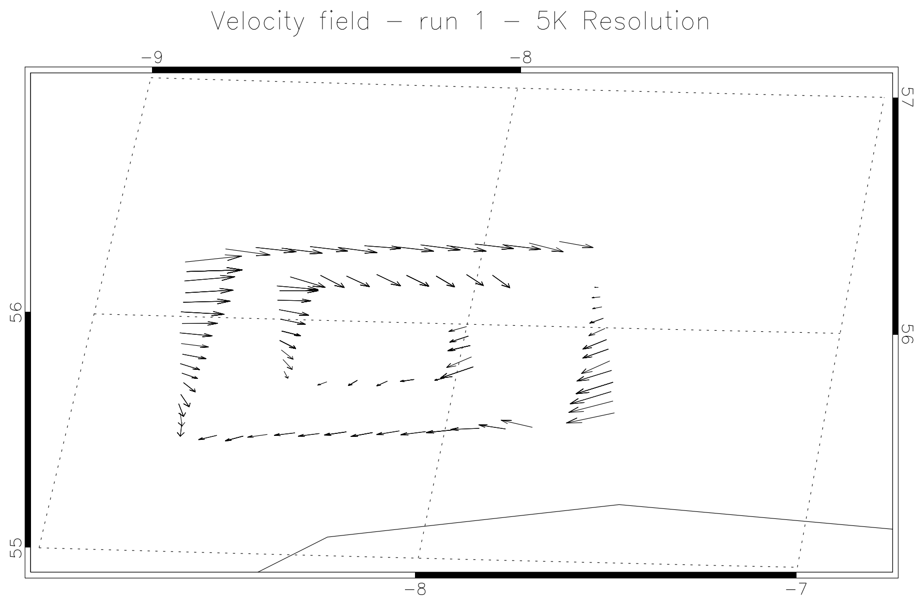

Figure 3.9: Horizontal velocity field at height $9.2km$, at $5km$ horizontal resolution.

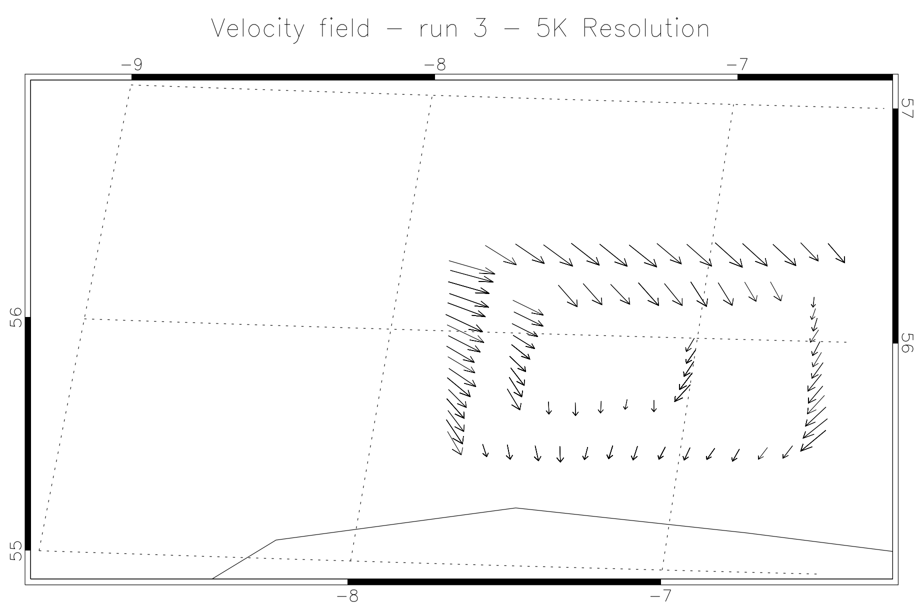

Figure 3.10: Horizontal velocity field at height $10.4km$, at $5km$ horizontal resolution.

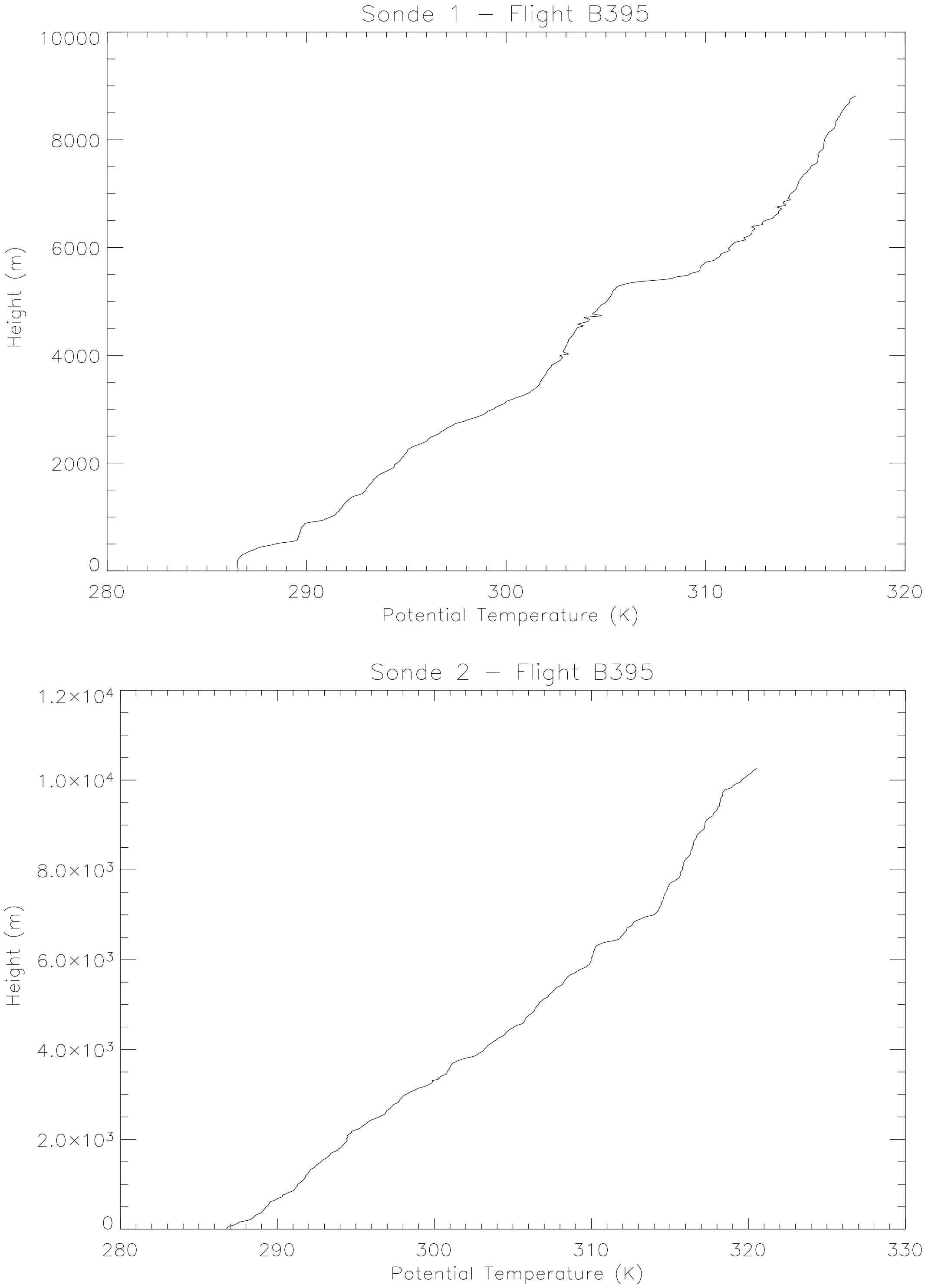

Figure 3.11: Vertical profile of θ from dropsondes 1 and 2 from flight B395. These were dropped from the coordinates ($56.2N$, $8.3W$) and ($56.1N$, $6.3W$).

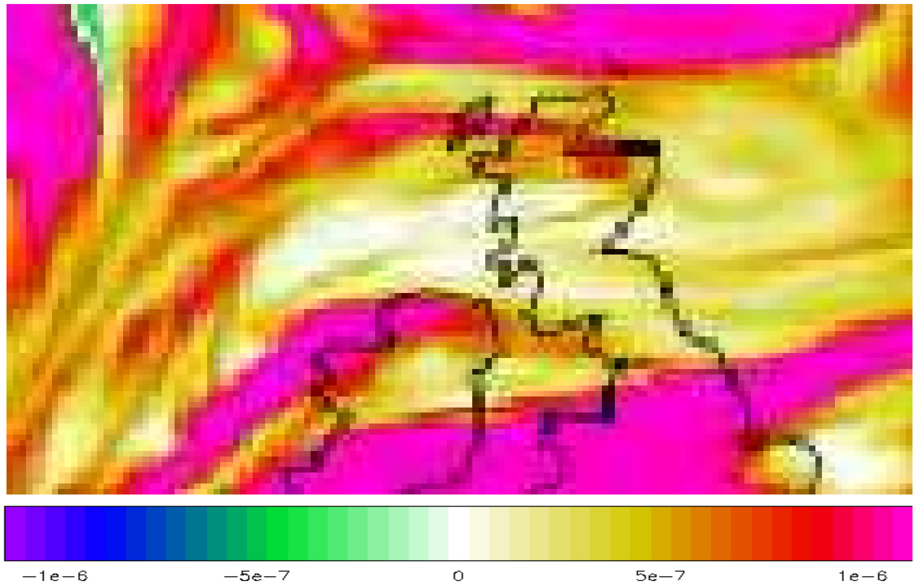

Figure 3.12: Ertel PV at θ=315K from the NAE at 1200UTC on 14 Aug 2008 from initial data at 0000UTC on 14 Aug 2008.

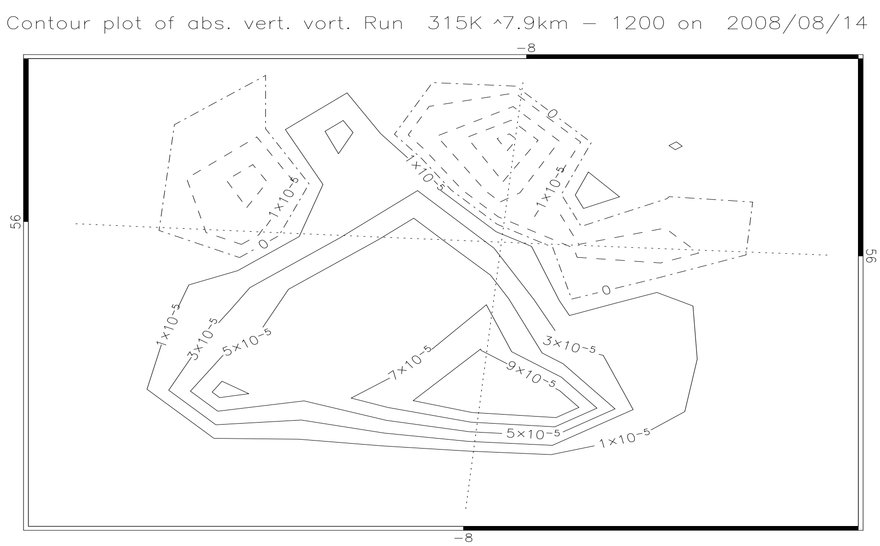

Figure 3.13: Vertical component of absolute vorticity from observational data at 1200UTC on 14 Aug 2008, at resolution (11.2km, 10.3km). Positive contours are solid lines. Zero contour is dot-dash line, negative contours are dashed lines.

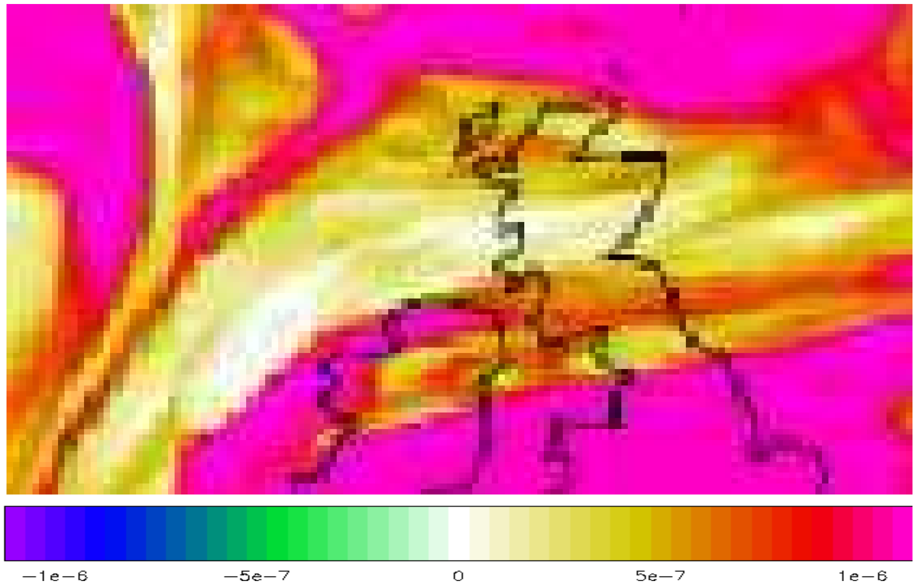

Figure 3.14: Ertel PV at θ=317K from the NAE at 1300UTC on 14 Aug 2008 from initial data at 0000UTC on 14 Aug 2008.

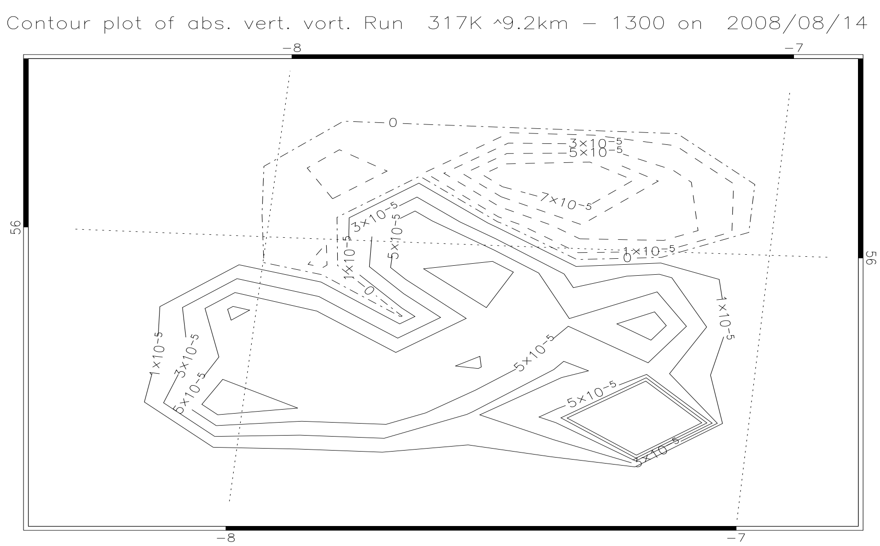

Figure 3.15: Vertical component of absolute vorticity from observational data at 1300UTC on 14 Aug 2008, at resolution (11.3km, 10.5km). Positive contours are solid lines. Zero contour is dot-dash line, negative contours are dashed lines.

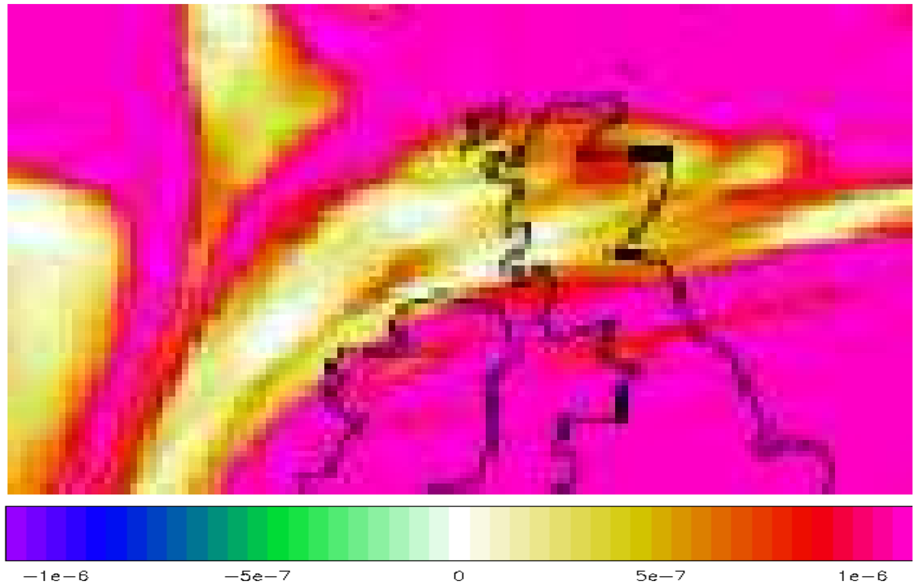

Figure 3.16: Ertel PV at θ=319K from the NAE at 1400UTC on 14 Aug 2008 from initial data at 0000UTC on 14 Aug 2008.

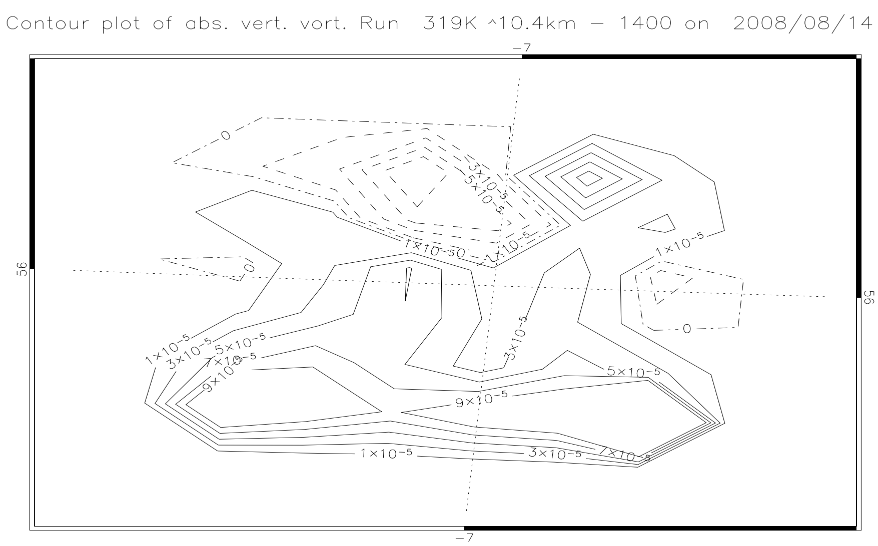

Figure 3.17: Vertical component of absolute vorticity from observational data at 1400UTC on 14 Aug 2008, at resolution (11km, 9.7km). Positive contours are solid lines. Zero contour is dot-dash line, negative contours are dashed lines.

Run	Resolution: with -ζ_a	Resolution: without -ζ_a
1	$(19.8km,\ 17.4km)$	$(24.7km,\ 21.7km)$
2	$(16.8km,\ 15.5km)$	$(20.2km,\ 18.7km)$
3	$(17.0km,\ 15.7km)$	$(20.5km,\ 18.9km)$

Table 3.1: Comparison of the horizontal grid resolution ($\Delta\phi$, $\Delta\lambda$), at each height level, at which evidence of an inertial instability is present and not present in the calculation of the absolute vertical vorticity from observational data.

Table 3.1 shows the resolutions of the calculations either side of the transition zone, at each height level, and figures 3.18 - 3.20 show the absolute vertical vorticity fields either side of this transition zone.

the 2nd order finite-difference calculation to assess at which horizontal grid scale a transition occurs between where the inertial instability is present and when it is not present in the observational data.

A horizontal grid resolution of approximately $20km\times 20km$ appears to be the threshold length scale at which the inertial instability occurs in the atmosphere, therefore, for the inertial instability to be modelled accurately we require a model with resolution much finer the $20km\times 20km$ are arguably much finer than the resolution afforded in the NAE. Furthermore, this also allows us to argue that balanced models should not be run on a scale below around 20-25km, as this is the resolution that the feature of imbalance manifests on.

3.2.4 Validity of vorticity-based balanced models

The high resolution data available from the flight B395 also allowed a more general analysis of the horizontal scale in the atmosphere, above which, the use of vorticity-based, balanced models such as CASL are appropriate.

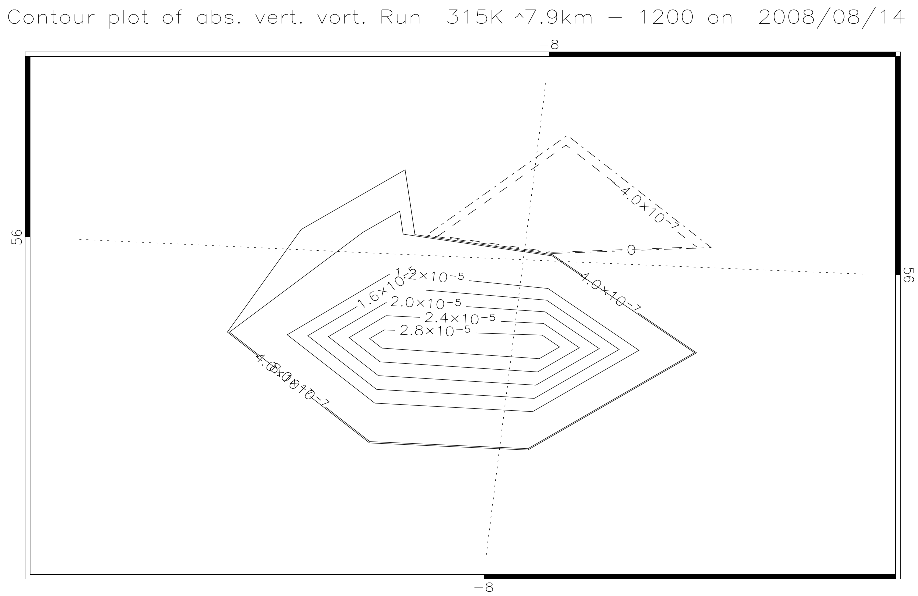

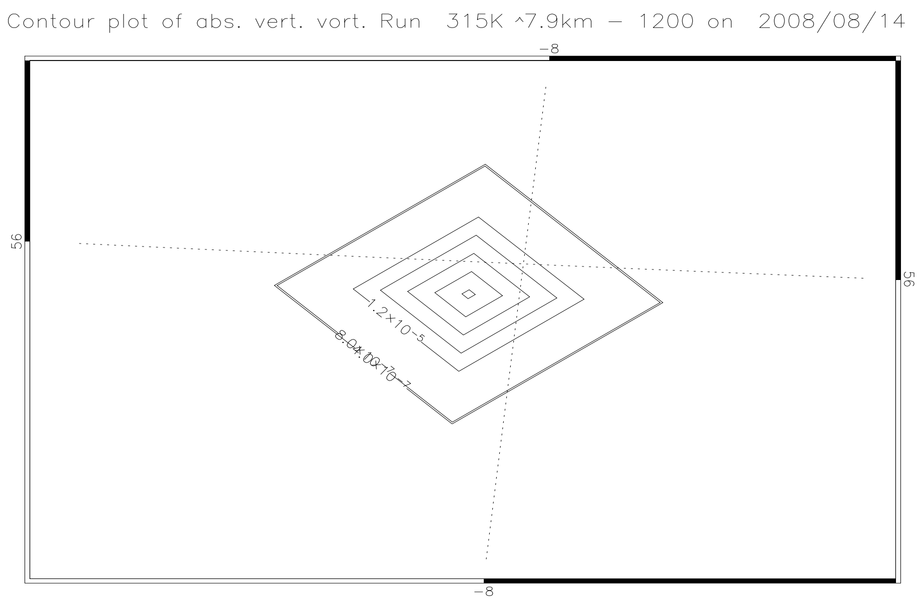

Figure 3.18: Vertical component of absolute vorticity from observational data at 1200UTC on 14 Aug 2008. Above: with negative absolute vertical vorticity, at resolution (19.8km, 17.4km), Below: without negative absolute vertical vorticity, at resolution (24.7km, 21.7km). Positive contours are solid lines. Zero contour is dot-dash line, negative contours are dashed lines.

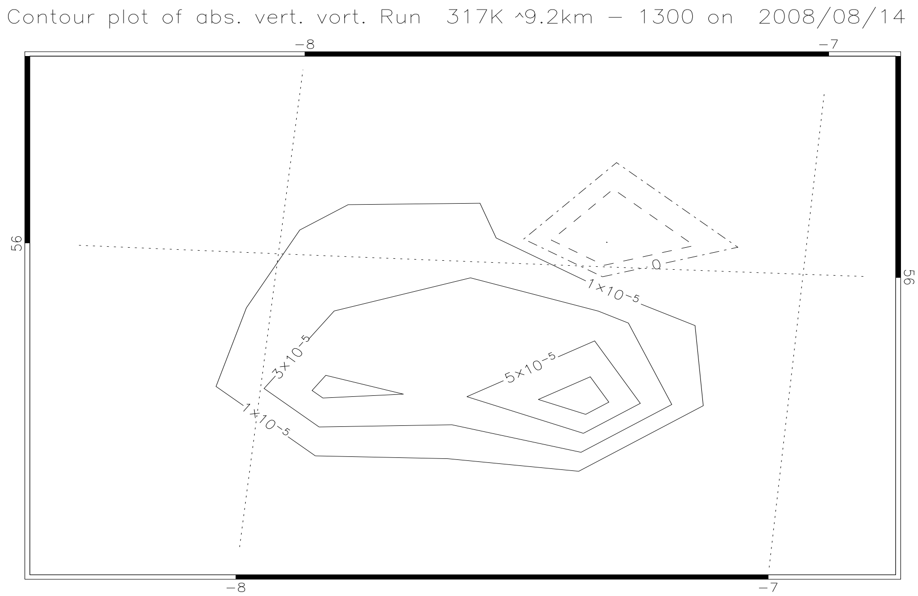

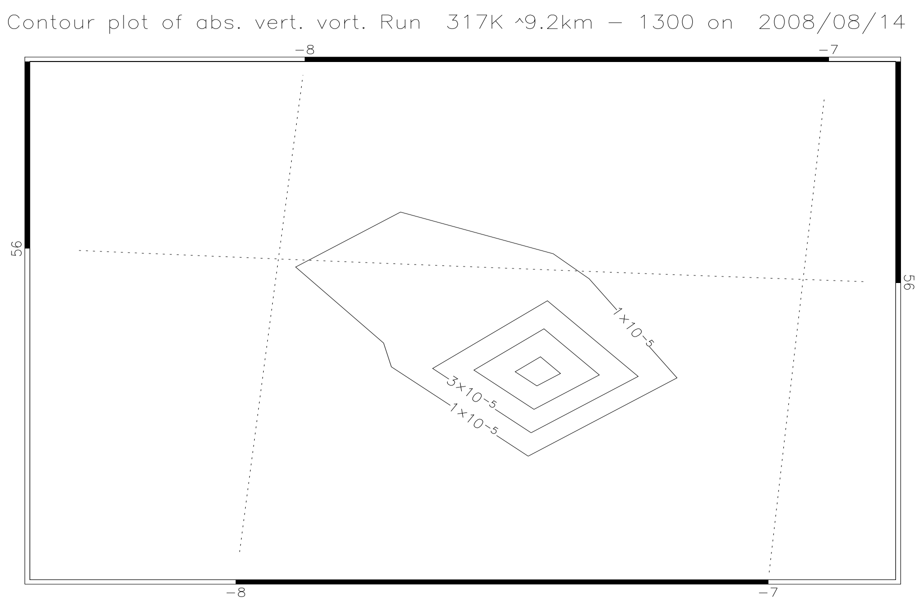

Figure 3.19: Vertical component of absolute vorticity from observational data at 1300UTC on 14 Aug 2008. Above: with negative absolute vertical vorticity, at resolution (16.8km, 15.5km), Below: without negative absolute vertical vorticity, at resolution (20.2km, 18.7km). Positive contours are solid lines. Zero contour is dot-dash line, negative contours are dashed lines.

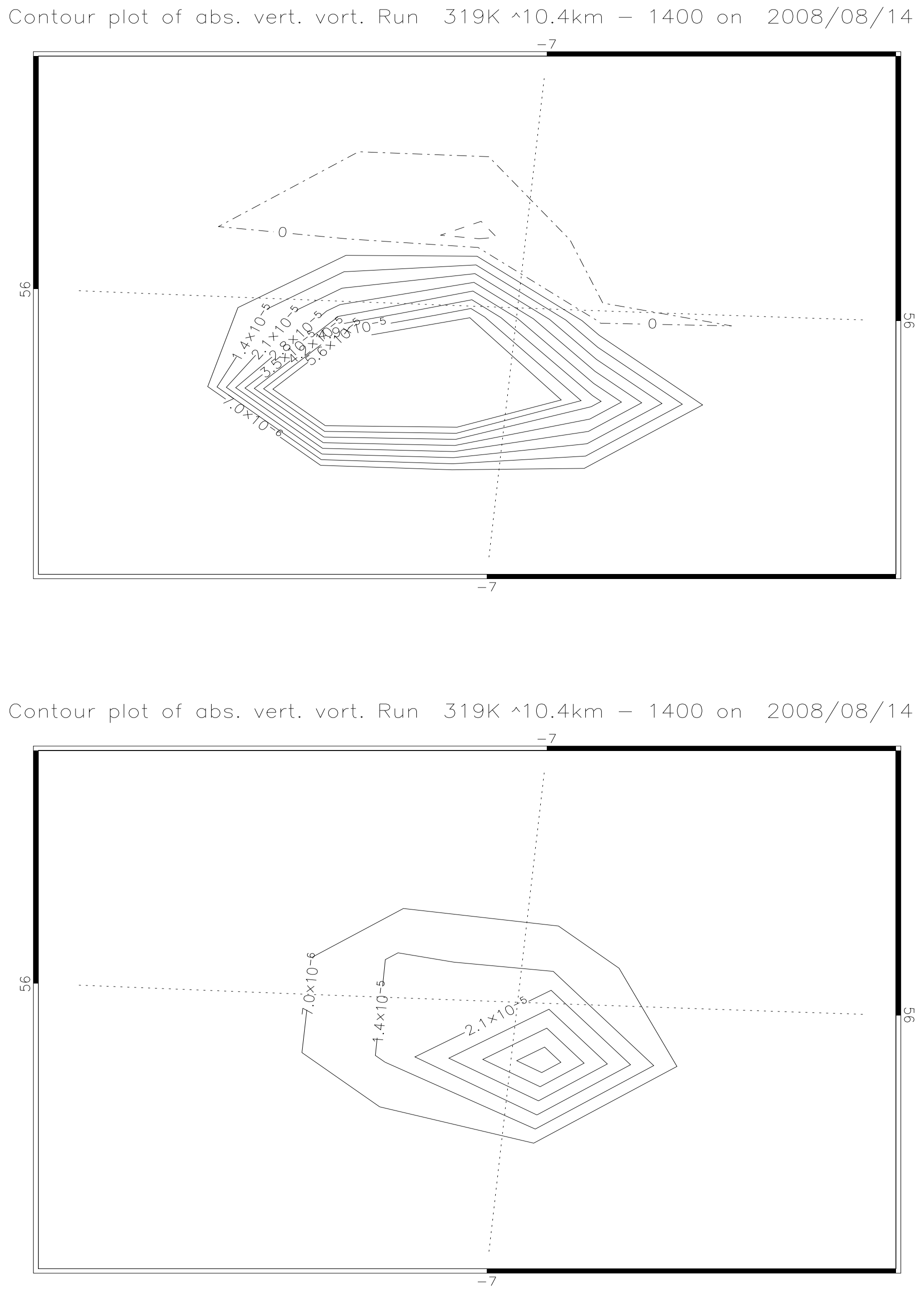

Figure 3.20: Vertical component of absolute vorticity from observational data at 1400UTC on 14 Aug 2008. Above: with negative absolute vertical vorticity, at resolution (17.0km, 15.7km), Below: without negative absolute vertical vorticity, at resolution (20.5km, 19km). Positive contours are solid lines. Zero contour is dot-dash line, negative contours are dashed lines.

At the order of metres the velocity has a small-scale structure. As the vorticity is the spatial derivative of the velocity field at this small-scale there are sharp gradients in the local vorticity field that make their global numerical solution challenging. Therefore, we assess at what scale the vorticity components become ordered in some sense and therefore do not depend on the underlying grid resolution. It is only in this regime that vorticity-based balanced models are valid. Figures 3.21 - 3.23 demonstrate how the root mean square (rms) and domain maximum components of the relative vertical vorticity components ($\zeta = dv/dx - du/dy$) vary with increasing horizontal grid length. On the longer sections of flight B395, runs 7 and 8 (see figure 3.8) the appropriate vorticity component was calculated with a second-order finite difference approximation of the form

$$\frac{dv}{dx} = \frac{v(n+1) - v(n-1)}{2\Delta}, \tag{3.11}$$

where Δ is grid length, with a similar expression for du/dy. The run lengths were approximately $80km$ for runs 7 and 8 at each height level. There was a relatively fine resolution of data available on these runs with a reading taken at approximately every $150m$. The horizontal velocity components were interpolated linearly to the number of grid points desired, from 3 up to the number of data points on each run.

A question of interest is at what horizontal grid scale do the vorticity components stop behaving like $1/2\Delta$. We wish to make some statement in general about this. There is qualitatively and quantatively different behaviour between the $|du/dy|$ and $|dv/dx|$ components at each height level. From figure 3.10 for example, there is a greater wind shear in the y-direction than the x-direction. On leg 7 of each height level there is a clear non-zero shear in $|du/dy|_{rms}$ and this component stops behaving like $1/2\Delta$ in the 3-5km range.

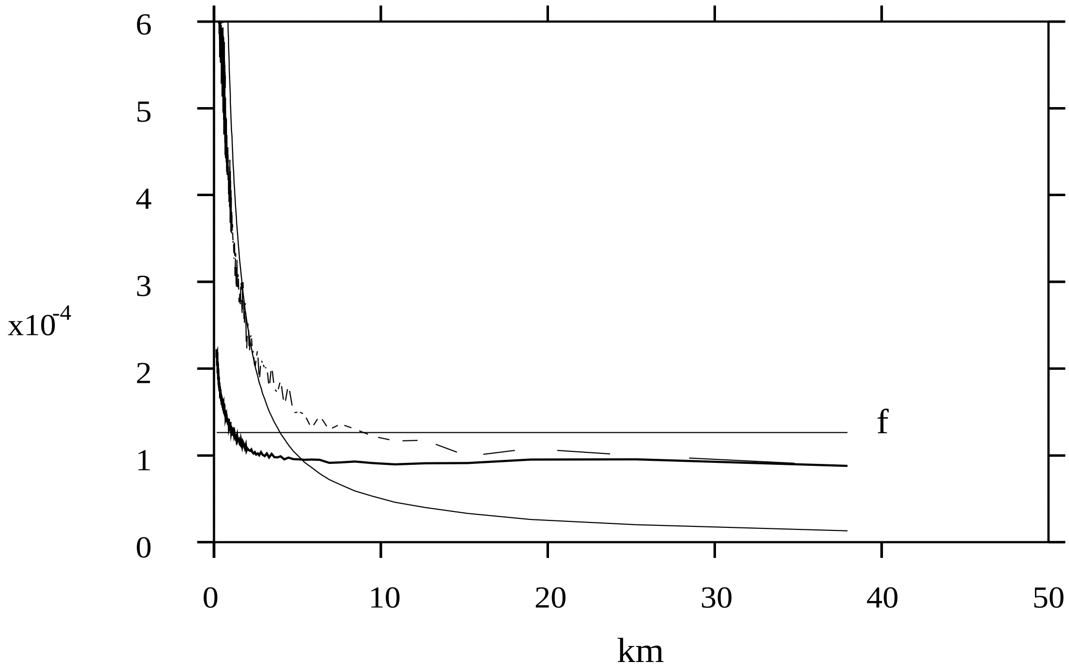

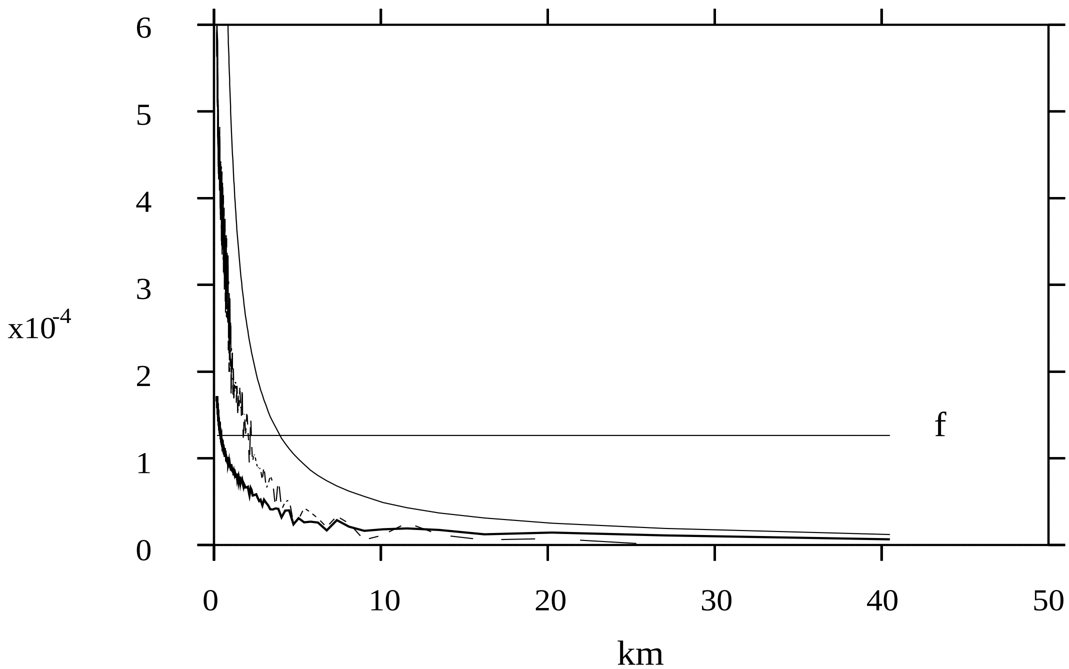

Figure 3.21: At height level 1, ($7.2km$), the variation with respect to the horizontal grid spacing Δ of (top): du/dy_{rms} (bold) and du/dy_{max} (dashed), run 1.7 and (bottom): dv/dx_{rms} (bold) and dv/dx_{max} (dashed) run 1.8. $1/2\Delta$ and the Coriolis frequency are indicated by the thin lines.

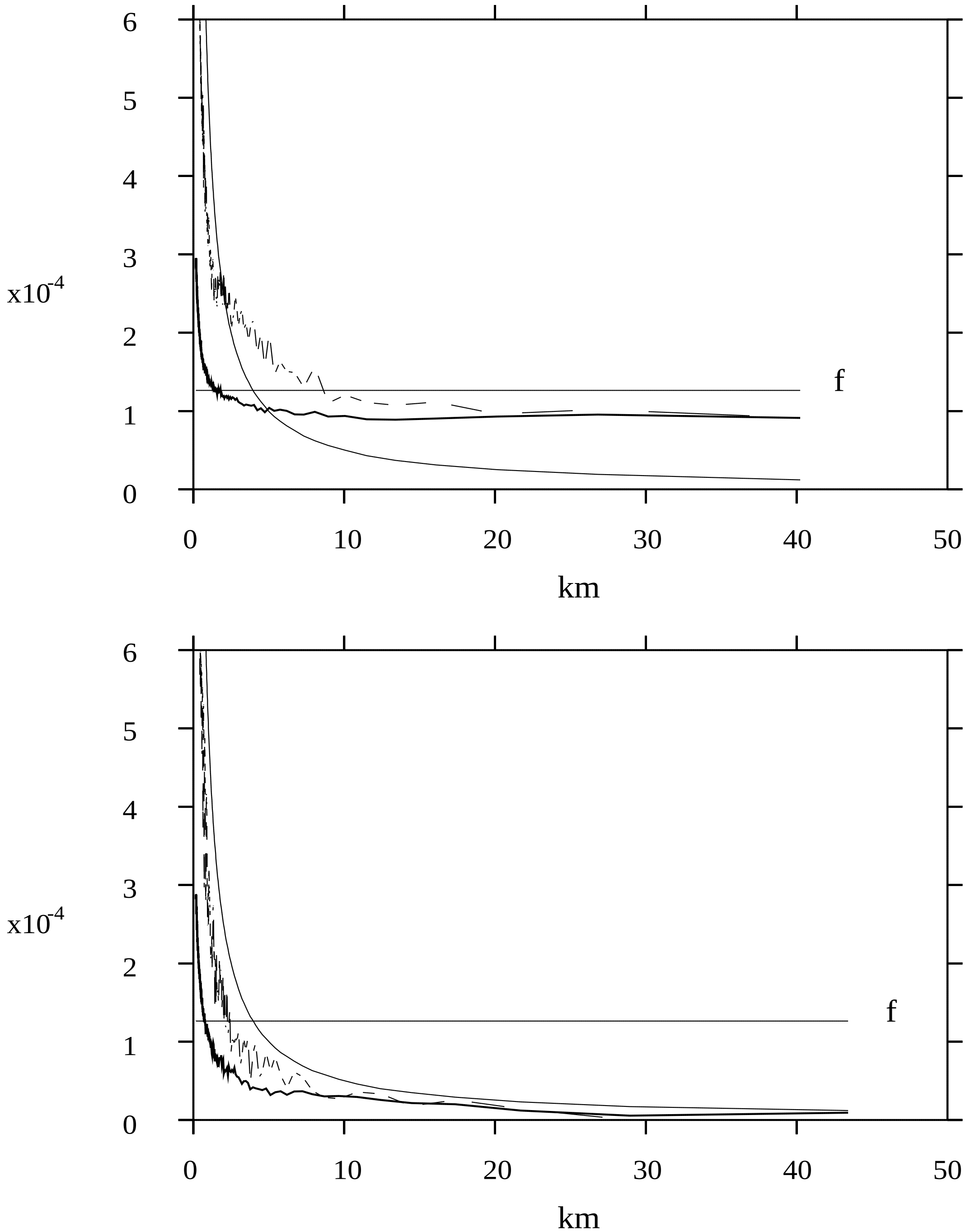

Figure 3.22: As in figure 3.21, at height level 2, $(9.2km)$.

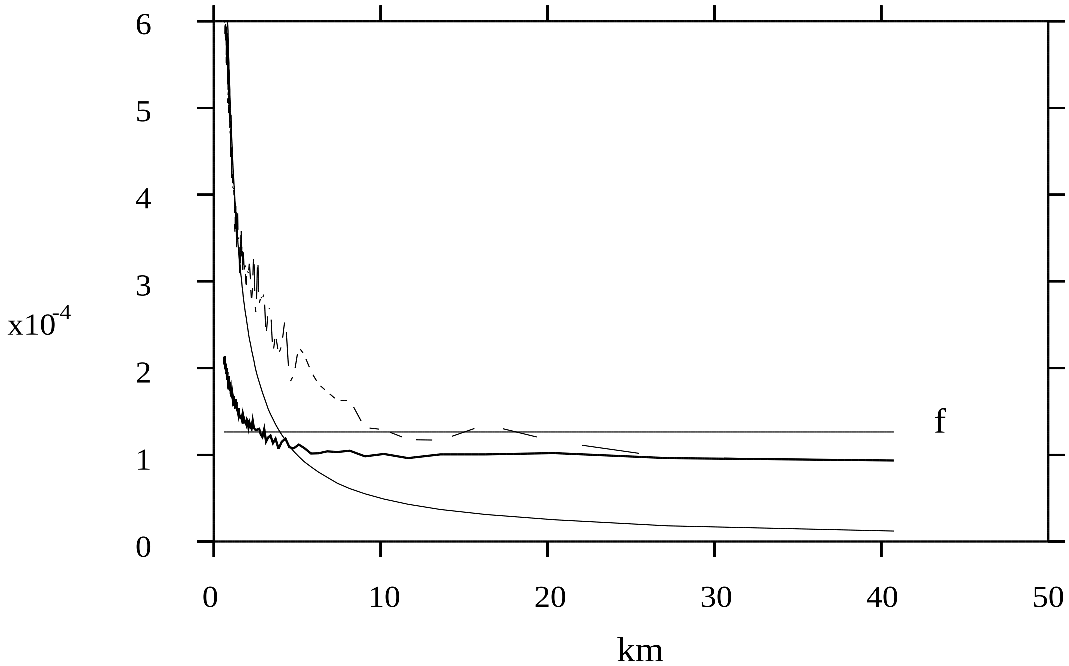

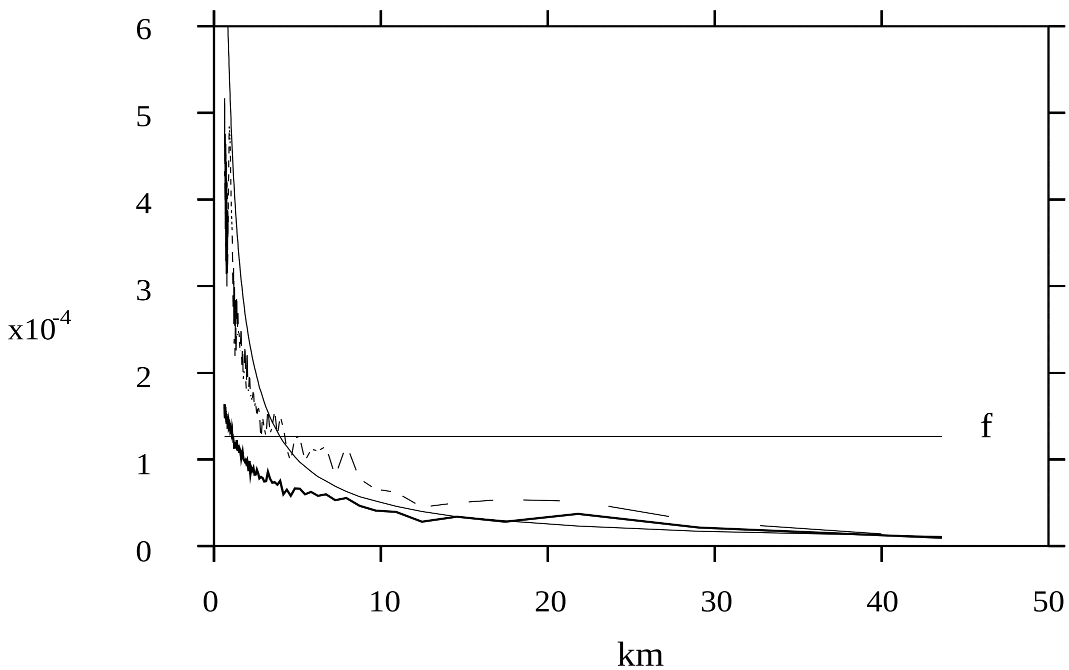

Figure 3.23: As in figure 3.21, at height level 3, (10.4km)

From a horizontal grid scale of $5km$ upwards $|du/dy|_{rms}$ enters a transition zone where values are not so dependent on grid length. Between 10-20km the $|du/dy|_{rms}$ values become more coherent and depend very little on grid length.

As the grid length increases the rms values of each component tend to a constant value between resolutions 10-20km again giving more weight to the claim that vorticity-based balanced models such as CASL should only be employed above 20-25km horizontal grid resolution, as above this resolution the calculation of the vorticity will not depend on the underlying grid.

3.2.5 Impact of data assimilation on symmetric instabilities

The impact of the data assimilation scheme developed and used operationally at the UKMO with the UM, four-dimensional variational assimilation (4D-VAR), Rawlins *et al.* (2007), is assessed as it provides a reference against which the quality of the observational data can be checked. Data assimilation is an analysis technique that incorporates observational data into a previous model forecast to predict an initial state for a current forecast. Briefly, 4D-VAR combines the available observations with a previous six-hour forecast so that dynamical and physical consistency constraints are met between each to produce a model analysis. The assimilation scheme does not explicitly fit the previous forecast to observations, but rather makes estimates of the inevitable errors in both the model fields and observations and acts to minimise these errors, and adjusts the model state to the most probable initial conditions. For practical purposes in this work the data assimilation scheme consisted of two main components, the analysis correction scheme Bell *et al.* (1993) and the incremental analysis updating scheme Clayton (2003). This comparison is not as valuable as using solely observational data as the data assimilation component of the UM comprises of model data plus

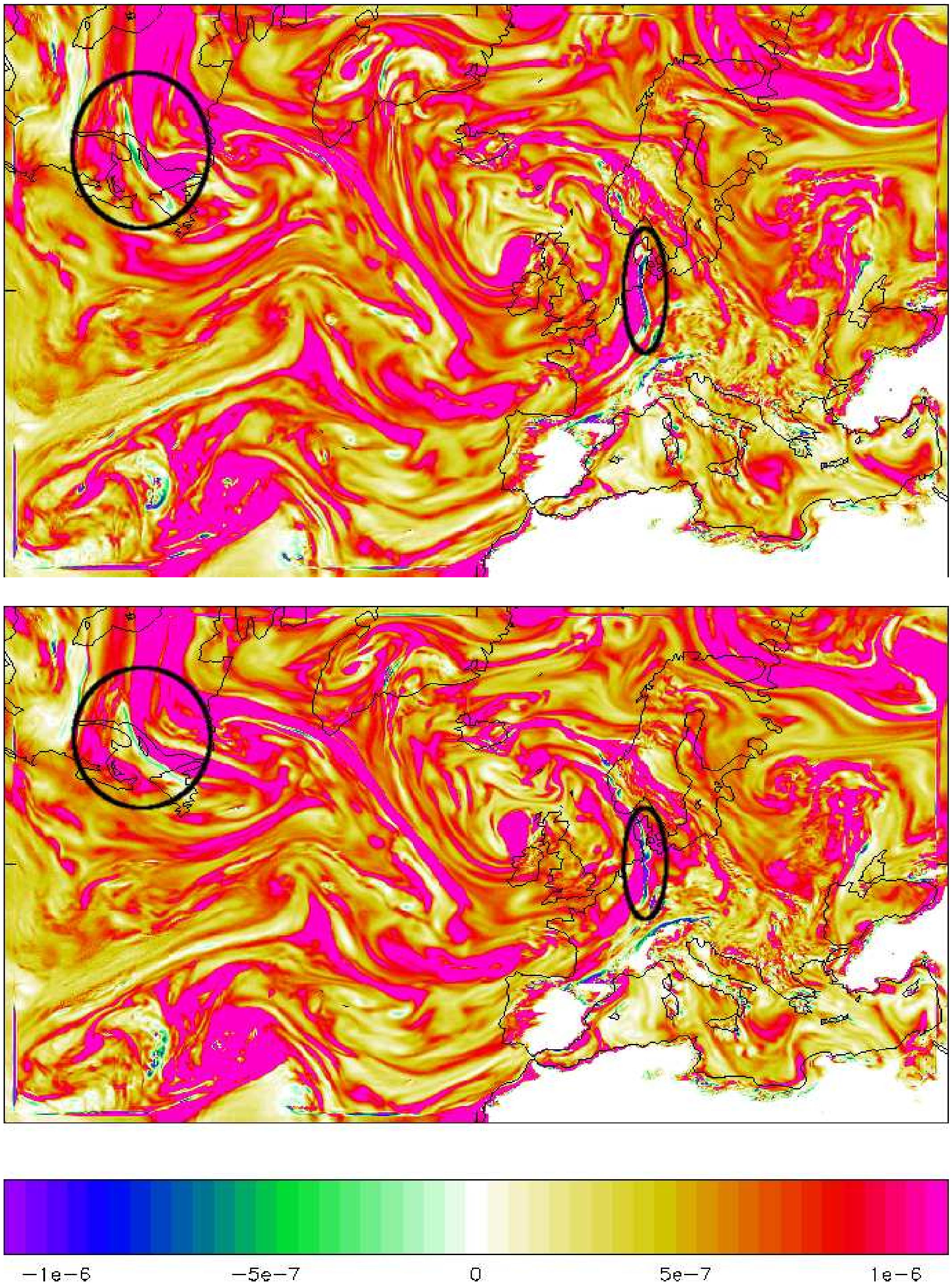

Figure 3.24: Ertel PV at θ=310K from the NAE at 1500UTC on 31 Jul 2006 from initial data at 0000UTC on 31 Jul 2006, *top*: with data assimilation, *bottom*: without data assimilation.

observational data, but still provides a useful insight nonetheless.

Data assimilation in conjunction with the UM runs analysis correction (AC) and incremental analysis updating (IAU), Bloom *et al.* (1996). Simulations have been undertaken with and without data assimilation.

Figure 3.24 shows the Ertel PV field on θ=310K at 1500UTC on 31 July 2006, initialised at 0000UTC on 31 July 2006 from the NAE, with and without data assimilation, respectively. The areas of negative Ertel PV within each figure are consistent and are highlighted within the thick black lines. There has been no significant impact on the areas of negative Ertel PV associated with meteorological features on the synoptic scale. There is no evidence that the data assimilation process within the UM generates these structures spuriously or contributes artificially to their growth. Therefore there is consistent evidence of imbalance of atmospheric flows modelled by the UM. This behaviour was replicated in all comparisons of this nature.

3.2.6 Inter-model comparison: 31 July 2006

It has been demonstrated that the use of observational data to validate numerical predictions of the atmosphere is not entirely suitable in this context due to the lack of high resolution three-dimensional data. Knowledge can be gained through the assessment of areas of negative Ertel PV, by comparing different model resolutions and different initialisation times within the UM.

NAE vs. Global

An example comparing diagnostic output from the UM, from different resolutions within the UM is presented. Figure 3.25 shows an atmospheric pressure chart at 0600 on 31 July 2006 displaying the pressure field corrected for sea-level. Note the trough over the south of England. Figure 3.26 shows the Ertel PV

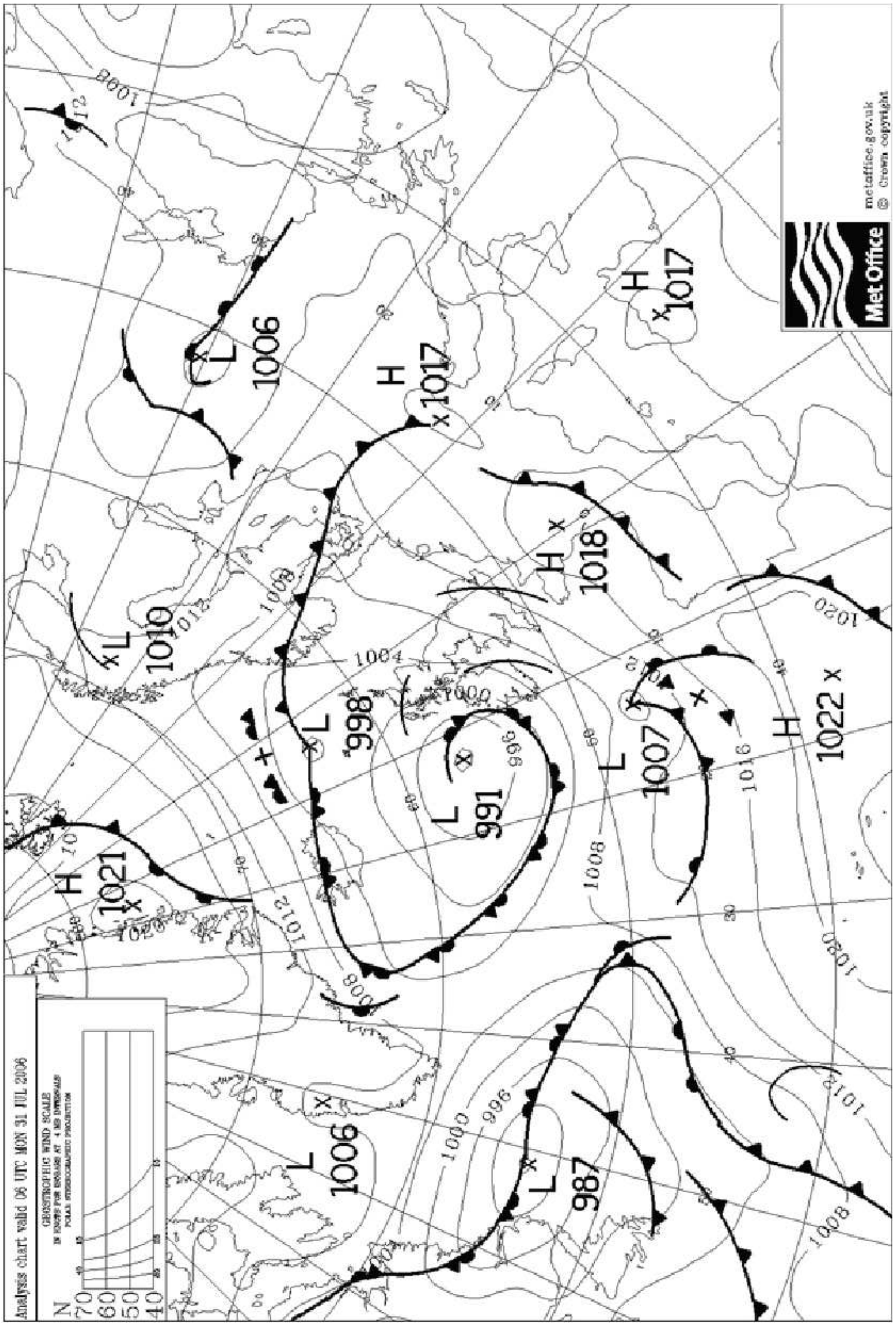

Figure 3.25: Analysis chart displaying the pressure field corrected for sea-level on 31 Jul 2006 at 0600UTC.

field on θ=310K at 0400 on 31 July 2006, from the global model and NAE. Each simulation was initialised four hours previously at 0000 on 31 July 2006. It should be noted that areas of negative Ertel PV commonly manifest at the boundary of LAMs like the NAE, but this evidence is not to be trusted as boundary conditions from larger area models contribute to this component of the diagnostic output field. Attention is given only to areas of negative Ertel PV sufficiently far from the boundary of the NAE.

By observation the Ertel PV fields on θ=310K produced by the global model and NAE are not identical. Attention is drawn to the areas in each field enclosed by the thick black lines. Within each there is a ribbon-like area of negative Ertel PV corresponding to the south of England where the pressure trough was located on the atmospheric chart in figure 3.25. In the NAE simulation there were smaller, localised areas of negative Ertel PV, enclosed by thick white lines. These structures are associated with convective processes. Therefore, areas of negative Ertel PV related to synoptic scale meteorological features like fronts appeared consistently in both the global model and the NAE, whereas the areas of negative Ertel PV associated with mesoscale and sub-grid scale processes like convection appeared in the NAE, but not in the global model. This result confirmed that the UM is capturing atmospheric features at the correct scale, such that mesoscale features like convection are being filtered from the global model solution.

In all simulations where evidence of a ribbon-like area of negative Ertel PV was discovered in the global model it was consistently found in the corresponding NAE simulation. On occasion, evidence of negative Ertel PV was discovered in the NAE, but not in the global model. This evidence was excluded from this study as unreliable as the SI is by nature a high resolution feature, therefore we place more trust in a higher resolution model. So, if initially the global model is analysed and evidence is found then one could claim that evidence of a signal will be found in the NAE, but not vice versa.

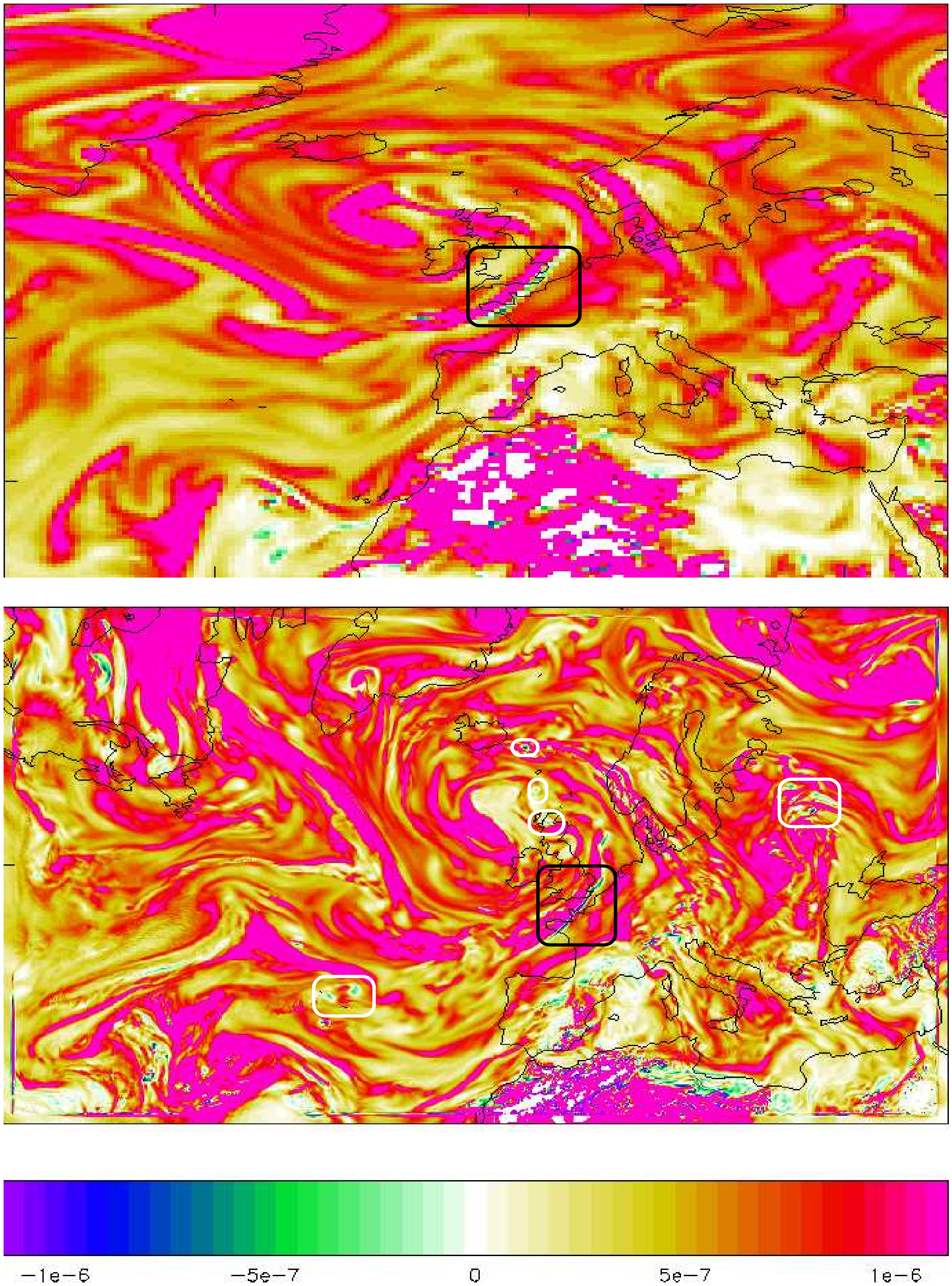

Figure 3.26: Ertel PV at θ=310K from *top*: the global model and *bottom*: the NAE at 0400UTC on 31 Jul 2006 from initial data at 0000UTC on 31 Jul 2006.

Initialisation - Varying when the model is initialised

Another example of consistency between areas of negative Ertel PV, this time within the global component of the UM, is presented. Figure 3.27 shows the Ertel PV field on θ=310K, at 0400UTC on 31 July 2006, initialised at 0000UTC on 31 July 2006 and the result of the same simulation, but with the model initialised at 0000UTC 30 July 2006, twenty-four hours previously. Again, while the fields are not identical there is a good degree of agreement in the synoptic scale feature common to each field to inspire confidence in the diagnostic output of the UM. In each field a ribbon-like strip of negative Ertel PV associated with a front over Scandinavia is highlighted within a thick black line. This structure persists in both simulations but is not as pronounced in the simulation that was initialised twenty-four hours previously. This is evidence that the UM does not generate or amplify these structures spuriously in the initialisation procedure. Another area of negative Ertel PV is highlighted over Greenland in the simulation initialised at 0000UTC on 31 July 2006. It is interesting to note that that this structure does not appear in the output of the simulation that was initialised twenty-four hours previously. This may be of some concern as the UM appears to have filtered this structure from the solution. On the other hand, this feature is not synoptic in scale so one should not be too concerned about this discrepancy. Generally, this behaviour was replicated in all comparisons of this nature, in both the global and NAE.

3.3 Conclusion

In this chapter we have outlined a method of diagnosing indicators of imbalance in the atmosphere, namely, symmetric instabilities (SIs), regions where the Ertel PV is negative (in the Northern hemisphere) when evaluated on isentropic surfaces, with the UM. We found that the UM predicted a relative abundance of these SIs.

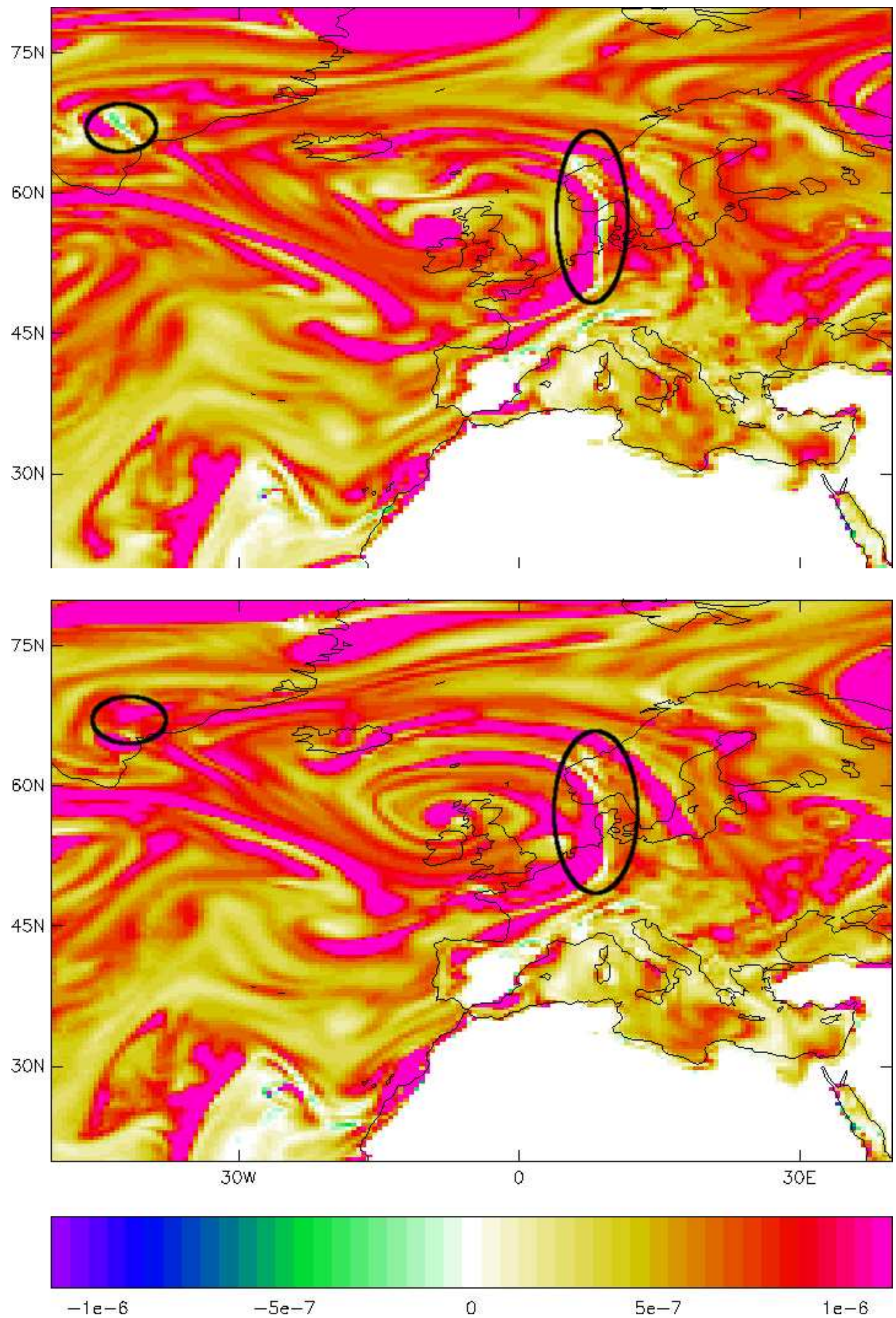

Figure 3.27: Ertel PV at θ=310K from the global model at 0400UTC on 31 Jul 2006 from initial data at *top*: 0000UTC on 31 Jul 2006 and *bottom*: 0000UTC on 30 Jul 2006.

We then assessed that the SIs diagnosed by the NAE and global components of the UM were predominantly inertial in nature. Our intention was to calculate the three-dimensional Ertel PV directly from observations, but these were too sparse to allow a comparison with the global model, particularly in the vertical, so we calculated the two-dimensional vertical component of the absolute vorticity, which if negative would indicate the presence of an inertial instability, the next best option available. Comparisons of observations and the UM were made at equivalent resolutions of the global and NAE components of the UM, $40km$ and $12km$ respectively.

We found no evidence of the atmosphere being inertially unstable at $55km$ resolution but this was almost certainly due to a lack of observational data. At $12km$ we employed relatively fine-scale observational data from a targeted research flight and did find evidence of an inertial instability in the atmosphere at this resolution.

Furthermore, we assessed at which horizontal grid scale the inertial instability was not present in the observational data by decreasing the resolution of the vorticity calculation. We discovered that there is a transition zone at approximately $20km \times 20km$ above which the inertial instability is no present. This indicates that the NAE component of the UM may not be of sufficient resolution to adequately capture an inertial instability in general.

We then used the high resolution aircraft data to estimate a lower bound on the horizontal grid-length scale, above which, balanced models of the atmosphere should not model features of imbalance, of approximately 20-25km. This is an important finding when assessing under what conditions a balanced model such as CASL could operate in an operational NWP context.

Finally, we assessed the data assimilation component of the UM, a combination of model output and observations. This was found to have no significant impact on SIs. We also found that there was a good agreement between different resolutions of the UM regarding the location and nature of the SI. We also observed that varying when the UM is initialised plays no significant role in the location and nature of the inertially dominated, non-convective related occurrence of SIs, so essentially the UM does not artificially 'spin-up' or create the imbalanced features.

In the following two chapters of this thesis we investigate such balanced models in the shallow water and non-hydrostatic under the Boussinesq approximation contexts, and the novel numerical algorithm which generates their solution, the CASL algorithm.

Chapter 4

Robustness of the shallow water CASL algorithm

4.1 Introduction

In this chapter we present results from various shallow water simulations. Initially we focus on the de-centring of the three-time-level semi-implicit semi-Lagrangian time-stepping scheme, used in the contour-advective semi-Lagrangian (CASL) algorithm, Dritschel & Ambaum (1997), to mimic the de-centring of the two-time-level semi-implicit scheme used in the Unified Model (UM) at the UK Met Office (UKMO). We investigate two formulations of CASL, namely, $\mathrm{CA}_{\tilde{h},\delta}$ and $\mathrm{CA}_{\delta,\gamma}$ which differ by the choice of prognostic imbalance variables. We then focus on two cases from each algorithm, exhibiting centred and de-centred integration. An assessment is made of the extent to which each case preserves the vortical-based balanced motion.

We then investigate the operational limits of $\mathrm{CA}_{\delta,\gamma}$ in Ro-Fr parameter space and extend the study to investigate the potential that $\mathrm{CA}_{\delta,\gamma}$ has to become more efficient by reducing computational expense while retaining solution accuracy, as this is a necessity if some form of CASL is ever to be used in an operational NWP context.

4.1.1 De-centring a semi-implicit integration scheme

We de-centre the time integration scheme in the shallow water CASL algorithm and investigate what effect it has on the persistence of balance within a complex and turbulent shallow water flow. In particularly we want to minimise the numerical errors that occur due to the sharp gradients in the PV field that lead to a false breakdown of balance resulting in the spurious generation of imbalance Mohebalhojeh & Dritschel (2000).

The UM used at the UKMO uses a two-time-level semi-implicit semi-Lagrangian scheme as it requires less storage and a forecast time is reached in 50% fewer steps compared to an equivalent three-time-level scheme as successive time-levels in the integration do not overlap, Temperton & Staniforth (1987). This integration scheme is de-centred to combat the spurious semi-Lagrangian orographic resonance outlined in Rivest *et al.* (1994). Tanguay *et al.* (1992) demonstrate that de-centring acts to damp the gravity wave component of the solutions to the shallow water equations. A physical example of orographic resonance is displayed in figure 1.1 in chapter §1. Private communication from Wlasak & Cullen report that de-centring the time integration scheme in the UM improves the balance preservation even in the boundary layer where one may not expect balance to be well preserved.

In anticipation of potentially using CASL in an operational NWP context we investigate the effects of de-centring the time integration scheme of $\mathrm{CA}_{\tilde{h},\delta}$ and $\mathrm{CA}_{\delta,\gamma}$ on the preservation of balance within a flow. The time integration scheme use in the CASL algorithms has three-time-levels as opposed to the two-time-level scheme used by the UM. In practice, the de-centring of the integration scheme results in the following simple analysis. Consider (2.36c)

$$\frac{\partial \tilde{h}}{\partial t} = -\delta - \nabla \cdot (\mathbf{u}\tilde{h}). \tag{4.1}$$

The left-hand-side will be discretised as

$$\frac{\partial \tilde{h}}{\partial t} = \frac{\tilde{h}^{n+1} - \tilde{h}^{n-1}}{2\Delta t} = \bar{\bar{\tilde{h}}}^{n}, \tag{4.2}$$

where $\bar{\bar{\tilde{h}}}^{n}$ represents all terms on the right-hand-side of the equation. If we assume Δt=1 for simplicity then for a centred scheme at the future time, we want to evaluate

$$\tilde{h}^{n+1} = 2\bar{\bar{\tilde{h}}}^{n} + \tilde{h}^{n-1}. \tag{4.3}$$

But when the scheme is de-centred this discretisation becomes

$$\bar{\bar{\tilde{h}}}^{n} = (1-p)\tilde{h}^{n+1} - p\tilde{h}^{n-1}, \tag{4.4}$$

so that

$$\tilde{h}^{n+1} = \left(\frac{1}{1-p}\right)\bar{\bar{\tilde{h}}} + \left(\frac{p}{1-p}\right)\tilde{h}^{n-1}, \tag{4.5}$$

where p is the de-centring parameter. To ensure stability $p \leq$0.5. When p =0.5 the integration scheme is centred and is $\mathcal{O}(\Delta t^2)$ accurate. When $p \neq 0.5$ then the scheme is de-centred and only $\mathcal{O}(\Delta t)$ accurate, cf. (2.5).

This scheme is replicated for the other prognostic equations involving δ and γ that are advanced in time on an Eulerian grid.

Next we outline the initial conditions for our global simulations.

4.1.2 Initialisation

The initial conditions of the flow are replicated from Galewsky *et al.* (2004). They are composed of a balanced, barotropically unstable, mid-latitude jet to which a depth perturbation is added to initiate a global instability. This initial condition captures both the slow balanced motion and the relatively fast IGW motion. Gravity waves are generated in the adjustment process, which proceed to propagate around the globe initially, while the vorticity based motion develops over a few days. The basic zonal velocity is given as a function of the latitude

$$u(\phi) = \begin{cases} 0 & \text{for } \phi \leq \phi_0, \\ \frac{u_{max}}{e_n} \exp\left[\frac{1}{(\phi-\phi_0)(\phi-\phi_1)}\right] & \text{for } \phi_0 < \phi < \phi_1, \\ 0 & \text{for } \phi > \phi_1, \end{cases} \tag{4.6}$$

where u_{max} is the maximum zonal velocity, ϕ_1 is the latitude of the northern boundary of the jet in radians, ϕ_0 is the southern boundary of the jet in radians and e_n is the non-dimensional parameter that normalises the magnitude of the jet to a value of u_{max} at the mid-point of the jet. The set up is as follows: u_{max}=80ms^{-1}, ϕ_0=$\pi/7$, ϕ_1=$\pi/2 - \phi_0$, e_n =exp$[-4/(\phi_1 - \phi_0)^2]$, resulting in the mid-point of the jet located at ϕ=$\pi/4$.

With the basic zonal flow given by (4.6) the balanced height field associated with this jet is obtained through the solution of

$$\tilde{h}_z(\phi) = \mu - \frac{1}{c^2} \int_{-\frac{\pi}{2}}^{\phi} u(\phi')[fa + u(\phi') \tan \phi']\mathrm{d}\phi', \tag{4.7}$$

where a =6.37122 $\times 10^6 m$ is the radius of the Earth and μ is a constant to be found by imposing the condition of zero average $\tilde{h}_z$. In order to initiate the barotropic instability a localised depth perturbation is added to the balanced height field of the form

$$\tilde{h}' = \left(\mu' + \hat{h}\cos(\phi)\exp\left[-(3\lambda)^2\right]\exp -\left[(15(\pi/4) - \phi\right]^2\right)/H, \qquad (4.8)$$

where λ is the longitude in radians, $-\pi < \lambda < \pi$, μ' is a separate constant to be found by imposing the condition of zero average $\tilde{h}'$. The amplitude of the depth perturbation $\hat{h}$ is taken as $120m$. The mean layer depth H is set to $10km$.

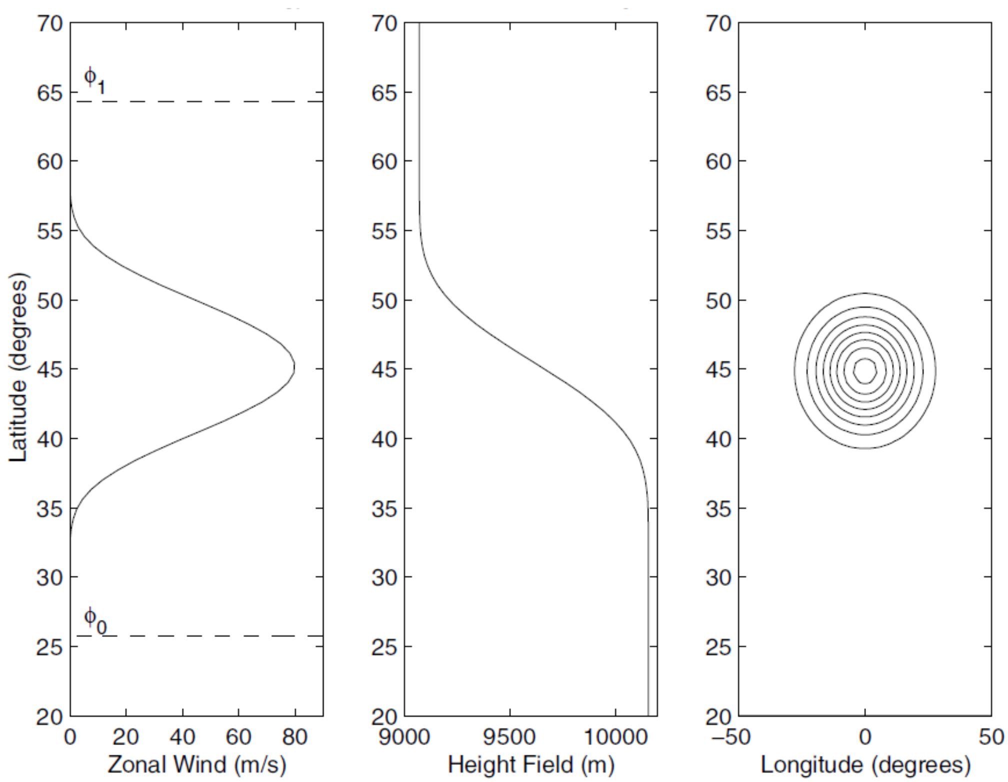

Figure 4.1: The initial profiles from left to right of the zonal velocity, height field and the perturbation depth. From Galewsky *et al.* (2004).

Figure 4.1 shows the latitudinal profiles of the initial zonal flow and the corresponding balanced height field, with a contour map of the depth perturbation. For the CASL algorithms the initial PV is computed from the depth and velocity fields on the grid and then converted to contours with a grid-to-contour conversion algorithm as described in Dritschel & Ambaum (1997).

In this study for convenience length and time are non-dimensionalised by a and $2\pi/\Omega_E$, where Ω_E=7.292 $\times 10^{-5} rads^{-1}$, respectively so that the unit length is the radius of the Earth and the unit of time is one day.

4.2 Results

We performed simulations of CA$_{\tilde{h},\delta}$ and CA$_{\delta,\gamma}$ for values of the de-centring parameter p =0.5, centred and p =(0.4, 0.3, 0.2, 0.1), de-centred. Each simulation was run at 128×128 resolution. A time-step Δt=0.005 was chosen to ensure accuracy. This equated to a Courant number ∼0.54. At this Δt we expect to accurately model the large-scale vortical motions of the flow, but not the relatively faster IGW motions. Therefore, we assume that any small-scale behaviour observed in an imbalanced field, δ or γ, is evidence of spurious IGW motion.

We illustrate four cases CA$^{0.5}_{\delta,\gamma}$, CA$^{0.2}_{\delta,\gamma}$, CA$^{0.5}_{\tilde{h},\delta}$ and CA$^{0.2}_{\tilde{h},\delta}$, where the superscript denotes the value of p the de-centring parameter, to assess the impact of de-centring.

Figure 4.2 shows the evolution of the domain maximum and minimum Rossby numbers where Ro=$\zeta/2\Omega$, and the maximum Froude number, where Fr=$|\mathbf{u}|/\sqrt{gh}$ for each of the four cases. The minimum and maximum Rossby numbers fluctuate and reach maxima around t=6 in the adjustment phase. The maximum Froude number remains almost constant for the simulation.

Figures 4.3 and 4.4 show the evolution of the PV field from CA$^{0.5}_{\delta,\gamma}$, viewed from the equatorial plane and from above the North Pole respectively. This evolution in the PV field was typical for all simulations in each algorithm, centred and de-centred. As de-centring only acts on the imbalanced variables in each algorithm we would not expect to see any change in the dynamics of the large-scale vortical flow. Peak complexity of the flow occurs around t=19, measured by the

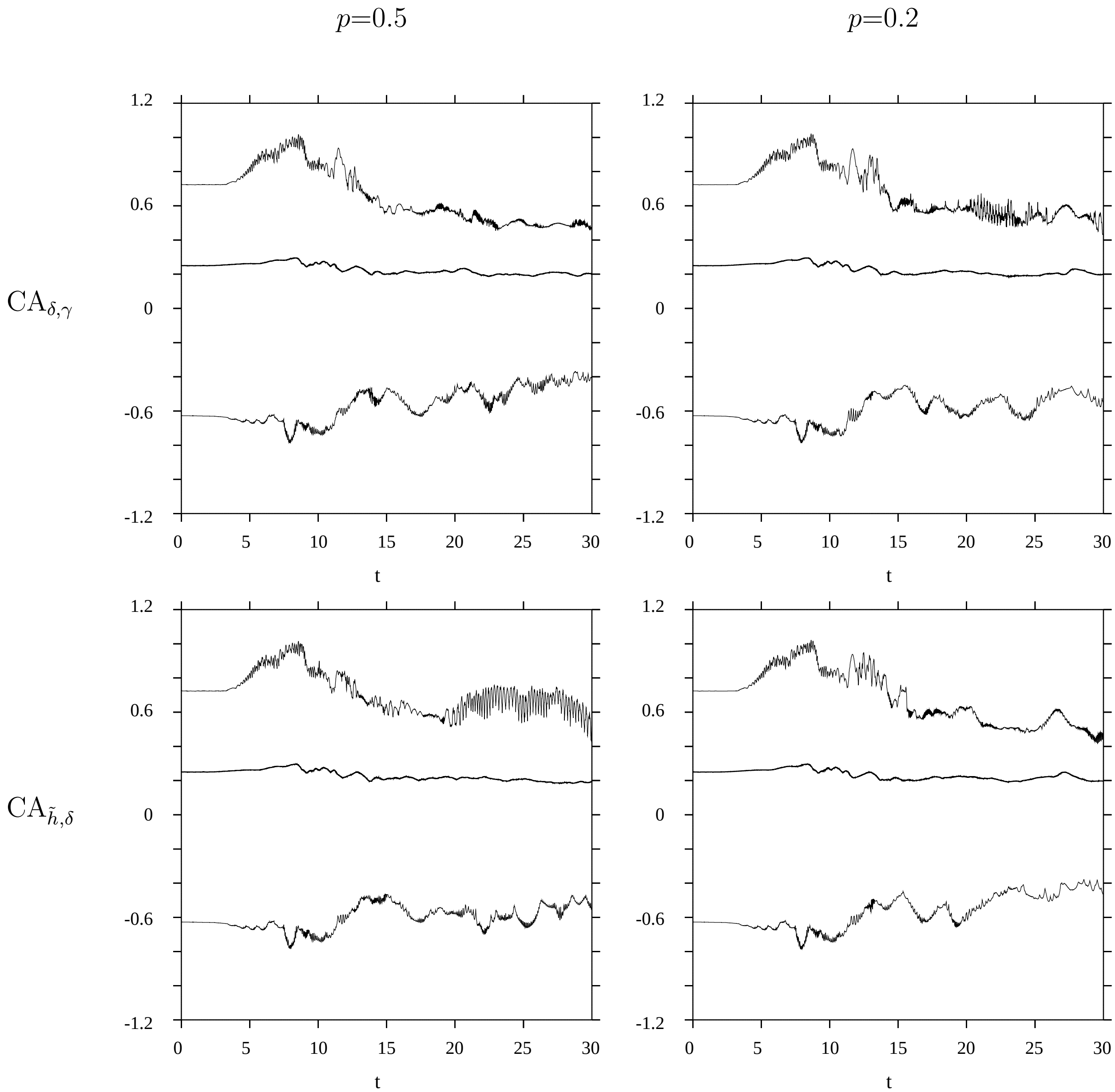

Figure 4.2: Evolution of the minimum and maximum Rossby numbers (thin line) and maximum Froude number (bold line), for top: (left) CA$^{0.5}_{\delta,\gamma}$, (right) CA$^{0.2}_{\delta,\gamma}$ and bottom: (left) CA$^{0.5}_{\tilde{h},\delta}$, (right) CA$^{0.2}_{\tilde{h},\delta}$.

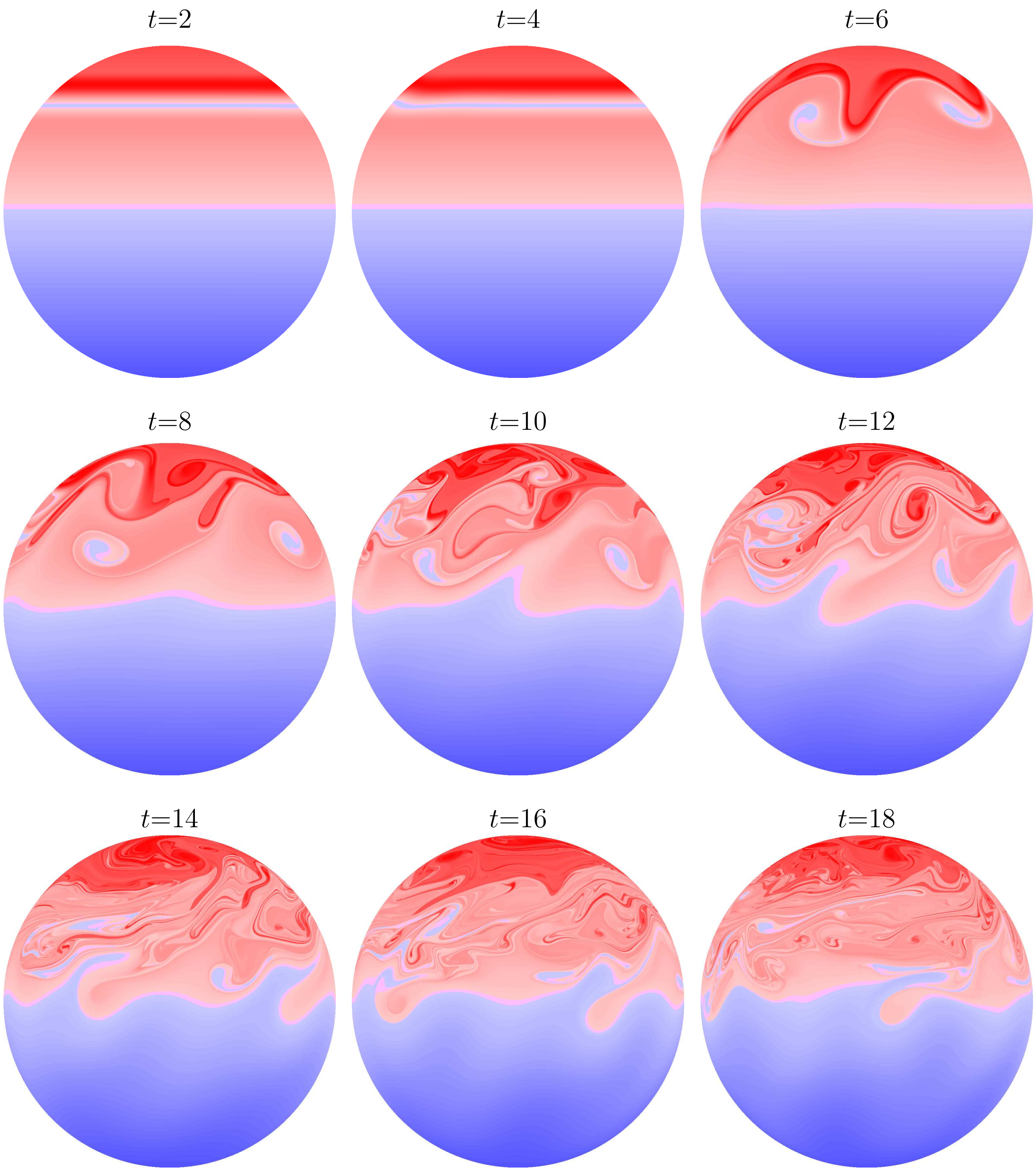

Figure 4.3: Evolution of the PV field, at time t =(2,4,6,8,10,12,14,16,18) *days* from $\mathrm{CA}^{0.5}_{\delta,\gamma}$ viewed in the plane of the equator.

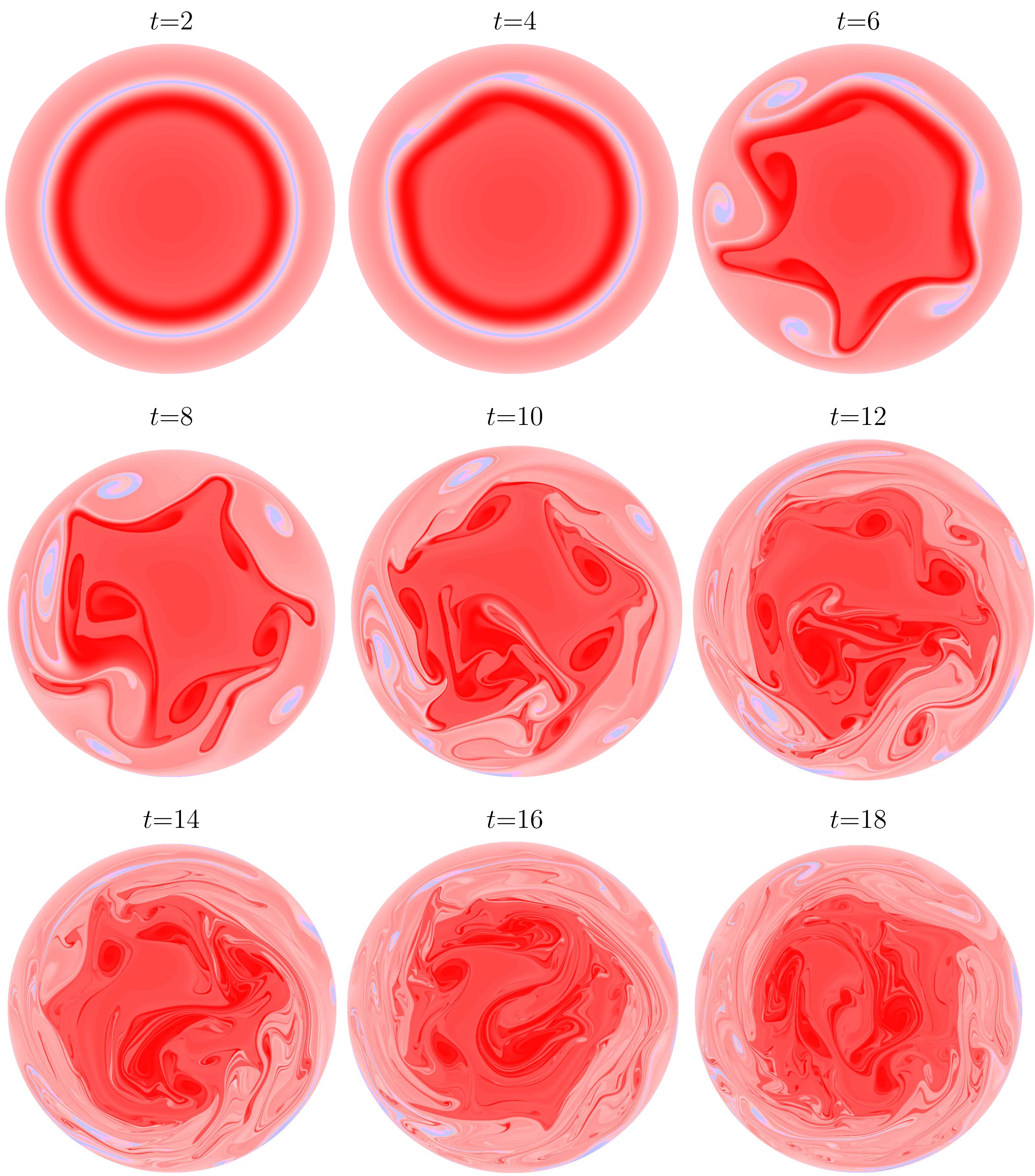

Figure 4.4: As figure 4.3 but viewed from directly above the North Pole.

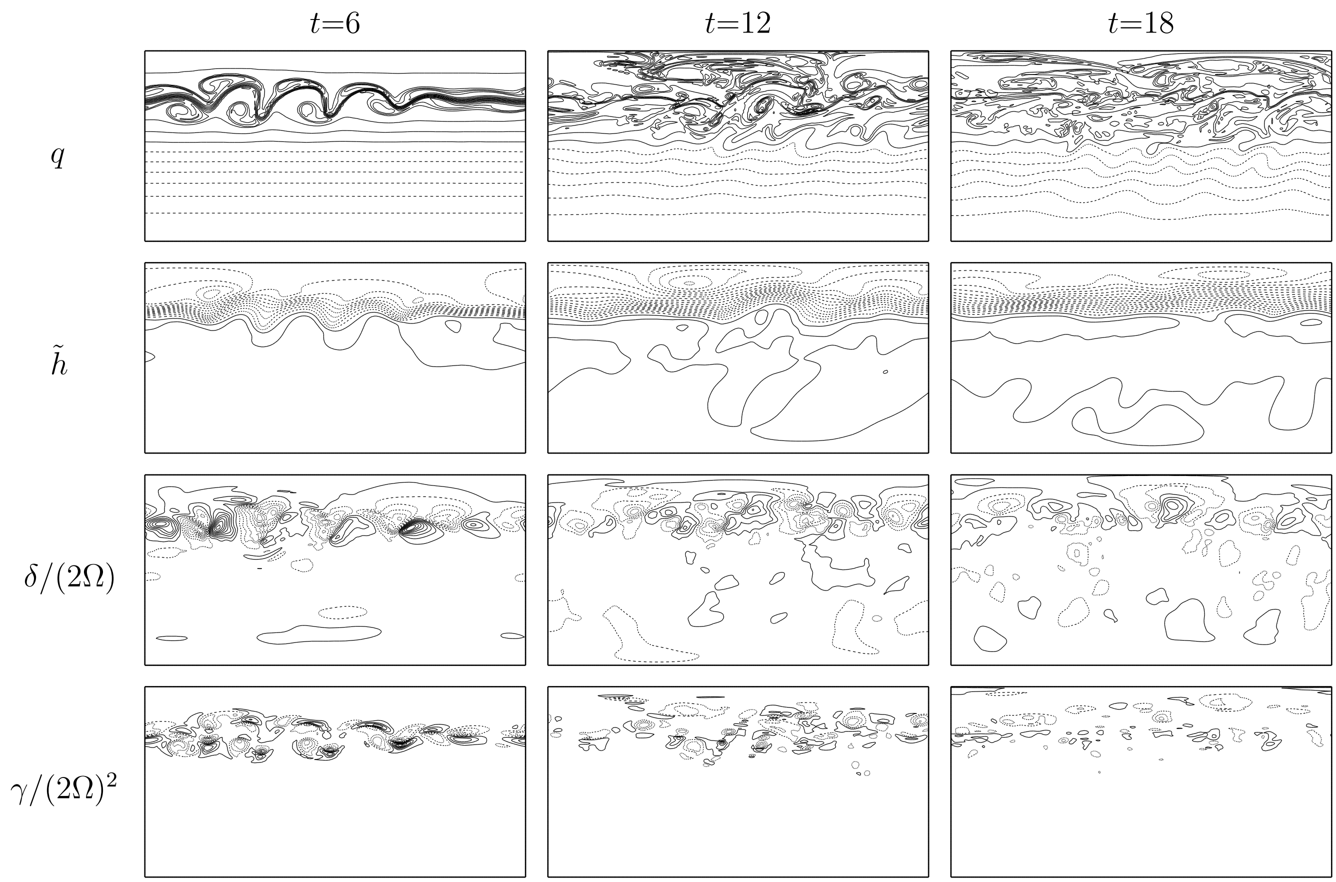

Figure 4.5: From top to bottom row, evolution of q, $\tilde{h}$, $\delta/(2\Omega)$ & $\gamma/(2\Omega)^2$, at times t=6, 12, 18 *days*, for $CA^{0.5}_{\delta,\gamma}$. The contour intervals for each is 2.0 for q, 0.01 for $\tilde{h}$, 0.001 for $\delta/(2\Omega)$ and 0.05 for $\gamma/(2\Omega)^2$.

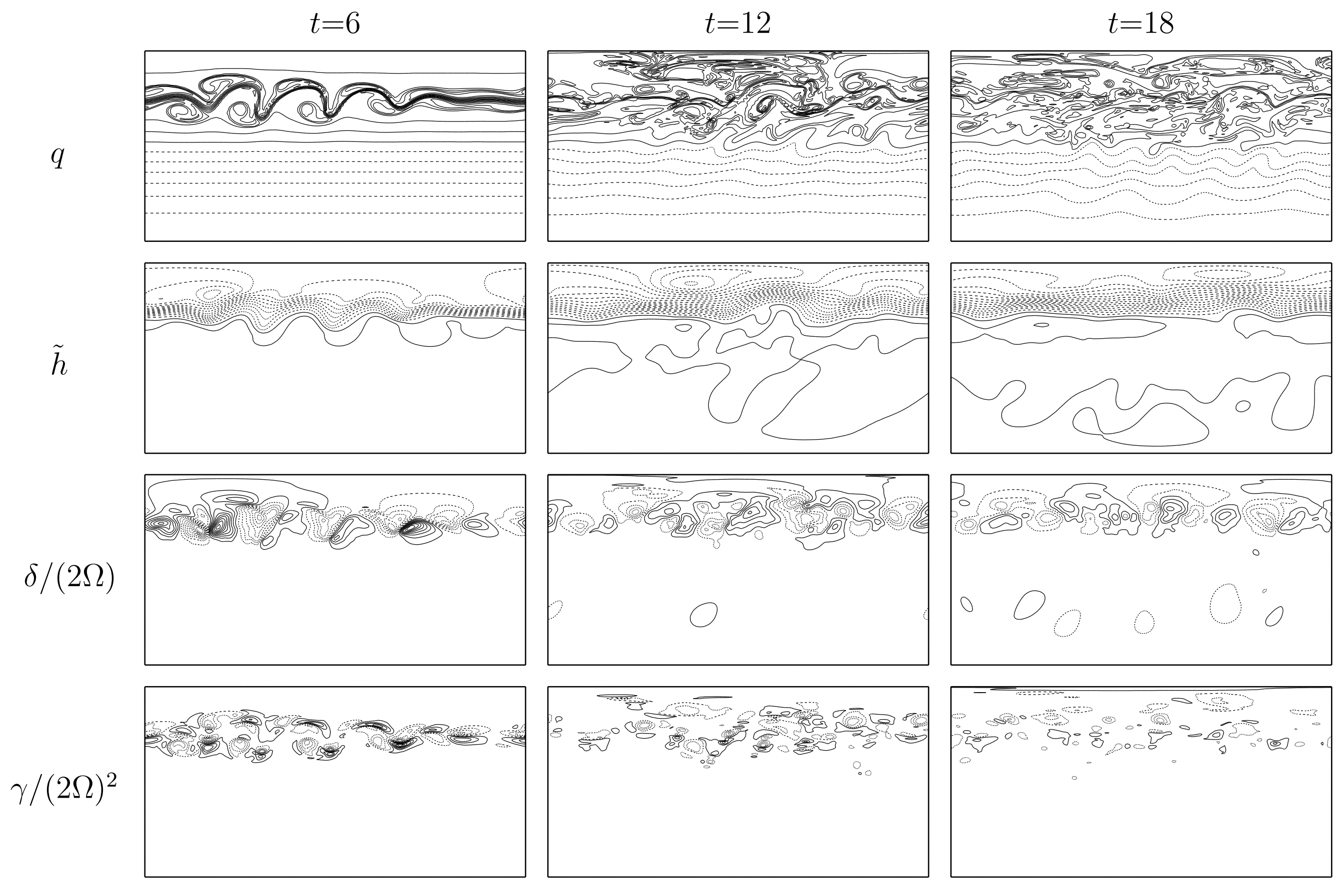

Figure 4.6: As in figure 4.5 for $CA^{0.2}_{\delta,\gamma}$.

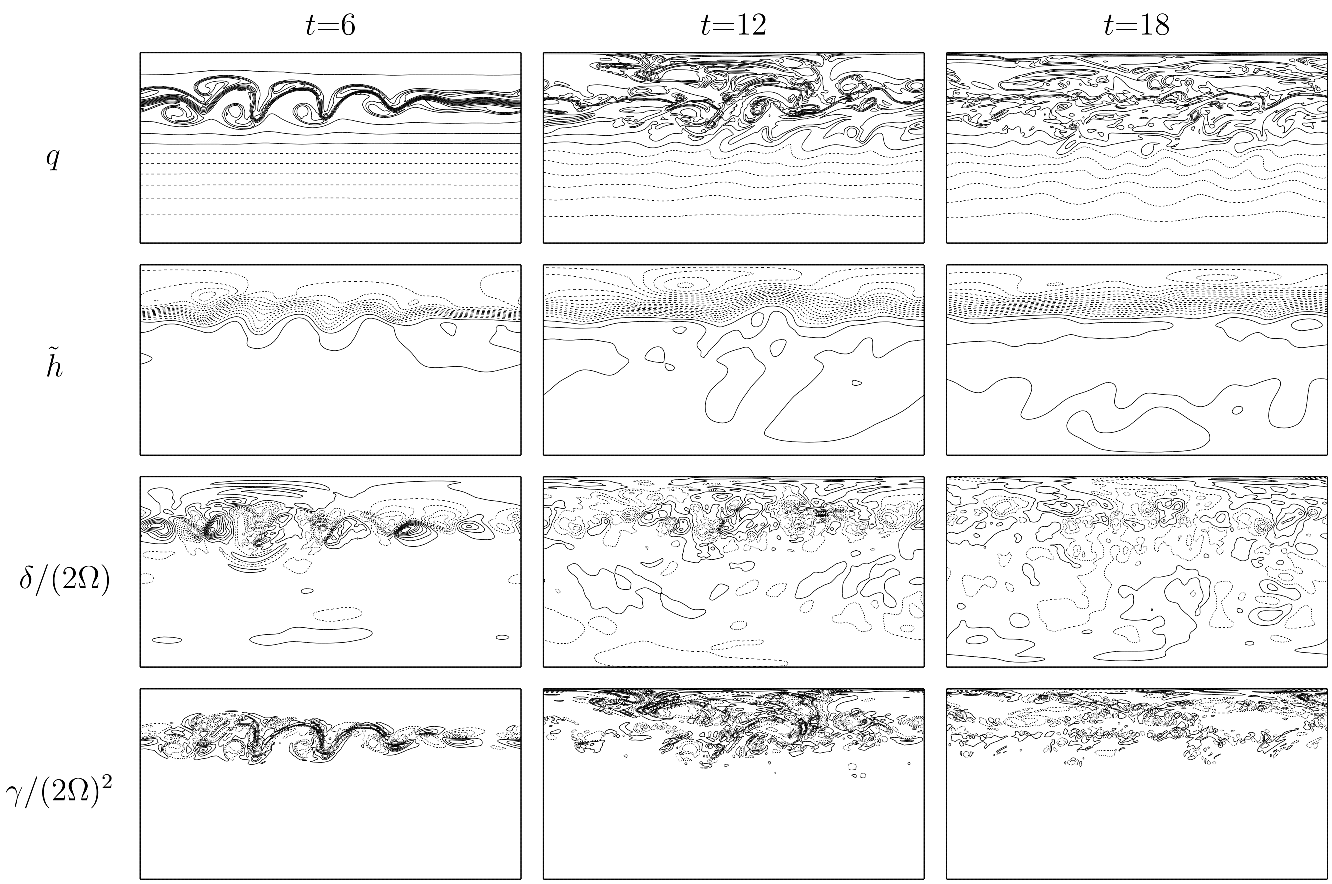

Figure 4.7: As in figure 4.5 but for $\mathrm{CA}^{0.5}_{\tilde{h},\delta}$.

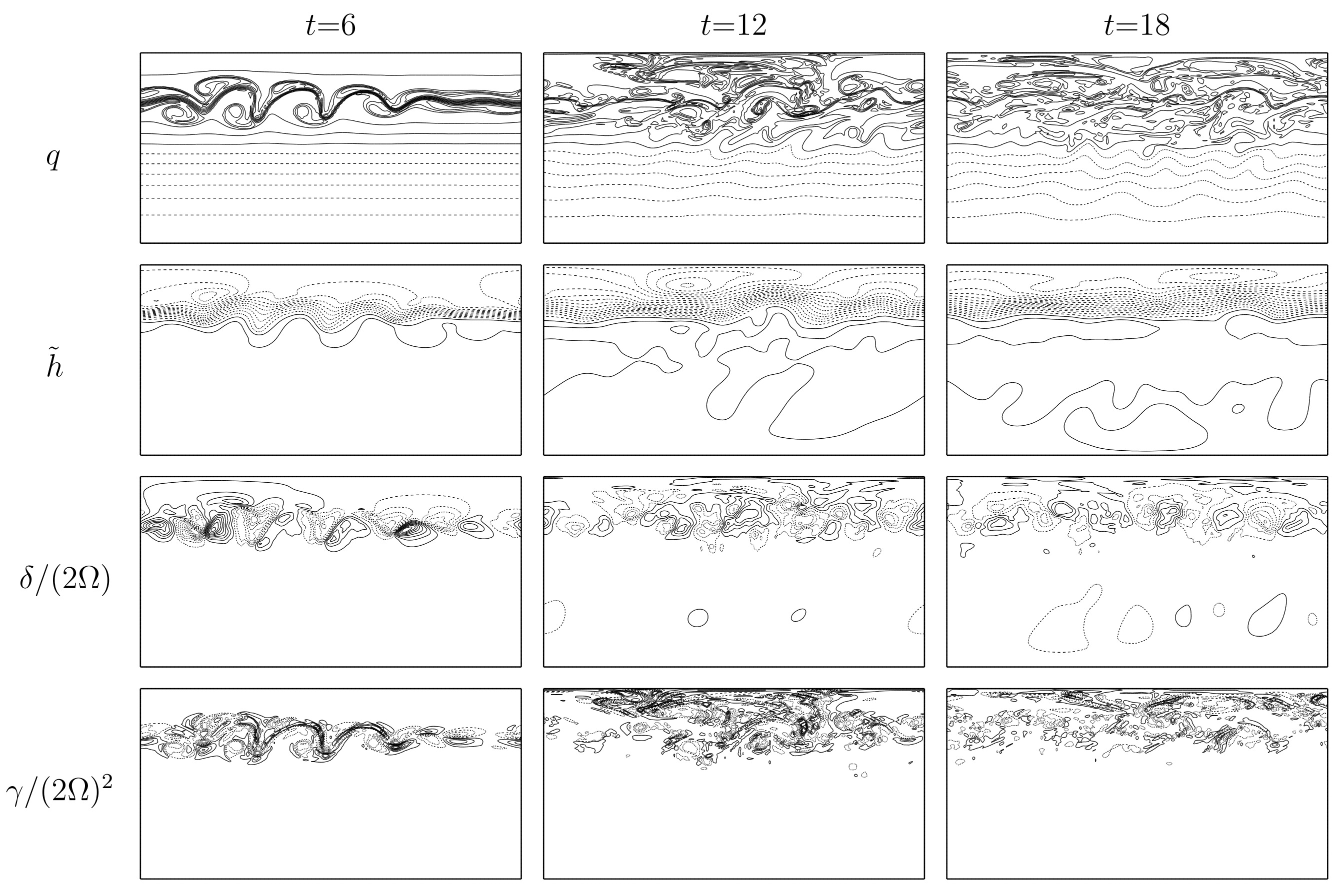

Figure 4.8: As in figure 4.5 but for $CA^{0.2}_{\tilde{h},\delta}$.

maximum number of nodes required to represent the PV contours. From figures 4.2 - 4.4 it is a reasonable assumption that a comparison of various simulations is only meaningful up to around t=15 as the evolution of the flow is chaotic thereafter.

At early times the PV field varies marginally in the Rossby adjustment phase. By t=6 the jet is in the process of rolling up into complex vortical structures. At later times, the PV exhibits sharp gradients and a turbulent, fine-scale filamentary structure.

Figures 4.5 - 4.8 show the contoured PV, depth, divergence and acceleration divergence fields for each of the four cases as indicated. The rectangular domain in each varies from $-\frac{\pi}{2} \leq \phi \leq \frac{\pi}{2}$ and $-\pi \leq \lambda \leq \pi$.

Recall that δ and γ express the departure from geostrophic and hydrostatic balance and so we would expect these fields to be non-zero, but relatively small. Recall that geophysical flows can undergo spontaneous-adjustment emission (SAE) which would be physical motion that we would not wish to damp. The aim is to minimise the *spurious* generation of imbalance.

The most striking difference, common to each algorithm, is the damping of the small-scale structures in the divergence field δ, in the Southern hemisphere, for de-centred simulations. We also note that $\mathrm{CA}_{\delta,\gamma}$ exhibits less of the small-scale imbalanced motions in δ, evidence of IGWs. De-centring has minimised δ in both $\mathrm{CA}_{\tilde{h},\delta}$ and $\mathrm{CA}_{\delta,\gamma}$, but to a greater degree in the latter.

The other qualitative difference between $\mathrm{CA}_{\tilde{h},\delta}$ and $\mathrm{CA}_{\delta,\gamma}$ appears in their representation of the acceleration divergence γ. There is more evidence of imbalance from γ in $\mathrm{CA}_{\tilde{h},\delta}$ as opposed to $\mathrm{CA}_{\delta,\gamma}$. It is not clear that de-centring has had any impact on γ within either model.

As de-centring is a non-scale selective intervention by the modeller a by-product may be that the overall accuracy of the solution may be impaired as the model is dissipating motions at high wavenumbers and reducing the effective resolution of the model. It is unclear if de-centring does more harm than good in the long run. On the other hand, in the work presented here, we reasonably expected most IGW motion to be spurious due to the Δt chosen, so the dissipation observed appears to have had a positive impact on the overall accuracy of the solution.

4.2.1 Bolin-Charney balance

To conclude this section of our analysis we assess how each algorithm minimises imbalanced motions that are present in the flow by analysing the Bolin-Charney balance conditions, Bolin (1955), Charney (1955). These conditions allow a decomposition of the flow at an instant in time to separate the PV controlled balanced motion and the imbalanced IGW component. This analysis has been used in previous studies, Mohebalhojeh & Dritschel (2001), (2004) and is discussed in much more detail in Mohebalhojeh & Dritschel (2009). In practice, once the balanced component of the flow has been diagnosed it can be subtracted from the full shallow water flow to determine the imbalanced component. Following Mohebalhojeh & Dritschel (2009), the quantitative time evolution of imbalance as measured by deviation from the Bolin-Charney balance, obtained by taking the variable Ξ,

$$\Xi = (f\zeta - c^2\nabla^2\tilde{h} - \beta u_\psi) - 2\left[\frac{\partial u_\psi}{\partial \phi}\left(\frac{\partial u_\psi}{\partial \phi} + \zeta\right) + \left(\frac{\partial v_\psi}{\partial \phi}\right)^2\right] - \left(u_\psi^2 + v_\psi^2\right), \quad (4.9)$$

and then setting its first time derivative to zero. Equation (4.9) is the divergence equation (2.36b) where terms involving δ and $\partial\delta/\partial t$ are omitted. The Bolin-Charney balance relation

$$\Xi = 0, \tag{4.10}$$

together with the definition of PV from (2.46), the definition of ψ from (2.39a), and

$$u_\psi = \hat{\mathbf{z}} \times \nabla\psi, \tag{4.11}$$

form a closed system of equations, allowing a PV inversion to determine $\tilde{h}$, ζ, ψ and u_ψ. The balanced component of δ can then be found from

$$\begin{aligned}(c^2\nabla^2 - f^2)\delta = \nabla\cdot(f\mathbf{u}\zeta) - c^2\nabla^2\nabla\cdot(\tilde{h}\mathbf{u}) + \\ 2\frac{\partial}{\partial t}\left[\frac{\partial u_\psi}{a\partial\phi}\left(\frac{\partial u_\psi}{a\partial\phi} + \zeta\right) + \left(\frac{\partial v_\psi}{a\partial\phi}\right)^2\right] + \frac{2}{a^2}(u_\psi\frac{\partial u_\psi}{\partial t} + v_\psi\frac{\partial v_\psi}{\partial t}),\end{aligned} \tag{4.12}$$

where

$$\frac{\partial u_\psi}{\partial t} = \hat{\mathbf{z}} \times \nabla\nabla^{-2}\{\nabla\cdot[(f+\zeta)\mathbf{u}]\}, \tag{4.13}$$

from setting

$$\frac{\partial\Xi}{\partial t} = 0. \tag{4.14}$$

Equation (4.12) can then be solved allowing the determination of δ and $\mathbf{u}$. The balanced fields can then be subtracted from the full shallow water fields to define the imbalanced fields. The L_2 norm for the state vector (u, v, $\tilde{h}$) of the system is defined as

$$||\mathbf{X}|| = \left(\frac{H}{2}\int_{-\frac{\pi}{2}}^{\frac{\pi}{2}}\int_0^{2\pi}[(u^2+v^2) + c^2\tilde{h}^2]\cos\phi \mathrm{d}\phi \mathrm{d}\lambda\right)^{1/2}. \tag{4.15}$$

The imbalance is then measured by

$$||\mathbf{X}_{imb}|| = ||\mathbf{X} - \mathbf{X}_b||, \tag{4.16}$$

where $||\mathbf{X}||$, $||\mathbf{X}_b||$ and $||\mathbf{X}_{imb}||$ are the full, balanced and imbalanced state vectors, respectively.

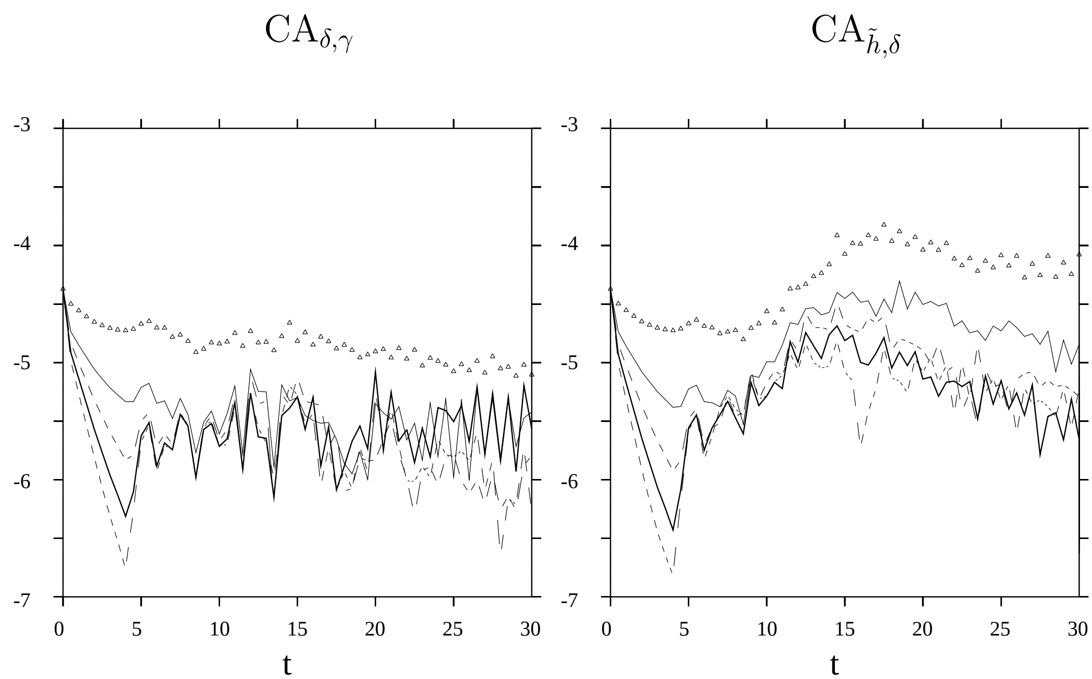

Figure 4.9: Evolution of the log (base 10) squared L_2 of the Bolin-Charney imbalance, $||\mathbf{X}_{imb}||^2$ where, *left*: $\mathrm{CA}_{\delta,\gamma}$, *right*: $\mathrm{CA}_{\tilde{h},\delta}$. Here, p=(0.5, 0.4, 0.3, 0.2, 0.1) are represented by triangles, thin line, long dashed line, bold line and short-dashed line, respectively.

Figure 4.9 shows the evolution of $||\mathbf{X}_{imb}||^2$ for each algorithm, at various values of p. De-centring decreases the imbalanced motions compared to the centred integration for all de-centred values of p. For the centred value of p=0.5, $||\mathbf{X}_{imb}||^2$ is almost identical in each algorithm up to around t=12. At de-centred values of $p \neq 0.5$, $||\mathbf{X}_{imb}||^2$ exhibits no difference up to about t=6, during the Rossby-adjustment phase. Between t=6 to t=12, $\text{CA}_{\delta,\gamma}$ approximately conserves $||\mathbf{X}_{imb}||^2$ while in $\text{CA}_{\tilde{h},\delta}$ the imbalance increases almost linearly in time indicating that $\text{CA}_{\delta,\gamma}$ would be the preferred choice of algorithm to minimise the imbalance while the time integration scheme is de-centred.

From around t=12 onwards, where the flow rapidly become more complex and around t=19, where the peak complexity of the flow is reached in terms of the maximum number of nodes that the algorithms use it is difficult to make any concrete statement as the evolution is chaotic. From t=19 on the surgery routine in CASL is diffusing the flow implicitly through contour surgery.

The smaller the value of p chosen, maximising the effect of de-centring, the more the imbalance is minimised. Caution should be exercised here as taking as small a value of p as possible as a model parameter in practice will have other unwanted, non-scale selective impacts that may damage the overall accuracy of the large-scale vortical motions. There is a balance to be struck in the selection of p to gain the benefits of damping spurious IGW motions, but minimising the harm done to the overall solution in the process. In practice, de-centring decreases the effective resolution of the simulation.

To try and justify the difference in behaviour between $\text{CA}_{\tilde{h},\delta}$ and $\text{CA}_{\delta,\gamma}$ we observe that in $\text{CA}_{\tilde{h},\delta}$ the balance relations, equations (2.36b) and (2.36c) imply that the height field is instantaneously related to the PV field through an elliptic operator as the PV controls the fluid motion in the limit of small Rossby and Froude number. Unfortunately the numerics do not capture this relation and instead the height field is integrated as an independent variable. In the process numerical harmful numerical discretisation errors occur to such an extent that maintaining balance become challenging. To complicate matters the errors show up as erroneous IGWs.

As a result, further investigations of the robustness of the shallow water CASL algorithms will use $\mathrm{CA}_{\delta,\gamma}$ as the prognostic variables employed would be more suited to being de-centred and thus possess more potential for application in an operational NWP context.

4.2.2 Further investigation of $\mathbf{CA}_{\delta,\gamma}$

For a numerical method to be of any practical use in an operational NWP context it must be able to generate an accurate solution that will allow a forecast, in as fast a time as possible, generally before the time that the actual forecast is due. This implies maximising the time-step Δt, almost certainly violating the CFL condition, while not degrading the accuracy of the solution.

Obtaining an accurate solution is challenging especially as features of meteorological interest often occur at Ro and $Fr \sim \mathcal{O}(1)$. An obvious question to be asked of balanced models such as $\mathrm{CA}_{\delta,\gamma}$ is how robust it will be for such flows where greater demands will be placed upon CASL.

4.2.3 General initialisation of a shallow water flow

The initialisation of the PV field is more general than earlier in this chapter. There is no anomaly in the depth field for a zonal jet to interact with. Instead, we introduce two perturbations to the initial flow.

The Cartesian coordinate system is rotated by a small perturbation angle about the y-axis, in the equatorial plane. Denoting the principal coordinate axes as (X, Y, Z), this system is rotated in a clockwise direction about the y-axis by a perturbation angle. The transformation is

$$\begin{pmatrix} X' \\ Y' \\ Z' \end{pmatrix} = \begin{pmatrix} \cos\alpha & 0 & \sin\alpha \\ 0 & 1 & 0 \\ -\sin\alpha & 0 & \cos\alpha \end{pmatrix} \begin{pmatrix} X \\ Y \\ Z \end{pmatrix}, \tag{4.17}$$

where α=0.01rad. Therefore in the transformed coordinate system

$$X' = \cos\alpha\cos\phi\cos\lambda + \sin\alpha\sin\phi, \tag{4.18a}$$

$$Y' = \cos\phi\sin\lambda \quad (\equiv Y), \tag{4.18b}$$

$$Z' = -\sin\alpha\cos\phi\cos\lambda + \cos\alpha\sin\phi. \tag{4.18c}$$

The initial PV field is computed from the initial velocity and depth fields from (2.38) and is then converted to contours on this displaced coordinate system. When the simulation commences on the principal coordinate system the PV contours are displaced slightly in the meridional direction, causing a rapid destabilisation of the PV. To manipulate this destabilisation of the flow we obtain a perturbed PV field of the form

$$q_p = q + \varepsilon\left[\left(\frac{f+\zeta}{1+\tilde{h}}\right) - f\right]\sin(6\lambda), \tag{4.19}$$

where ε=0.005 and λ is the longitude, giving a wavenumber 6 decomposition of the initial zonal jet.

4.2.4 Results

We surveyed a range of initial jet speeds and jet positions and mean depths on the globe and present two cases, a mid-latitude jet (ϕ=$\pi/4$) with an initial jet speed of 60ms^{-1} and an equatorial jet (ϕ=0) with an initial speed of 80ms^{-1}, each with a mean depth of 1km. All simulations in this section were at 256×256. These cases would allow the testing of geophysical activity at different locations on the globe and would highlight the potential difficulties in modelling the dynamics in the equatorial region, where $f \to 0$. A mean depth of $1km$ was chosen to mimic the effect of increased effective stratification of the flow, by decreasing the characteristic height scale of the flow. One may also think of the $1km$ depth as simulating dynamics in the boundary layer.

For stability in the method we had to employ a successive under relaxation method for the solution of the modified Helmholtz equation (2.48)

$$(c^2\nabla^2 - f^2)\tilde{h}^{n+1} = f(\zeta - f\tilde{h}^n) - \beta u - \gamma. \tag{4.20}$$

This equation is solved iteratively for $\tilde{h}^{n+1}$ on the left-hand-side using previous iterates. The left-hand-side of this equation is inverted to obtain the depth at the future time, $\tilde{h}^{n+1}$. Here an extra step is added of the form

$$\tilde{h}^{n+1} = 0.3\tilde{h}^n + 0.7\tilde{h}^{n-1}, \tag{4.21}$$

so that the updated depth field is composed of a combination of the two previous iterates, not just the previous one.

Figure 4.10 shows the evolution of Ro_{max}, Ro_{min} and Fr_{max} and table 4.1 gives a summary of these parameters, along with their time-averaged values over the 30 day duration of the simulation.

Each case is chosen as an example of the current operational limits of the algorithm. For increased initial jet speeds and decreased mean depths, CASL proved unstable. Each case exhibits Ro and $Fr \sim \mathcal{O}(1)$ providing the numerics of CASL a severe test, crucially at values of Ro and Fr of interest in operational NWP. This is a point already highlighted by the need for a successive under relaxation scheme for the inversion relation for the depth field.

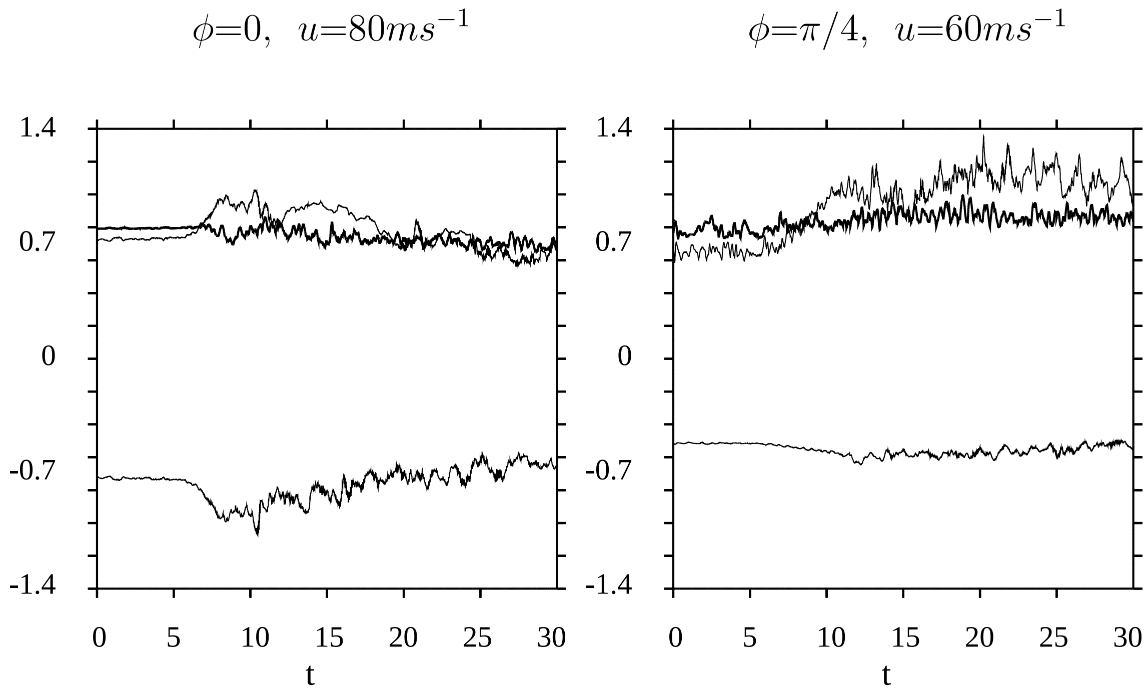

Figure 4.10: Evolution of the minimum and maximum Rossby numbers (thin line) and maximum Froude number (bold line), for CA$_{\delta,\gamma}$ for, *left*: u=80ms^{-1}, ϕ=0, and *right*: u=60ms^{-1}, ϕ=$\pi/4$.

Initial jet	Ro_{min}	Ro_{max}	$Ro_{max}(\bar{t})$	Fr_{max}	$Fr_{max}(\bar{t})$
u=80ms^{-1}, ϕ=0	-1.08	1.02	0.78	0.86	0.74
u=60ms^{-1}, ϕ=$\pi/4$	-0.64	1.35	0.94	0.99	0.84

Table 4.1: For each initial jet, the maximum and minimum Rossby numbers, the maximum Froude number, and the time-averaged maximum Rossby and Froude numbers

Figures 4.11 and 4.12 show the evolution of the PV field for the initial jet u=60ms^{-1}, ϕ=$\pi/4$ as viewed from the equatorial plane and the North Pole respectively. Qualitatively, the behaviour of the PV field is similar to the initial condition from Galewsky *et al.* (2004), from the earlier part of this chapter. The main difference now is the formation and persistence of intense vortices even at later times of the simulation.

The contour plots of the PV, depth, divergence and acceleration divergence in figure 4.13 all exhibit sharp and steep gradients, unlike the corresponding fields that were simulated earlier in this chapter.

Figure 4.14 shows the evolution of the PV field for the initial jet u=80ms^{-1}, ϕ=0, as viewed from the equatorial plane. Qualitatively, the dynamics of the equatorial jet differ from that of the mid-latitude jet. At t=10 the flow is undergoing adjustment and vortices are starting to form near the mid-latitudes in each hemisphere, but these structures do not persist for long as mixing occurs within the flow. The dominant behaviour here is a Kelvin wave about the equator.

The PV, depth, divergence and gamma fields in figure 4.15 now exhibit a greater extent than the corresponding fields for the the mid-latitudinal jet while exhibiting a similar small-scale structure in the imbalanced variables field.

We now consider in turn how increasing Δt and reducing the convergence criteria of the modified Helmholtz equation, (4.20), impacts on the accuracy of the solution.

Increased Δt

Both of the cases outlined will provide a stern test of the numerics of the CASL algorithm. To test the numerics even further we increase the time-step Δt of the model. In operational NWP we wish to achieve a solution in as quick a time as possible. One way to decrease the computational time a simulation requires is to

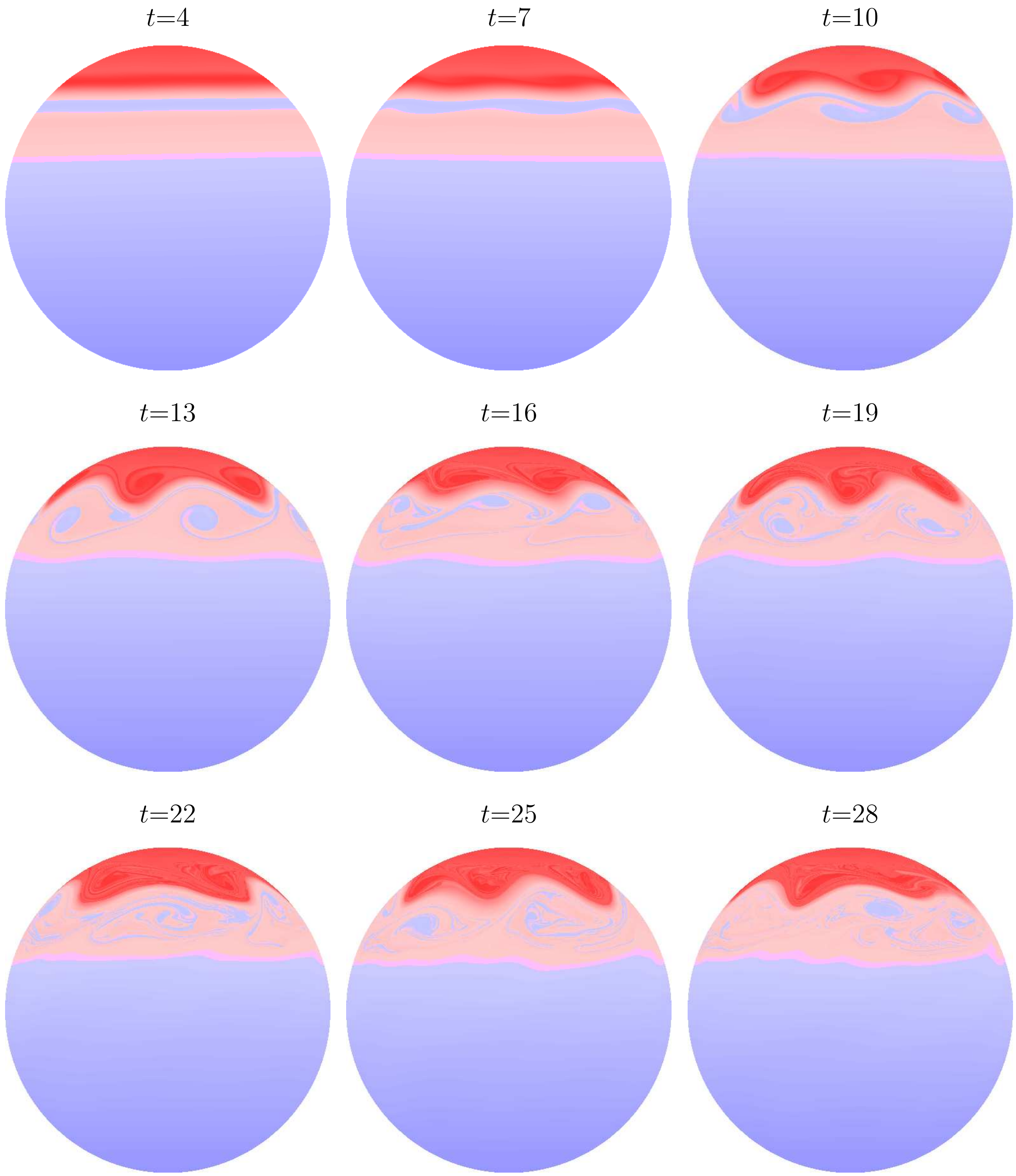

Figure 4.11: The evolution of the PV field, at time t=(4,7,10,13,16,19,22,25,28) *days*, with initial u=60 ms^{-1}, ϕ=$\pi/4$ viewed in the plane of the equator.

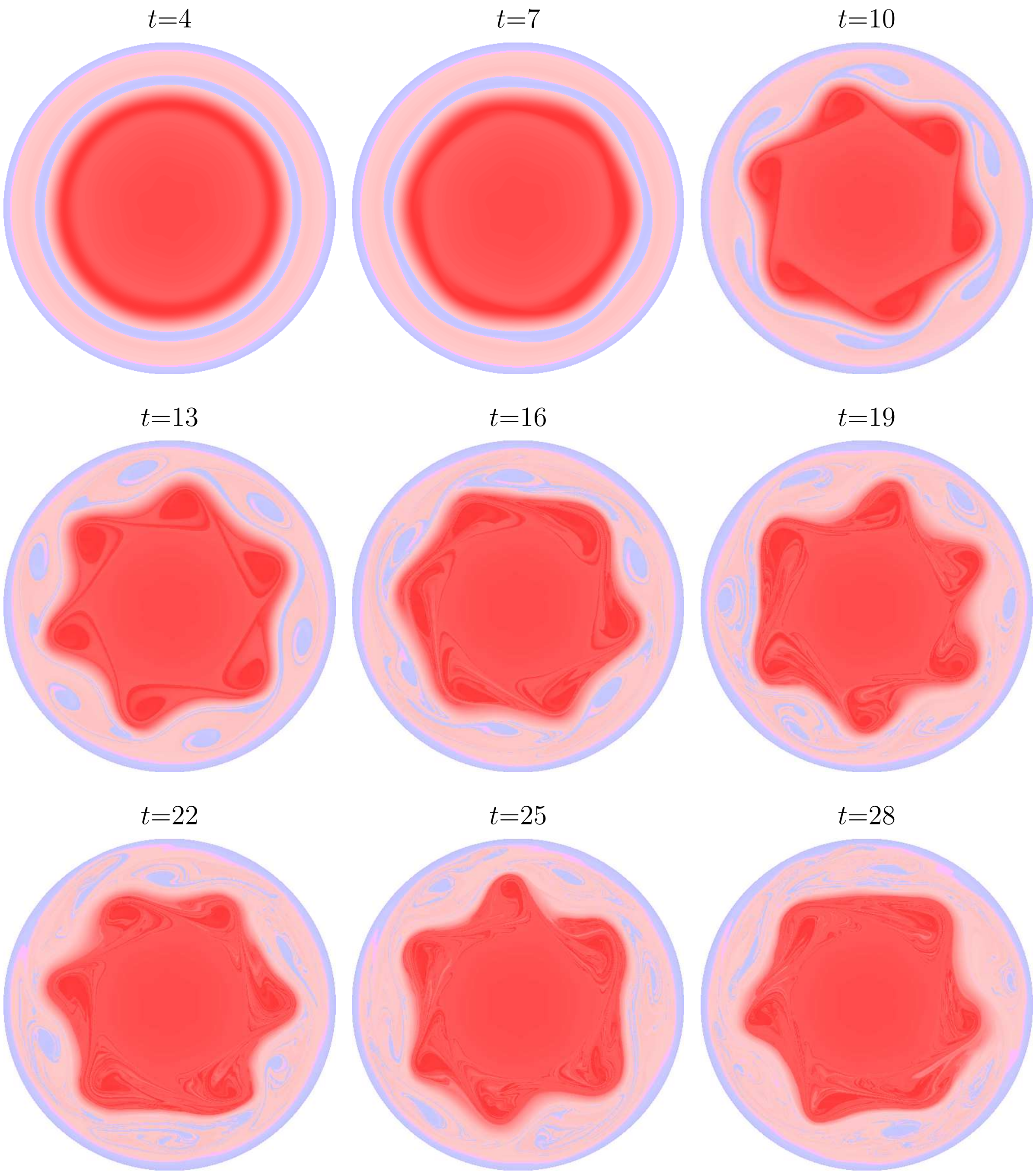

Figure 4.12: The evolution of the PV field, at time t=(4,7,10,13,16,19,22,25,28) $days$, with initial u=60 ms^{-1} and ϕ=π/4 viewed from above the north pole.

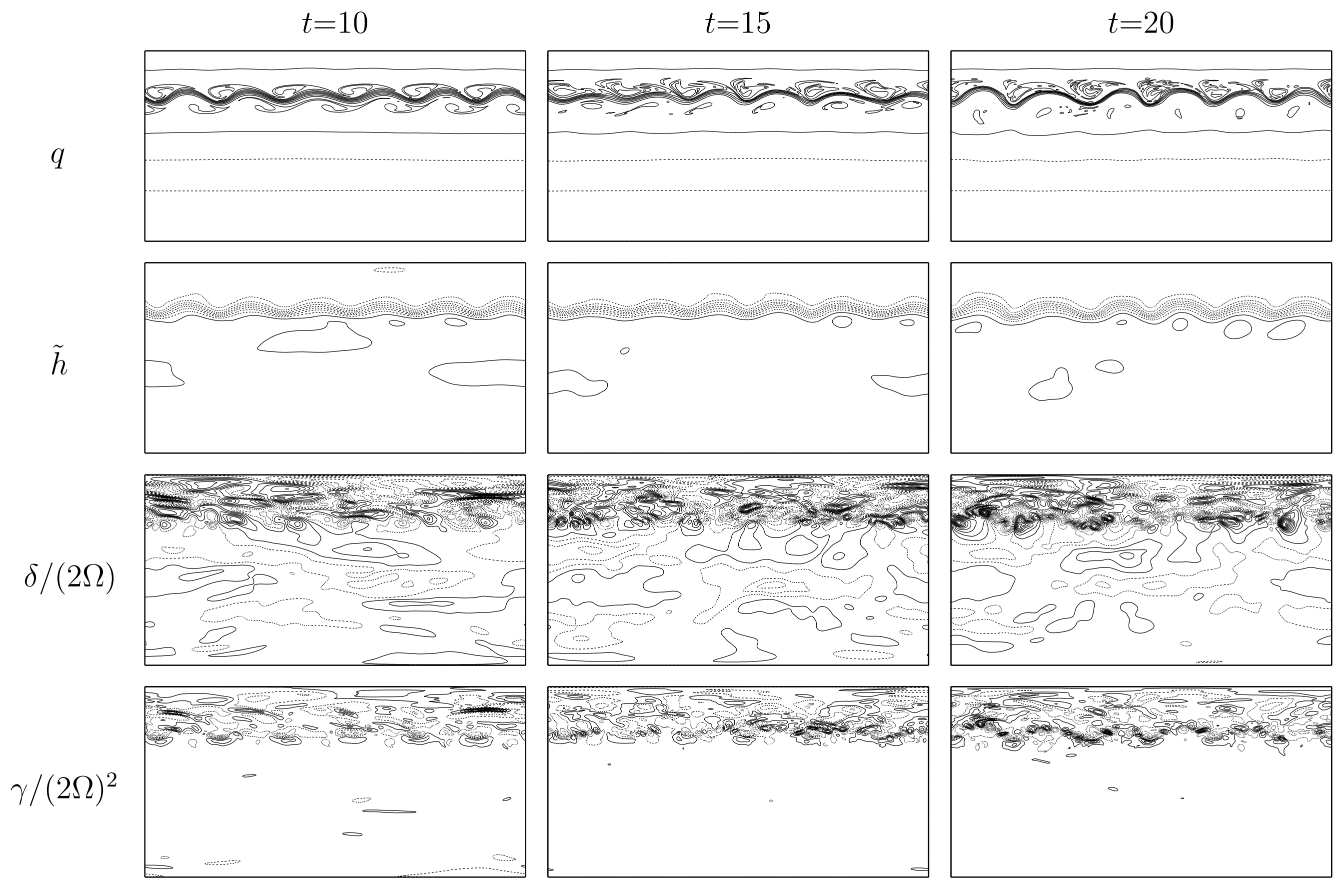

Figure 4.13: From top to bottom row, evolution of q, $\tilde{h}$, $\delta/(2\Omega)$ & $\gamma/(2\Omega)^2$, at times t=10, 15, 20 days, for u=60ms^{-1}, ϕ=$\pi/4$ at mid-latitude. The contour intervals for each is 5.0 for q, 0.1 for $\tilde{h}$, 0.02 for $\delta/(2\Omega)$ and 0.1 for $\gamma/(2\Omega)^2$.

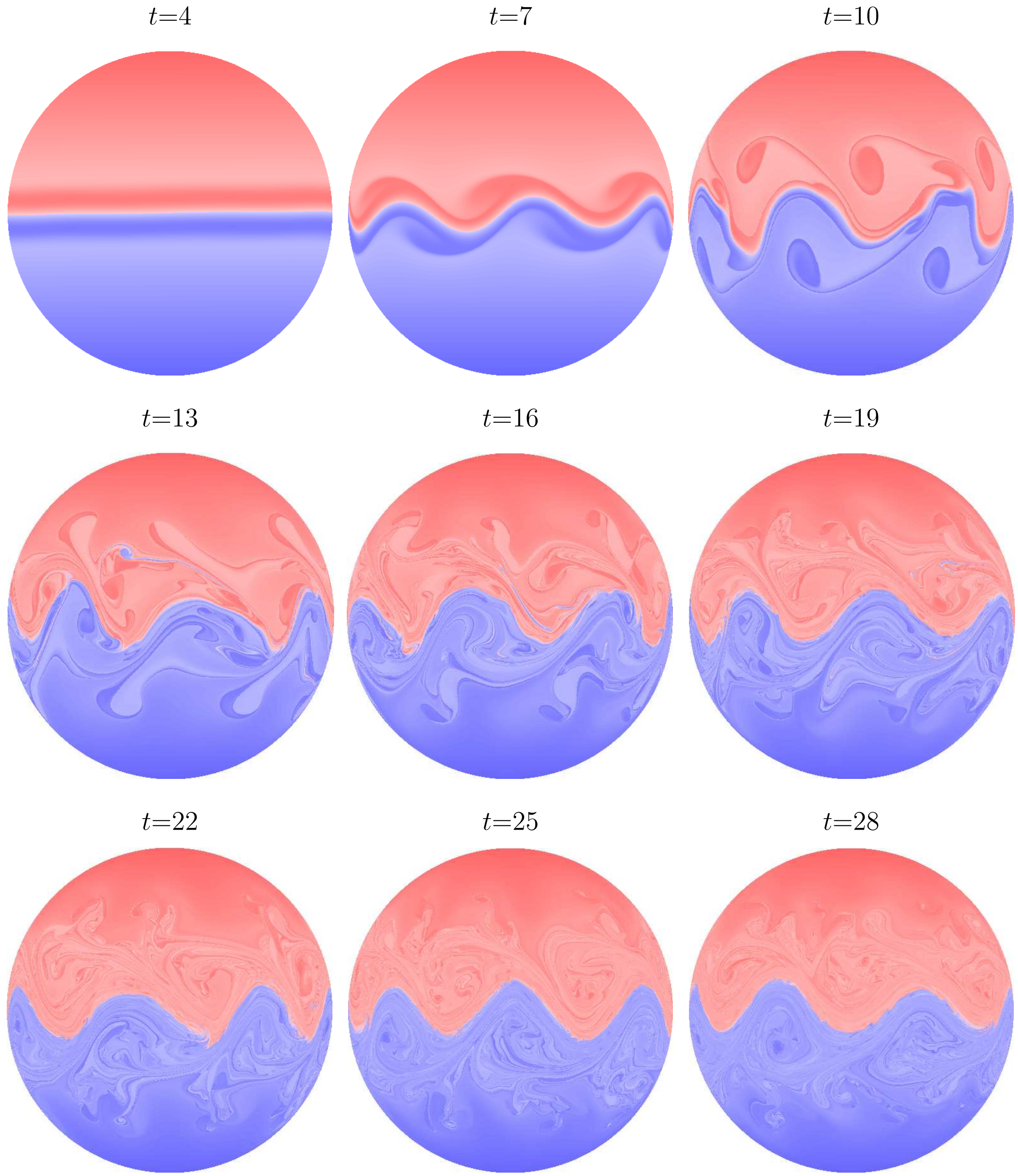

Figure 4.14: The evolution of the PV field, at time t=(4,7,10,13,16,19,22,25,28) $days$, with initial u=80ms^{-1}, ϕ=0 viewed in the plane of the equator.

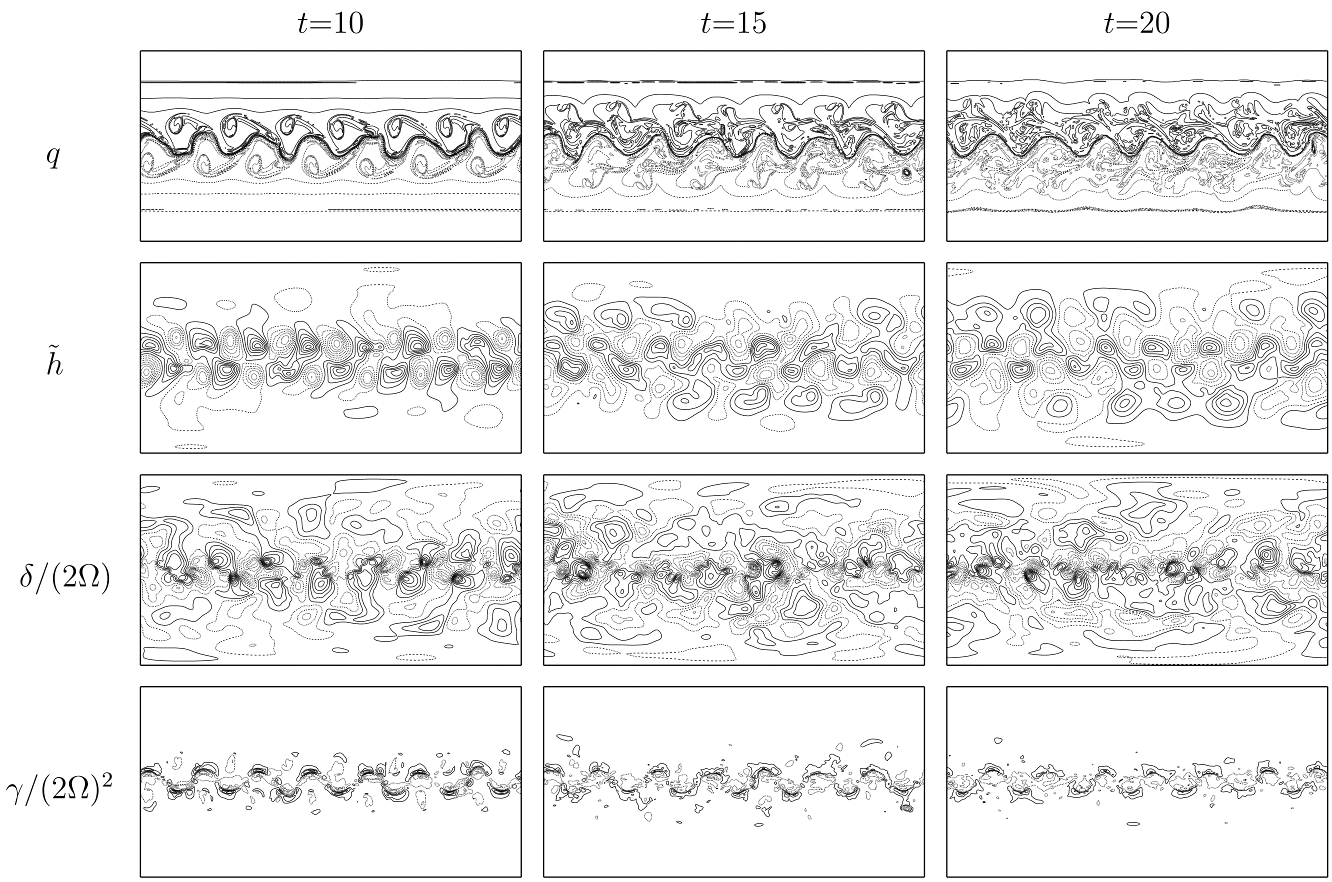

Figure 4.15: From top to bottom row, evolution of q, $\tilde{h}$, $\delta/(2\Omega)$ & $\gamma/(2\Omega)^2$, at times t=10, 15, 20 *days*, for CA_1 for u=80ms^{-1} at the equator. The contour intervals for each is 2.0 for q, 0.02 for $\tilde{h}$, 0.01 for $\delta/(2\Omega)$ and 0.1 for $\gamma/(2\Omega)^2$.

increase Δt in the algorithm.

There are limits to the choice of time-step. In practice, stability is assured if the Courant number $C \equiv U\Delta t/\Delta \leq 1$, where Δ is the horizontal grid spacing and U is the typical horizontal velocity.

The time-step chosen for our reference simulations was $\Delta t = 0.005$ giving C=0.54. We then increased Δt by doubling the reference value successively. Table 4.2 shows time-steps that we will run simulations at along with the corresponding Robert-Asselin filter A, Robert (1966), Asselin (1972), and Courant numbers.

Δt	A	C
0.005	0.04	0.54
0.010	0.05	1.08
0.020	0.11	2.17
0.040	0.20	4.34

Table 4.2: The Courant number C and Robert-Asselin filter A for each successive increase in the time-step Δt.

We expect the algorithm to run stably with Δt that gives $C \geq 1$ due to the semi-implicit nature of the scheme but we would expect to reach a value of Δt where the solution loses accuracy or becomes computationally unstable.

We proceed by running simulations at values of Δt exceeding Courant number one and then taking the rel$\| L \|_2$ norm of the depth and vorticity fields to assess how close to the reference solution these fields remain. The rel$\| L \|_2$ norm is given by

$$\mathrm{rel}\| \mathrm{L} \|_2 = \left[\frac{\sum (\Upsilon_{\mathrm{ref}} - \Upsilon)^2}{\sum (\Upsilon_{\mathrm{ref}})^2} \right]^{1/2}, \tag{4.22}$$

for any field Υ.

Figures 4.16 and 4.17 show the evolution of rel$\| L \|_2$ norms of the depth and vorticity fields respectively for each jet.

Accuracy is preserved in the simulations with increasing time-step for the mid-latitude jet. The rel$\| L \|_2$ norm differences in the vorticity and depth fields are remarkably small. Time averaged difference in vorticity for Δt =0.005, 0.01, 0.02 are respectively, 0.023, 0.016 and 0.019 while there is even less change in the depth field with changes of 7.7×10^{-4}, 5.2×10^{-4} and 5.4×10^{-4}. Thus, the algorithm has become more efficient with almost no loss of accuracy.

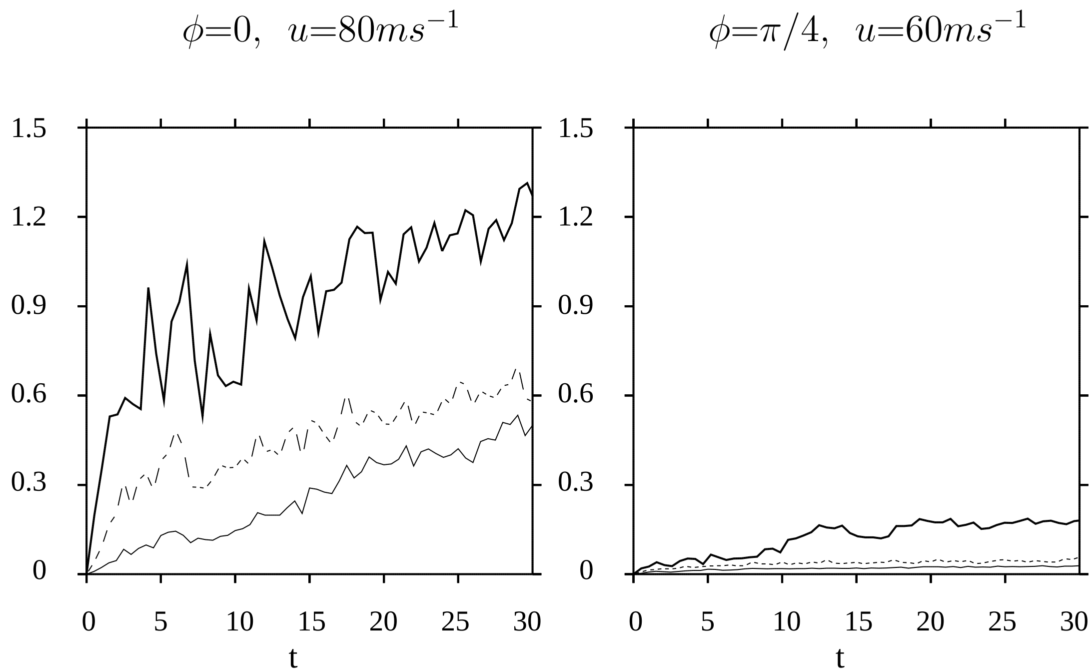

Figure 4.16: The evolution of the $\| L \|_2$ norms of error of the depth field at Δt =(0.01 (thin), 0.02 (dashed), 0.04 (bold)), from a reference Δt=0.005, for *left*: 80ms^{-1}, ϕ=0, and *right*: 60ms^{-1}, ϕ=$\pi/4$.

Increasing Δt has differing results on the rel$\| L \|_2$ of the depth field. For the mid-latitude jet there is a small error up to Δt=0.02. The error norms in the depth for the equatorial jet are significant. We speculate that these errors are being introduced in the solution of the inversion relation (2.48) for $\tilde{h}$ as $f \to 0$.

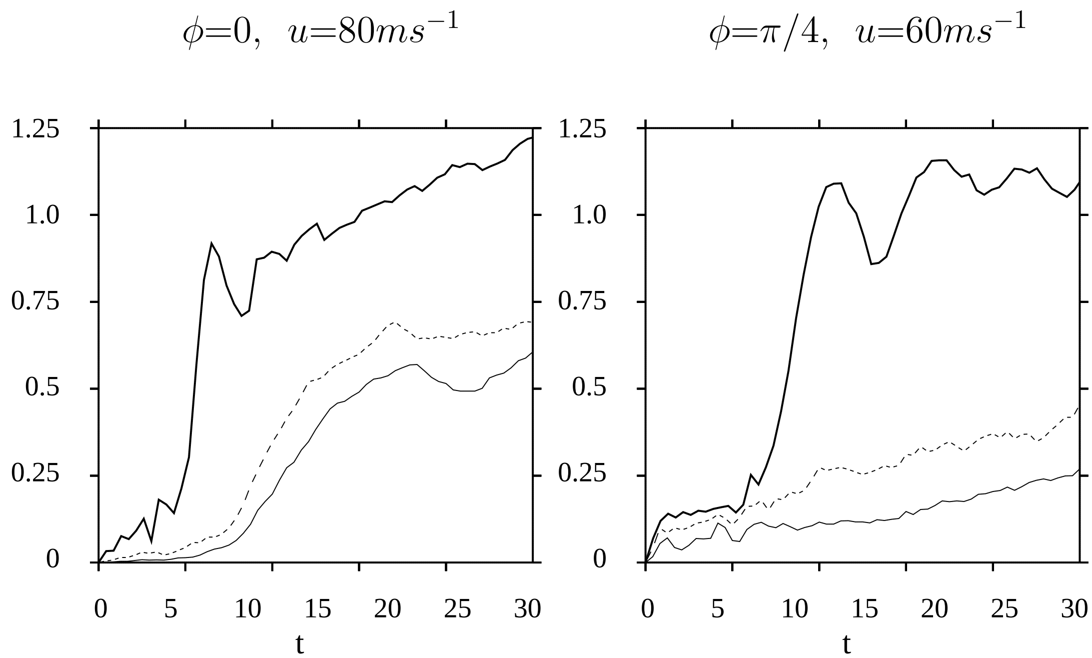

Figure 4.17: The evolution of the rel$\| \ L \ \|_2$ norms of error of the vorticity field at Δt=(0.01 (thin), 0.02 (dashed), 0.04 (bold)), from a reference Δt=0.005, for *left*: 80ms^{-1}, ϕ=0, and *right*: 60ms^{-1}, ϕ=$\pi/4$.

A similar analysis is made of the vorticity field where values of Δt =0.04 give significant errors. It suggests that there would be no merit in considering running CASL at this Δt=0.04 in any context, in its current configuration.

Modification and relaxation of convergence criteria for inversion of the modified Helmholtz equation

A computationally expensive section of the algorithm is solving an elliptic inversion relation for the depth field $\tilde{h}$. At worst, CA$_{\delta,\gamma}$ requires 100+ iterations per Δt to converge with a tolerance criteria 10^{-8}. The standard inversion relation solved iteratively for $\tilde{h}$ is

$$\left[\nabla^2 - \frac{f^2}{c^2}\right]\tilde{h}^{n+1} = \frac{1}{c^2}\left[f(\zeta - f\tilde{h}^n) - \beta u - \gamma\right]. \tag{4.23}$$

This inversion relation was modified to

$$\left[\nabla^2 - \frac{f\overline{Q}}{c^2}\right]\tilde{h}^{n+1} = \frac{1}{c^2}\left[f(\zeta - \overline{Q}\tilde{h}^n) - \beta u - \gamma\right], \tag{4.24}$$

where $\overline{Q}$ is a latitudinally averaged value of q calculated at initial time and q is the PV anomaly. The motivation for this modification is to remove the $f^2 \to 0$ in (4.23). From the definition of the shallow water PV, (2.38), $f \approx q$ at $Ro \ll 1$ as $\zeta/f \ll 1$. Even though this modification was expected to benefit rotation dominated flows it also had a positive impact on regimes away from $Ro \ll \mathcal{O}(1)$.

This change brought about a significant reduction in the number of iterations required for convergence of the inversion relation for the mid-latitude jet at $\Delta t \leq 0.02$.

	u=60, ϕ=$\pi/4$			u=80, ϕ=0		
Δt	ref	$\bar{Q}$	$\pm$%	ref	$\bar{Q}$	$\pm$%
0.005	96.7	59.0	−39%	92.7	62.6	−32.4
0.01	104.3	71.8	−31.2%	93.0	97.2	+4.5
0.02	106.2	76.4	−28.1%	96.4	99.7	+3.4
0.04	116.5	118.3	+1.5%	96.9	100.9	+4.1

Table 4.3: Comparison of the mean of the number of iterations required at each Δt to solve equation (4.23), denoted by the ref column and equation (4.24) which differ by the inversion relation solved, and the percentage increase or decrease. Simulations were 30 days in length.

Table 4.3 demonstrates the efficiency gained from the reduction in the number of iterations required to solve the inversion relation for $\tilde{h}$ from the reference case (4.23) and the modified case (4.24) for the mid-latitude jet up to Δt=0.02. Simulations with the equatorial jet do not benefit at all from the change of equation and are in fact marginally more expensive.

We can go one step further by reducing the tolerance criteria for the convergence of the inversion relation (4.24). As a test we examine the vorticity and depth fields for simulations with Δt=0.02 for the mid-latitude jet at $60ms^{-1}$.

tol	ref iter.	mean iter.	±%
10^{-8}	106.2	76.38	-28.1
10^{-7}	106.2	44.75	-57.9
10^{-5}	106.2	13.6	-87.2
10^{-3}	106.2	3.0	-97.2

Table 4.4: The mean number of iterations while the tolerance on equation (4.24) is reduced, for Δt=0.02.

The reduction in the number of iterations required as the tolerance is reduced from table 4.4 is significant. Figure 4.18 shows the rel$\| L \|_2$ error norms of the depth and vorticity fields respectively. The error norm in the depth field for Δt=0.02 with values of *tol* up to 10^{-3} is minimal, while in the vorticity field, *tol*=10^{-5} still preserves accuracy up to t=15, before the simulations diverge. If the model was to be run with *tol*=10^{-5} and Δt=0.02 we could still expect a reduction in the number of iterations required to solve the modified Helmholtz relation of around 87% for regimes where the dynamics is primarily in the mid-latitudes.

This analysis has been by no means exhaustive, but is aimed as an illustration of the potential that exists in improving the efficiency of the CASL algorithm while maintaining an accurate solution.

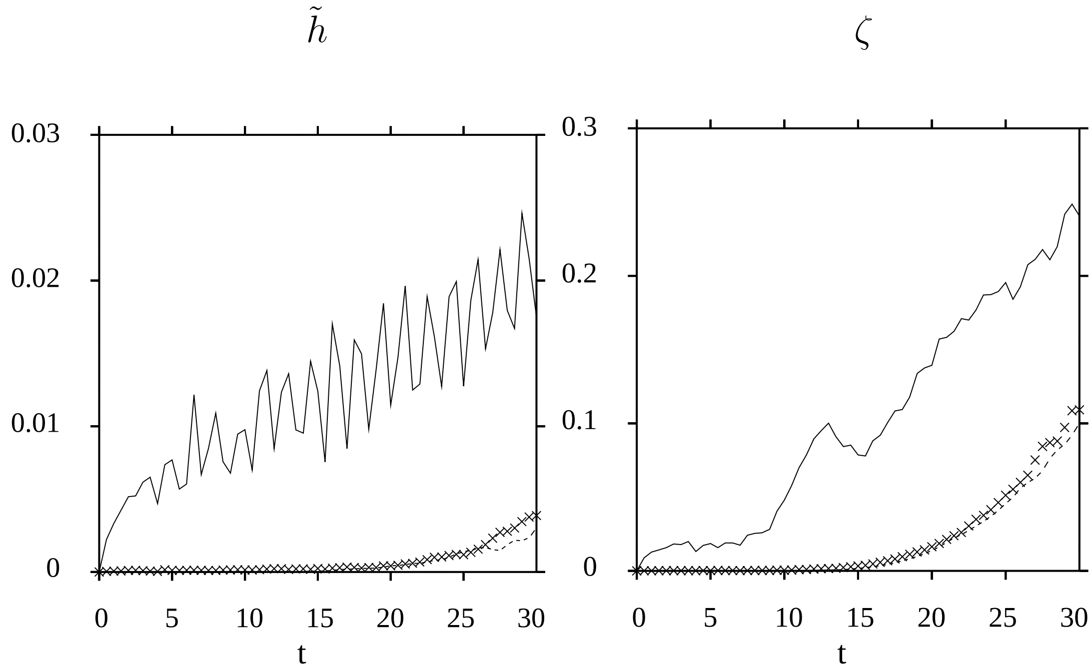

Figure 4.18: The evolution of the rel$\| L \|_2$ norms of error of *left*: depth, and *right*: vorticity for tol=(10^{-7} (dashed), 10^{-5} (cross), 10^{-3} thin)) with Δt=0.02 with reference solution tol=10^{-8} and Δt=0.005. Note the different scales on each graph.

4.3 Conclusion

In this chapter we investigated de-centring the three-time-level semi-implicit, semi-Lagrangian time integration scheme of two distinct shallow water CASL algorithms. For both shallow water algorithms, de-centring acts to minimise IGW motion, spurious or otherwise, as it acts on the gravity wave component of the flow. There is minimal effect on the large-scale vortical motion of the flow. While it is not clear that de-centring the integration scheme is entirely benign we have demonstrated that with the appropriate choice of imbalance variables, γ and δ, as opposed to δ and $\tilde{h}$ coupled with PV, in the shallow water CASL algorithm, acts to minimise the Bolin-Charney 'imbalance' in complex, turbulent flows, for each value of the de-centring parameter. This is an important step if there were to be further study into the use of shallow water CASL algorithm, $\mathrm{CA}_{\delta,\gamma}$ in an operational NWP context. Therefore the algorithm which is more amenable to de-centring is $\mathrm{CA}_{\delta,\gamma}$ and so we concentrated on this algorithm for the remainder of the chapter.

We then demonstrated that $\mathrm{CA}_{\delta,\gamma}$ can model flows with Ro, $Fr \sim \mathcal{O}(1)$, a regime containing many meteorological features of interest, which is one of the main concerns of NWP specialists, who may use the algorithm operationally.

We have also demonstrated that the time integration scheme of $\mathrm{CA}_{\delta,\gamma}$ can simulate complex geophysical flows for Courant number $C > 1$, allowing the algorithm to employ increased Δt, generating a forecast solution in less computational time while preserving the accuracy of the flow.

We have also shown that $\mathrm{CA}_{\delta,\gamma}$ has ample scope for increased efficiency. We demonstrated that increasing Δt, so that $C > 1$ did not overly affect the accuracy of the solution for the mid-latitudinal jet. The modification and relaxation of the of the inversion relation for the height field, coupled with increased Δt significantly reduces the number of iterations required for convergence, one of the more expensive components of the algorithm, while preserving accuracy for the predominantly mid-latitudinal flows, for tol=10^{-5} and Δt=0.02.

Following the investigation of CASL, a balanced model in shallow water, barotropic flows we proceed with an investigation of CASL in a non-hydrostatic, baroclinic flow in chapter §5.

Chapter 5

Comparison of numerical methods under the non-hydrostatic Boussinesq approximation

5.1 Introduction

In this chapter we compare three numerical algorithms simulating three-dimensional freely decaying turbulence. One of the algorithms is the non-hydrostatic CASL formulation. Two pseudospectral algorithms, vorticity-based pseudospectral (VPS) and primitive equation pseudospectral (PEPS) are constructed to draw comparison with CASL. This comparison is made as many major forecast centres around the globe employ spectral-based methods in their forecast models.

We examine geophysical flows that exhibit the typical properties of a large-scale geophysical flow, a near balanced initial condition. Firstly we quantify the stability requirements of each algorithm. Then we vary the initial Rossby number of the flow and assess how each algorithm simulates the flow. We also outline operational limitations of CASL in this context before quantifying to what degree each algorithm preserves balance.

Finally we try to quantify which of the three algorithms is the most efficient and therefore most suited to an operational NWP environment.

5.1.1 Initialisation and parameter settings

The initial conditions for each simulation consist of a two-dimensional vorticity field perturbed in the vertical direction. We start by specifying the two-dimensional kinetic energy spectrum $E(k)$ of a random vertical vorticity field that is in exact geostrophic and hydrostatic balance following Dritschel *et al.* (2007). Here we take $E(k)=k^3 \exp[-(k/2)^2]$ which peaks at $k=\sqrt{6} \approx 2.45$ where $k=\sqrt{k_x^2+k_y^2}$, k_x and k_y being the horizontal wavenumbers. Next, the three-dimensional PV is created by displacing the two-dimensional vorticity field in x by: $0.016 \cos z - 0.007 \cos(2z + 63°)$ and in y by: $0.010 \sin z + 0.013 \sin(2z + 63°)$. This choice here is completely arbitrary. As a result the initial conditions are no longer in exact geostrophic and hydrostatic balance but remain close to balance, approximating the large scale behaviour of geophysical flows. Figure 5.1 shows the initial three-dimensional PV for a flow with Ro=0.1 initially, and a horizontal cross-section of the PV at z=0. The initial conditions for each simulation are equivalent at time t=0.

The simulation domain is triply periodic with physical dimension $L_x \times L_y \times L_z$, with $L_z = 2\pi$ and L_x=L_y=$(N/f)L_z$ with an equal number of grid points (here 128 unless otherwise stated, for a CASL simulation, the contour-to-grid conversion grid is therefore 512^3) used in each direction. We take a buoyancy frequency of $N = 2\pi$ and set Prandtl's ratio $\epsilon \equiv f/N$ =0.1 so that the inertial period T_{ip} is $2\pi/f$ =10. McKiver & Dritschel (2009) demonstrated that the flow

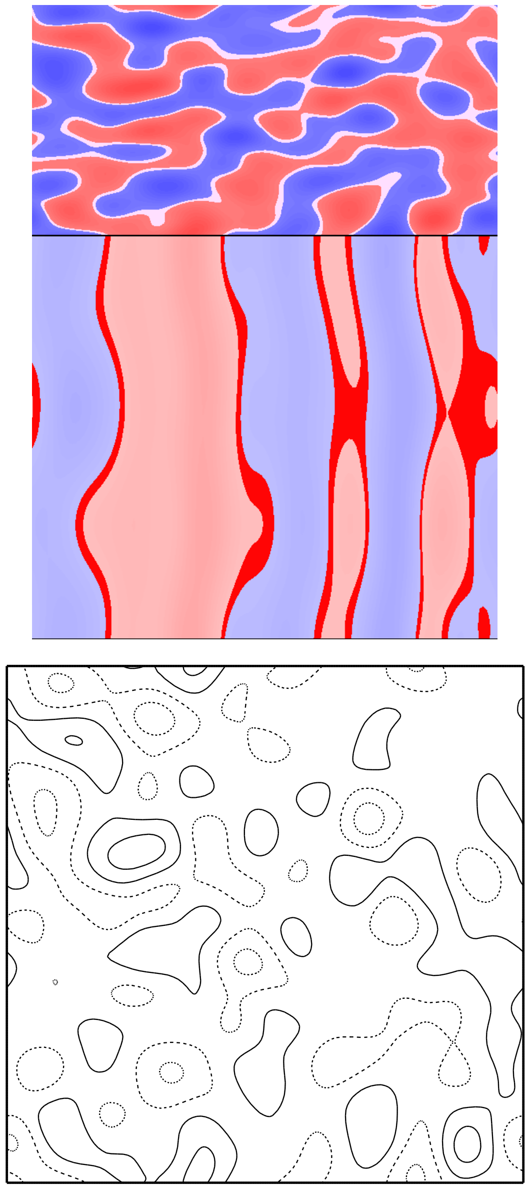

Figure 5.1: Top: Initial three-dimensional PV distribution for a simulation with Ro=0.1, viewed at an angle of 60° from the vertical. Positive PV is represented by red while negative PV is blue. Bottom: Horizontal cross-section of the PV at z=0. Here the contour interval Δ=0.05 and the plotted contours represent $\pm$0.025 and $\pm$0.075. Positive contours are represented by solid lines and negative contours by dashed lines.

evolution has no significant dependence on f/N for $f/N \lesssim 0.1$.

The time integration scheme used to advect the Lagrangian PV in CASL is an explicit third-order Adams-Bashforth scheme. In CASL, VPS and PEPS, the gridded prognostic variables are evolved in time by a standard explicit leapfrog scheme. The time-step Δt was chosen as a function of the initial value of Ro. For $Ro \leq 0.5$, we use Δt=0.1, which is small enough to resolve IGWs, which have frequencies between f and N. For values of $Ro > 0.5$, we use Δt=$0.005 T_{buoy}/(Ro\,\epsilon)$ which is a non-dimensional fraction of the maximum relative vorticity to maintain equivalent temporal accuracy. Therefore, as Ro increases above 0.5, Δt decreases to maintain the accuracy of the solution. This ensures that the IGWs, having frequencies between f and N are well resolved in time.

Geophysical flows typically exhibit very high Reynolds numbers, in the ocean typically of the order 10^{11} (see Vallis (2006)), and as such molecular viscosity cannot be modelled explicitly. However some diffusion is required for numerical stability. Here we use an artificial numerical diffusion term. CASL uses a bi-harmonic hyperdiffusion term $\nu\nabla^4$ which is enough to remove the smallest ageostrophic vorticity features in CASL. In PEPS and VPS we use a Laplacian diffusion term $\nu\nabla^2$ to emulate standard operational weather prediction models. In each case ν is chosen to damp the largest wave-number in spectral space at a chosen maximum rate C. This implies

$$\nu = \frac{C}{\frac{2\pi}{f}[(n_x^d + n_y^d + n_z^d)]}, \tag{5.1}$$

where d is the order of diffusion operator (d=2,4) and C is the damping rate on the highest wave-numbers k_x=$n_x L_z/2L_x$, k_y=$n_y L_z/2L_y$ and k_z=$n_z/2$, on a grid of resolution $n_x \times n_y \times n_z$. In the next section we investigate the smallest values of C required for the stability of each method and the impact this has on the accuracy of the flow.

5.1.2 Numerical stability

McKiver and Dritschel (2008), performed a number of turbulence simulations initialised from a near balanced random distribution of three-dimensional PV. They found that, for CASL, a value of C=1+10Ro^4 per inertial time period was sufficient for stability as Ro was varied initially. We performed a similar investigation for our different initial condition to obtain C for the stability of the pseudospectral algorithms PEPS and VPS.

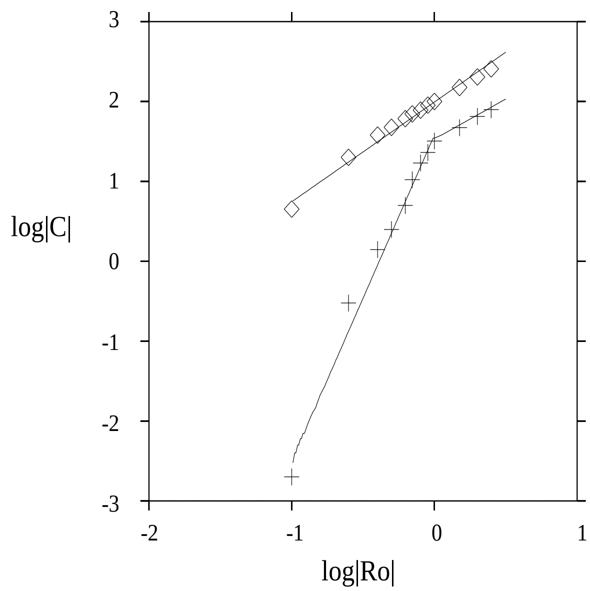

Figure 5.2: A log-log (base 10) plot of minimum diffusion coefficient C vs. Ro, with best fit straight lines through the data points. PEPS 128^3: ◇ ◇ ◇ , VPS 128^3 + + + .

Figure 5.2 shows the dependence of C on Ro up to Ro=2.5 for PEPS and VPS. PEPS exhibits an approximate linear dependence on Ro with best-fit gradient of 1.20 while VPS exhibits the same Ro^4 dependence found in CASL up to Ro=1.0 with best-fit gradient of 4.08. For Ro >1.0 the dependence of C is linear in Ro with best-fit gradient of 1.02. At 128^3 the numerical stability criteria required for PEPS is $C = 1 + 110Ro$. For VPS, C=1+45Ro^4 up to Ro=1.0 and C =1+33Ro

for Ro >1.0.

Figure 5.2 demonstrates that significantly less numerical diffusion is required for the stability of VPS compared to PEPS, especially at $Ro \ll 1.0$. We do not include the results for CASL as CASL requires significantly less numerical diffusion than both pseudospectral counterparts. However, the CASL method uses a bi-harmonic diffusion operator which is more efficient at dissipating high wavenumber spectral coefficients and CASL damps only the horizontal components of $\mathcal{A}$, not the PV. As the numerical diffusion required for stability decreases we expect to capture sharper gradients and smaller scale structures within the flow. It is no coincidence that the algorithms with transformed prognostic variables, CASL and VPS, require less diffusion as this transformation favours the modelling of the balanced and unbalanced components of the flow. Thus the change of variables gives a numerical advantage due to the more accurate representation of the underlying balanced dynamics of the flow.

5.2 Results

5.2.1 Flow evolution comparison

It is instructive to compare simulations at different resolutions, namely of PEPS at 256^3, (PEPS:256), VPS at 128^3, (VPS:128) with CASL at 64^3, (CASL:64). Each simulation had a duration of 20 inertial periods. We examined initial maximum values of Ro =0.1, 0.5, 1.0 and 1.5. The CASL simulations at Ro=1.5 diverge as CASL is not designed for high Ro flows, as discussed in Dritschel & Viùdez (2003). One feature of relatively high Ro flows are static instabilities which are an indicator of overturning or mixing of the fluid in the vertical direction. This is a feature which CASL cannot model adequately. Indeed, there is a limit to the maximum value of Ro initially in CASL and this point is covered in more depth in section §5.2.2.

The degree to which rotation and stratification influence each flow is shown in figures 5.3 and 5.4 by the time evolution of the domain minimum (most negative) and maximum (most positive) Rossby numbers Ro_{min} and Ro_{max}, and the domain maximum Froude number Fr_{max} for initial Ro=0.1, 0.5, 1.0 and 1.5, for each algorithm.

In figure 5.3 at Ro=0.1 there is essentially no difference between each algorithm with Ro_{max}, Ro_{min}=±0.1. At higher values of Ro, PEPS requires more diffusion than VPS, which in turn requires more diffusion than CASL. This suggests that as we investigate higher values of Ro in PEPS and to a lesser extent in VPS, the underlying dynamics of the flow will be more heavily damped, resulting in a less accurate (more diffusive) solution.

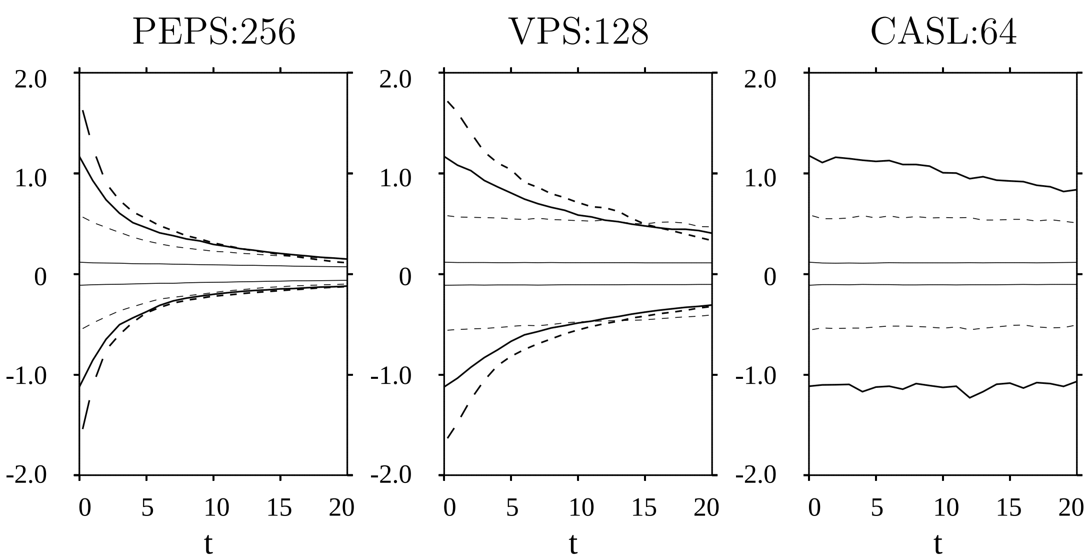

Figure 5.3: Time evolution of the domain minimum and maximum Rossby numbers for initial Ro=0.1 (thin lines), 0.5 (dashed lines), 1.0 (bold lines) & 1.5 (bold dashed lines) for each algorithm indicated. The CASL algorithm has resolution 64^3. Note that the CASL algorithm diverges for Ro=1.5.

In figure 5.4, when each algorithm has initial Ro=0.1 the flow evolves close to the quasi-geostrophic regime. As the initial Ro increases in PEPS, $Fr_{max} \approx 0.1$, which indicates that the flow is strongly stratified in the vertical direction. At values of initial $Ro > 0.1$, VPS and CASL do not tend to model a flow with such strong stratification as PEPS. In CASL, particularly at initial maximum Ro=1.0, the maximum Froude number remains around 0.6, which suggests that CASL is able to sustain weak stratification and a more physically realistic three-dimensional flow, unlike the pseudospectral algorithms, at lower resolution.

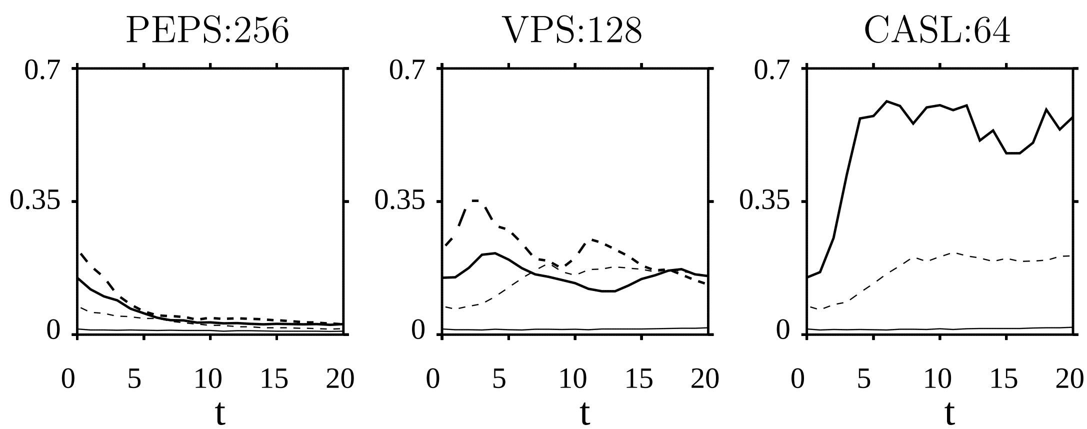

Figure 5.4: Time evolution of the domain maximum Froude number, for initial Ro=0.1 (thin line), 0.5 (dashed line), 1.0 (bold lines) & 1.5 (bold dashed line). Note that the CASL algorithm diverges Ro =1.5.

Figure 5.5 shows the time evolution of the root mean square (rms) vertical velocity divided by the rms horizontal velocity ($w_{rms}/|\boldsymbol{u}_h|_{rms}$), at the resolutions indicated. In oceanic flows, the vertical velocity w is observed to be much weaker than the horizontal velocity. The magnitude of w is a common (but potentially misleading) measure of imbalanced (IGW) motion, see Viúdez & Dritschel (2003). In the limit of small Rossby and Froude number one expects $|\boldsymbol{u}_h|$ to be larger than w as $|\boldsymbol{u}_h|$ scales like Ro, while w scales like Ro^2 for small Ro, see equations (A.1) & (A.3) in appendix A. Again, at differing resolutions the pseudospectral methods perform similarly, with ($w_{rms}/|\boldsymbol{u}_h|_{rms}$) displaying almost no dependence on

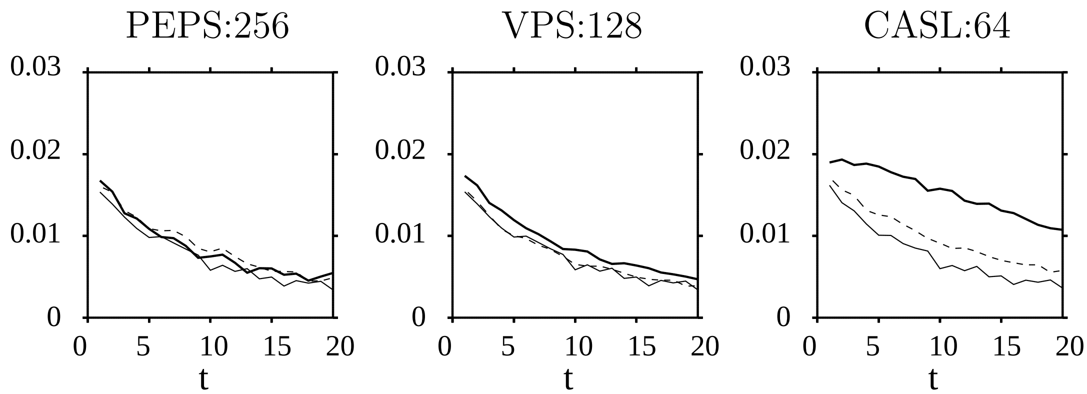

Figure 5.5: Time evolution of rms vertical velocity divided by the rms horizontal velocity ($w_{rms}/\boldsymbol{u}_{hrms}$), for initial Ro=0.1 (thin line), 0.5 (dashed line), 1.0 (bold lines) & 1.5 (bold dashed line).

Ro. In CASL ($w_{rms}/|\boldsymbol{u}_h|_{rms}$) does exhibit a dependence on Ro as expected theoretically. By contrast, much stronger diffusion in the pseudospectral algorithms damps the vertical velocity and obscures the underlying balance.

Figures 5.6 and 5.7 show vertical and horizontal cross sections of the PV at y=0 and z=0 respectively, at staggered times t=5, 10 and 15 inertial periods, at the values of Ro indicated. The times were chosen at each Ro to allow a more meaningful comparison. These results were typical of other cross sections of the PV. It is instructive to qualitatively assess how each algorithm diagnoses the PV, which is a key field linked to the large-scale balanced dynamics of the atmosphere. At Ro=0.1 there is no significant difference in the overall structure and accuracy of the PV between each algorithm, vertically or horizontally. At Ro=0.5 and 1.0 the structure of the PV captured by PEPS:256 and VPS:128 are broadly similar but VPS:128 captures sharper PV gradients. CASL:64 also captures these sharper PV gradients along with more small scale structures in the PV field. Such sharp PV gradients are commonly observed in the atmospheric jet stream, Hoskins *et al.* (1985). Specifically, the vertical cross section of the PV from figure 5.6, for CASL:64 at Ro=1.0 provides more evidence of the nearly inviscid nature of the dynamics captured. The chaotic nature of geophysical flows contributes to the relative divergence of each solution over time, which is to be expected. Even so, PEPS:256 and VPS:128 are visibly more diffuse due to the explicit diffusion used in each pseudospectral method.

Figure 5.8 shows horizontal cross sections of the vertical velocity field at z=0, at Ro and t shown. These results were typical of other cross sections of the vertical velocity field. Again, there is no noticeable difference at Ro=0.1 in the detail and structure captured. For larger Ro, PEPS:256 loses the fine scale of resolution compared to VPS:128, while VPS:128 does not capture as much of the fine details as CASL:64. The plot at Ro=1.0, t=15 for CASL:64 exhibits a much greater amount of fine scale structure as all the plots the same contour intervals.

Through less numerical diffusion, VPS:128 captures a greater proportion of the fine-scale structure of the flow. At the same resolution CASL is more computationally expensive than VPS, which in turn is more computationally expensive than PEPS. This is due to the iterative procedure required to invert the vertical component of the potential $\boldsymbol{\varphi}$ in the double Monge-Ampère equation (2.54) to recover the primitive variables of the system. A comparison of the relative computational efficiency of each algorithm is presented in section §5.2.4.

Figure 5.9 shows the energy dissipation rate from each algorithm given by

$$\frac{\partial E}{\partial t} = uu_D + vv_D + ww_D + f^2 \mathcal{D}\mathcal{D}_D, \tag{5.2}$$

where the subscript D indicates the diffusive component. At Ro=0.1, CASL:64 and VPS:128 dissipate energy at similar orders with CASL achieving this at lower resolution. In contrast, PEPS:256 dissipates energy at a higher rate, at this higher resolution.

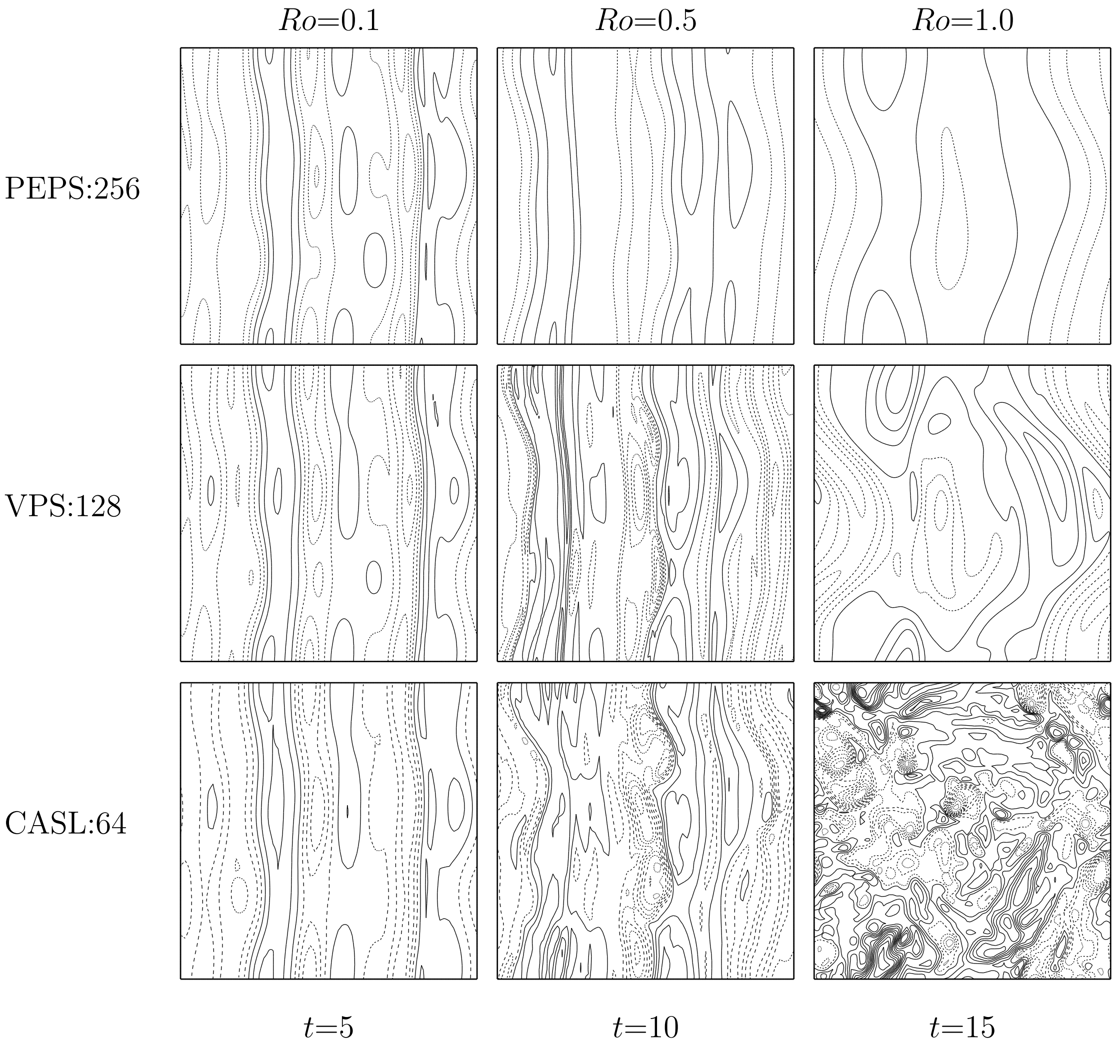

Figure 5.6: Comparison of the PV field in a y=0 vertical cross section for each algorithm and resolution indicated. The contour intervals are Δ=0.02 for Ro=0.1 and Δ=0.08 for Ro=0.5 and 1.0, where the time displayed takes account of the eddy turnover time at each Ro. Plotted contours represent $\pm\Delta/2$, $\pm 3\Delta/2$,...., $\pm(2n+1)\Delta/2$. Positive contours are represented by solid lines and negative contours by dashed lines.

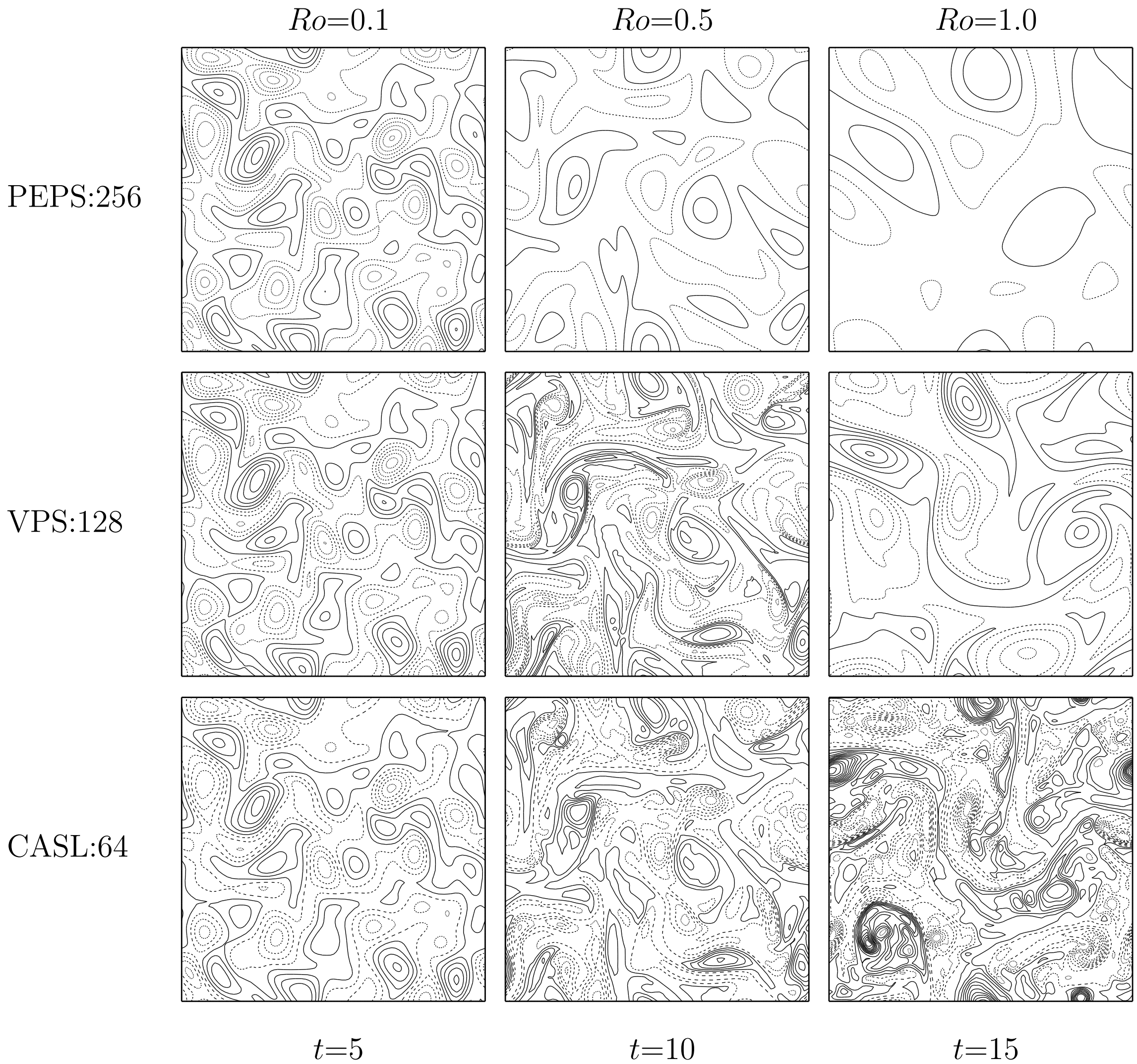

Figure 5.7: As in figure 5.6, for a z=0 horizontal cross section of the PV field.

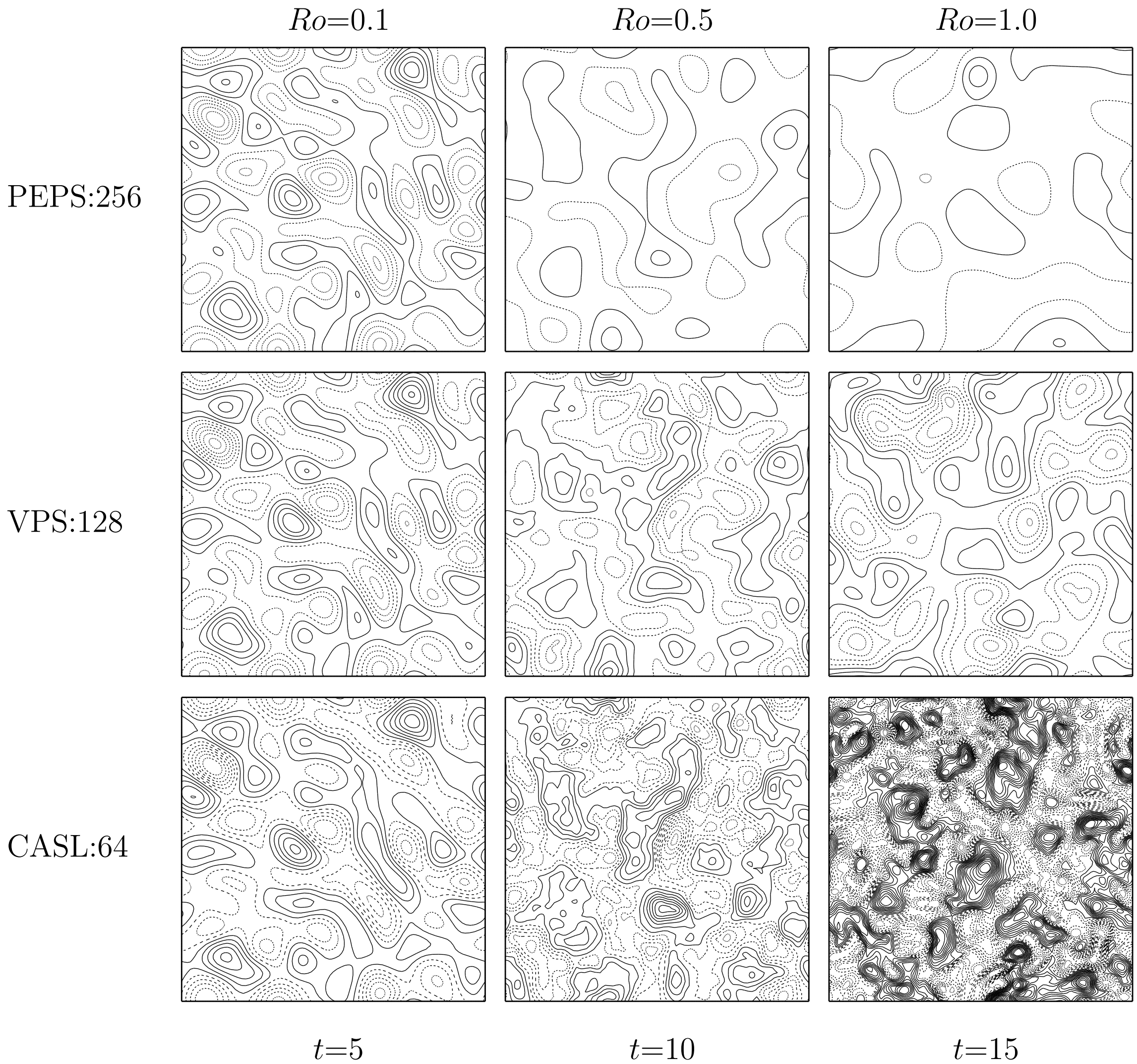

Figure 5.8: As in figure 5.7, for w, the vertical velocity. The contour intervals are Δ=0.0002 for Ro=0.1 and Δ=0.01 for Ro=0.5 and 1.0.

As Ro increases, energy dissipation rates increase for each algorithm. In terms of accuracy CASL appears to match or outperform its pseudospectral counterparts up to Ro=0.5.

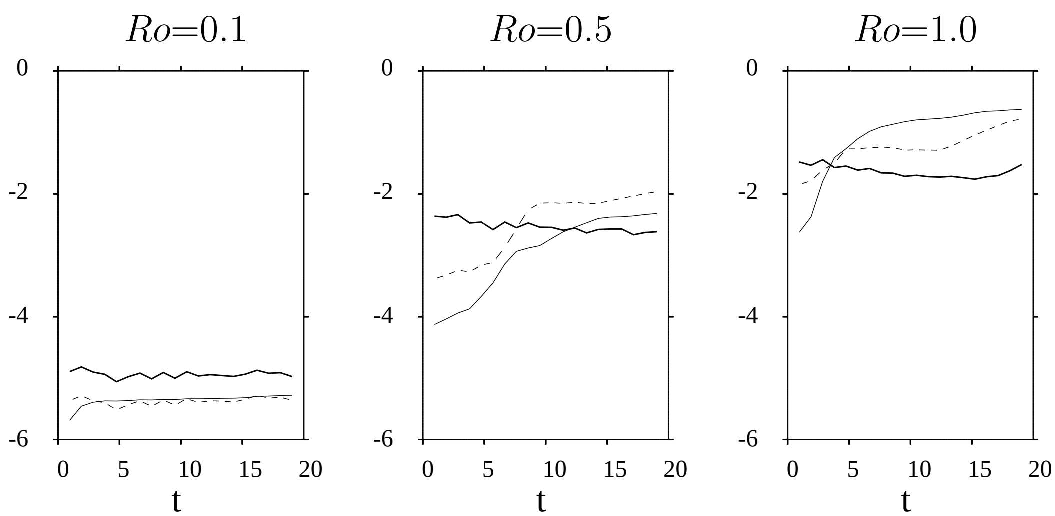

Figure 5.9: Time evolution of the energy dissipation from (5.2), for (bold line) PEPS:256, (dashed line) VPS:128, (thin line), CASL:64. Note that a logarithmic scale (to base 10) is used for the energy dissipation rate.

One limitation of the CASL algorithm is its restriction on the value of Ro it can model. CASL represents the PV field on material surfaces which cannot overturn and must remain smooth. This is to retain the bijective nature and the smoothness of the mapping between material (isopycnal) surfaces and the vertical direction z. This point is illustrated in the next section, §5.2.2.

5.2.2 A limitation of CASL

As outlined previously, there is a limit on the value of Ro within the flow that CASL can simulate. Dritschel & Viúdez (2003) found that CASL diverges in regimes where there are rapid changes in the isopycnal displacement $\mathcal{D}$. Physically in this situation a static instability occurs where fluids of different densities are mixed vertically, such as convective overturning in the atmosphere.

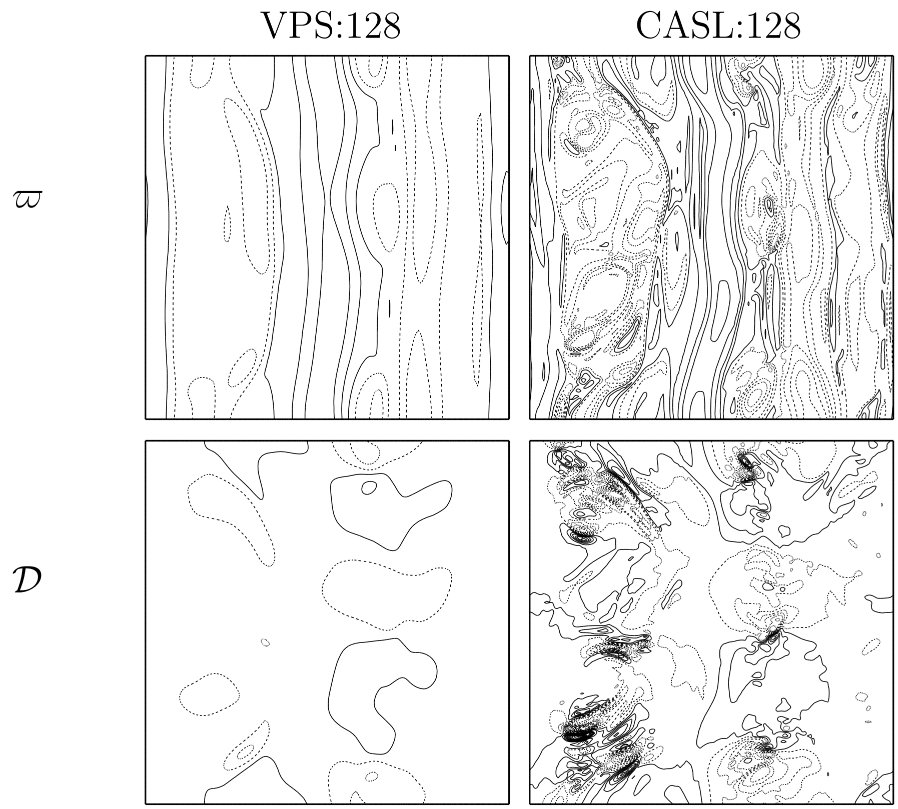

Figure 5.10: Comparison of the vertical cross sections at $y \approx 9\pi/10$ of *top row:* PV, ϖ (contour interval Δ=0.2), *bottom row*: isopycnal displacement, $\mathcal{D}$ (Contour interval Δ=0.05) for *Ro*=1.0 at time t =7.45 inertial periods for VPS and CASL simulations at 128^3.

A comparison is drawn between VPS and CASL at *Ro*=1.0, at grid resolution 128^3. Figure 5.10 shows the PV and the isopycnal displacement $\mathcal{D}$, at $y \approx 9\pi/10$ at time t =7.45 inertial periods for both VPS and CASL simulations two time-steps before the static stability criterion 1 - $\mathcal{D}_z > 0$, Holton (2004), is violated in CASL. This instability occurs in the bottom left corner of $\mathcal{D}$ from CASL. In both diagnostic fields significantly more detail is captured by the CASL algorithm.

As CASL advects the PV on isopycnals, this can only be done sensibly when the isopycnals are stably oriented. This limitation calls into question the suitability of a Lagrangian method such as CASL in a forecasting context. An observational study from chapter 3 suggests that these physical static instabilities do not occur above a certain horizontal length scale Δx of around 20-25km. In other words a global forecast model operating at this scale would not expect to capture a static or inertial instability, which could potentially remove this obstacle to the use of Lagrangian techniques such as CASL, at synoptic scales in the atmosphere, in an operational numerical weather prediction context.

5.2.3 Nonlinear quasigeostrophic (NQG) balance

To assess the balance properties of each algorithm the non-linear quasi-geostrophic (NQG) balance routine McKiver & Dritschel (2008) is used as a diagnostic tool. NQG balance has been used for a similar purpose in McKiver & Dritschel (2009). As the flow is close to balance initially an important question is to what extent each algorithm preserves balance as the flow evolves. The balanced component of each flow can be extracted with the NQG balance routine to allow an estimation of how the degree of imbalance varies with each algorithm, at varying $Ro \leq 0.5$. NQG balance diagnoses balance based on a quasi-geostrophic scaling analysis of the non-hydrostatic equations, (2.50) as outlined in section §2.6. This procedure has been proved to capture a much greater fraction of the underlying balance than the standard linear quasi-geostrophic balance. Full details can be found in McKiver & Dritschel (2008). An outline is given in appendix B. We now investigate the vertical velocity and isopycnal displacement fields to discover to what extent each field is composed of balanced motions.

Vertical velocity

The vertical velocity field w is weak compared to the horizontal velocity components $\mathbf{u}$ and is frequently used as a measure of IGW activity. As the balanced component of the vertical velocity is typically 10^4 times smaller than the horizontal velocities the finer scale IGW motion signal may be expected to appear here initially.

Each simulation was initialised with the NQG balance routine to minimise the initial spurious IGW activity. Figure 5.11 contains the full (w), balanced (w_b) and imbalanced (w_i=$w - w_b$) components of the vertical velocity field at time t =10 inertial periods, at Ro=0.1, for each of the three algorithms. The cross section here is vertical, at y=0. The general behaviour in each of these cross sections is replicated in all other cross sections of w. The main difference in the qualitative representation of w in each algorithm is the contour intervals required to adequately capture each field. The magnitudes of w are of the order of two decades greater in PEPS:256 than in the corresponding CASL:64 and VPS:128 simulations. Furthermore, w in PEPS:256 is almost exclusively composed of imbalanced motions. For CASL:64 and VPS:128 the full and balanced w fields are in broad agreement and are of the same magnitude. The qualitative differences manifest in the w_i fields which are 5 times finer than the corresponding balanced fields, evidence that the CASL:64 simulation has remained close to balance for the evolution of the flow until this point, t=10 inertial periods. The structures in CASL:64 are of a much smaller scale than in the corresponding VPS:128 field. This smaller-scale behaviour is likely to be the signal of the smaller scale IGWs. In figure 5.12 the same comparison is drawn as in figure 5.11, but for Ro=0.5. Again, PEPS:256 fails to capture any significant portion of the balanced dynamics of w and is an order of magnitude greater than the value of w in CASL:64 and VPS:128. Significantly, where there was no major difference between CASL:64 and VPS:128 at Ro=0.1 there are now differences at Ro=0.5. CASL:64 captures a much finer scale of detail in w, at lower resolution.

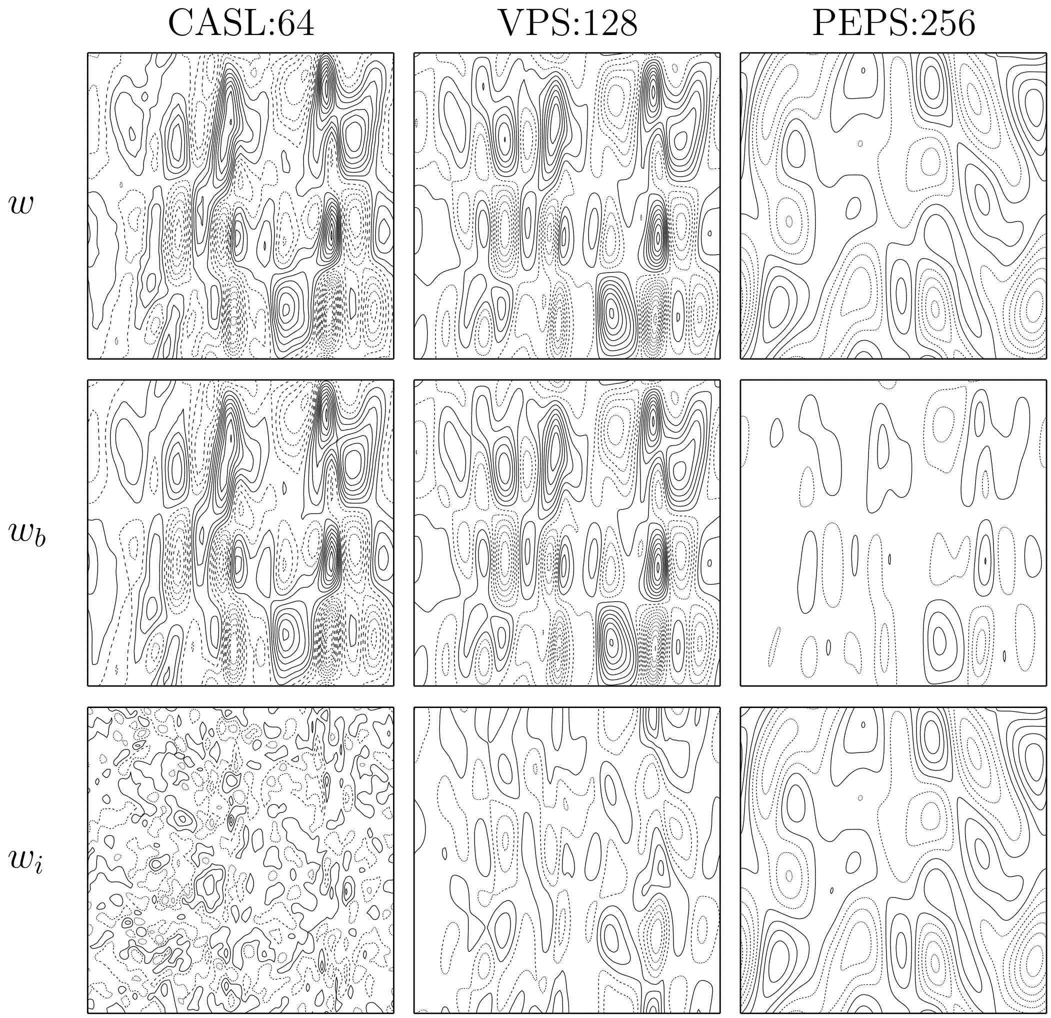

Figure 5.11: Comparison of the full (top row), balanced (middle row) and imbalanced (bottom row) components of the vertical velocity field, in a y=0 cross-section at t=10, for Ro=0.1. Plotted contours represent $\pm\Delta/2$, $\pm3\Delta/2$,...., $\pm(2n+1)\Delta/2$. Positive contours are represented by solid lines and negative contours by dashed lines. For CASL:64 and VPS:128 contour interval is $\Delta = 2\times10^{-6}$ for the full and balanced cases. Imbalanced contour interval is $\Delta/5$. For PEPS:256 the contour interval is Δ=5 $\times10^{-4}$ for the full and imbalanced cases. Balanced contour interval is $\Delta/100$.

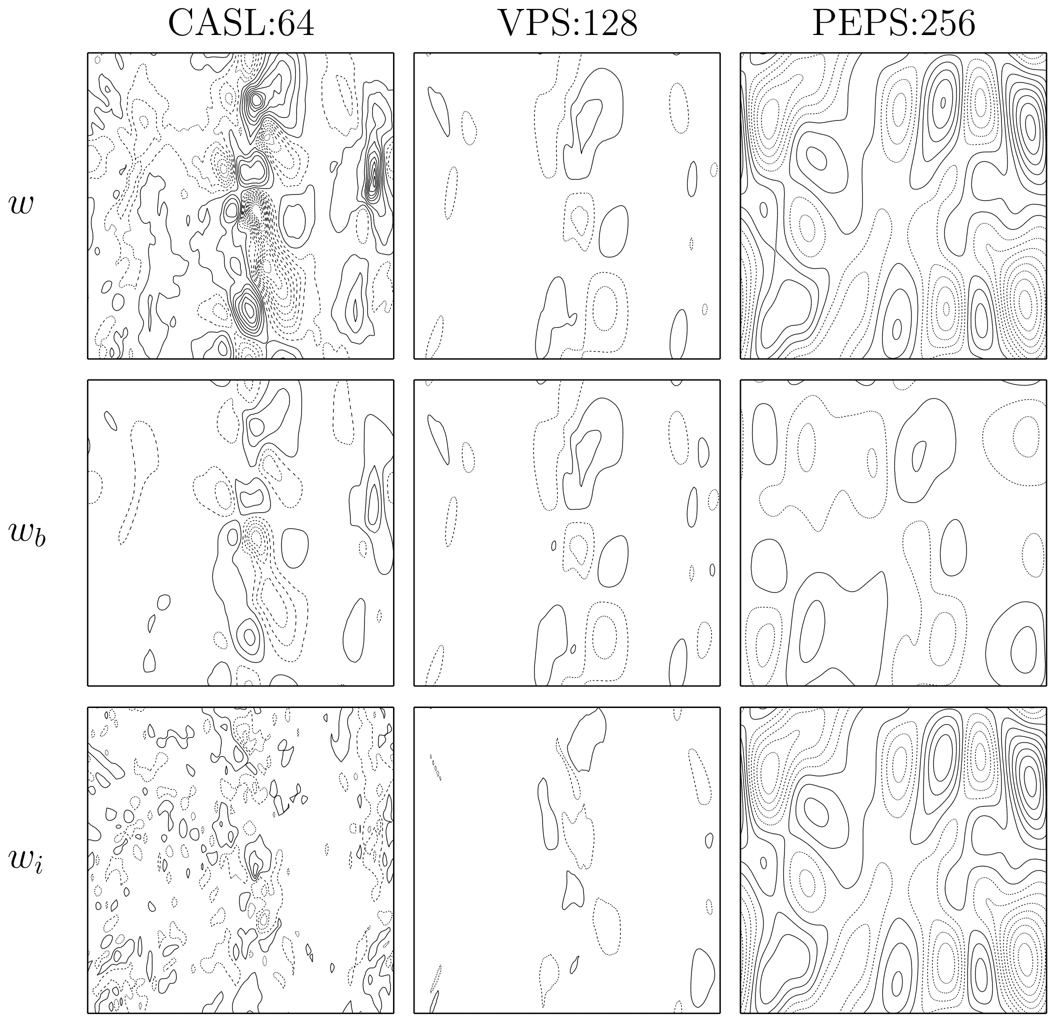

Figure 5.12: As in figure 5.11, for Ro=0.5. For CASL:64 and VPS:128 contour interval is Δ=5 $\times 10^{-4}$ for the full and balanced cases. Imbalanced contour interval is $\Delta/5$. For PEPS:256 the contour interval is Δ=1 $\times 10^{-3}$ for the full and imbalanced cases. Balanced contour interval is $\Delta/10$.

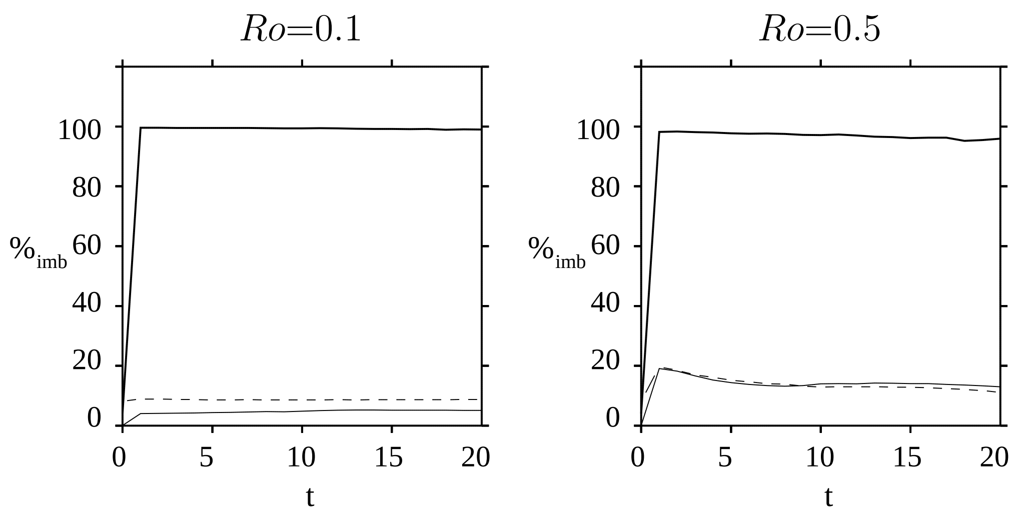

Figure 5.13: Time evolution of the percentage imbalance of w for (bold line) PEPS:256, (dashed line) VPS:128, (thin line), CASL:64, at *Ro* indicated. Note that each simulation is initialised with NQG balance.

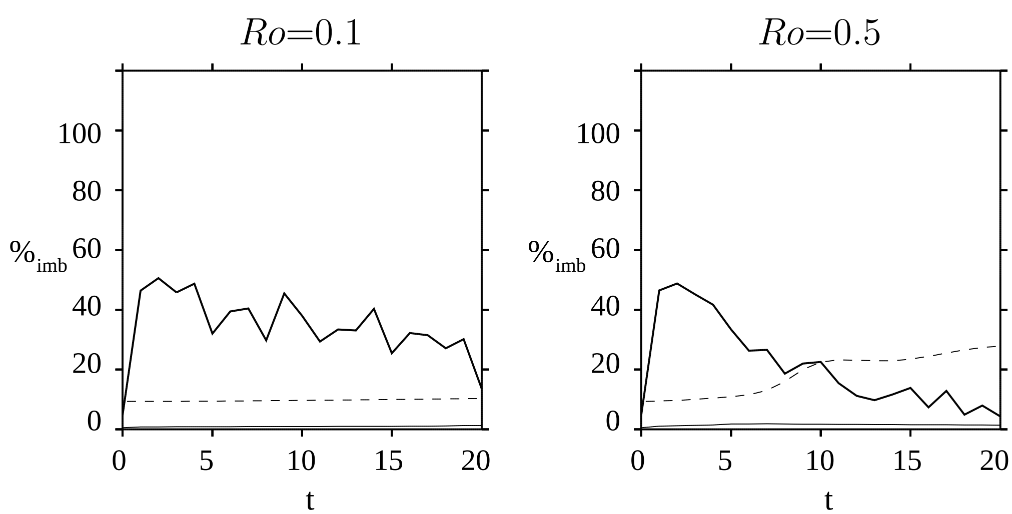

Figure 5.14: Time evolution of the percentage imbalance of $\mathcal{D}$ for (bold line) PEPS:256, (dashed line) VPS:128, (thin line), CASL:64. Note that each simulation is initialised with NQG balance.

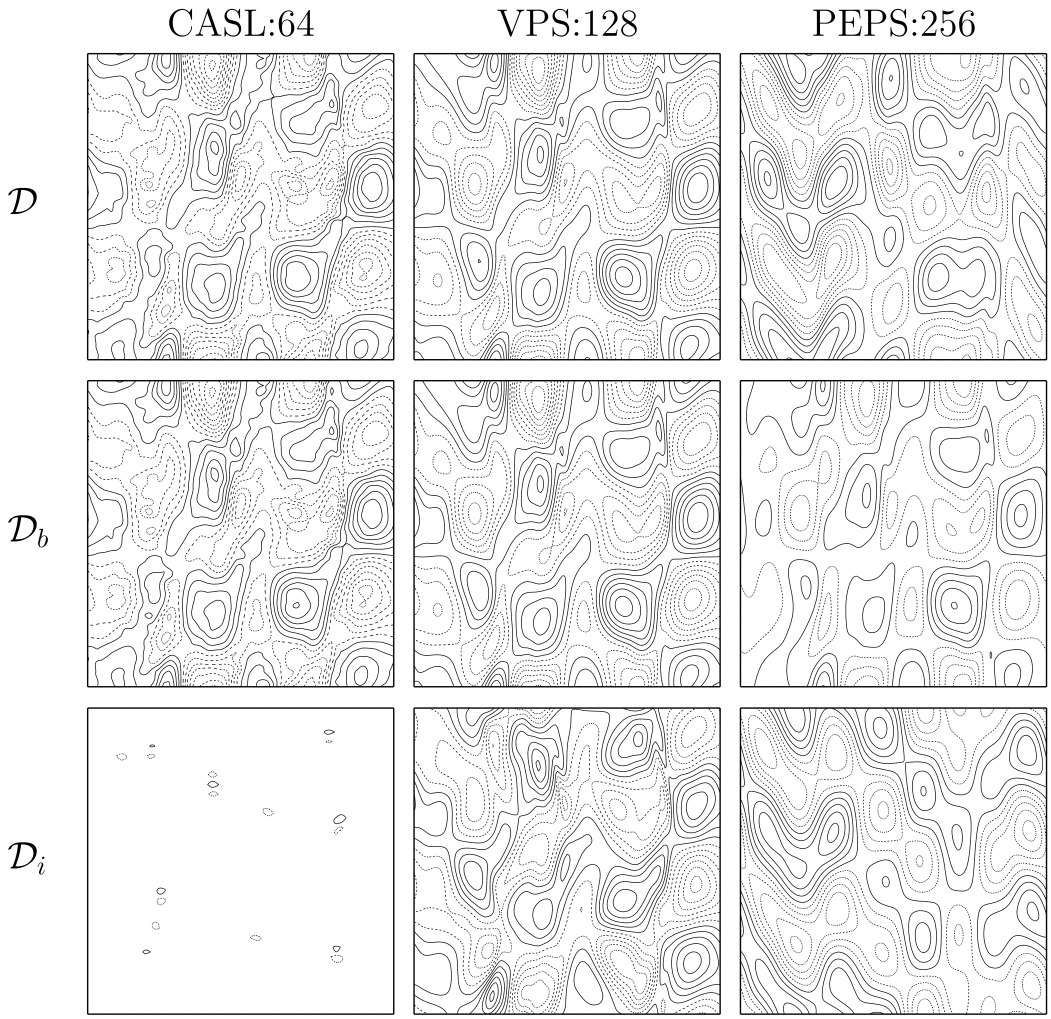

Figure 5.15: As in figure 5.11, for the isopycnal displacement, for *Ro*=0.1. Contour intervals for the full and balanced parts are Δ=5 $\times 10^{-4}$. For CASL:64 and VPS:128 the imbalanced contour interval is $\Delta/10$. For PEPS:256 the imbalanced contour interval is equal to the full and balanced parts.

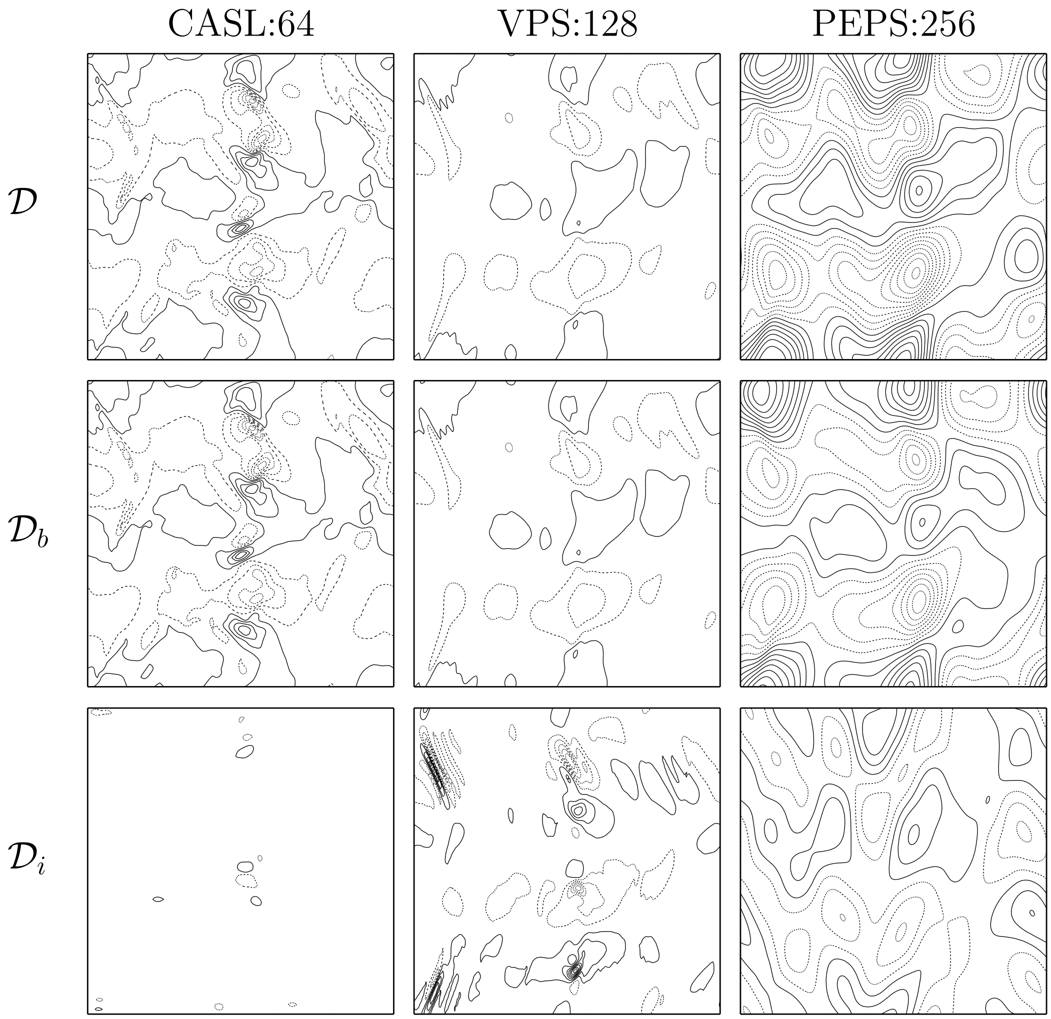

Figure 5.16: As in figure 5.15, for *Ro*=0.5. Contour intervals for the full and balanced parts are Δ=2 $\times 10^{-2}$. For CASL:64 and VPS:128 the imbalanced contour interval is $\Delta/10$. For PEPS:256 the imbalanced contour interval is equal to the full and balanced parts.

This is more evidence of the detrimental effect that the Laplacian diffusion has on the pseudospectral algorithms. This analysis is borne out by figure 5.13. This shows the evolution of the rms imbalance in w as a percentage of the full rms vertical velocity, namely $100|w_i|_{rms}/|w|_{rms}$. As expected the percentage imbalance of w in PEPS:256 was nearly 100% for the duration of the simulation. CASL:64 and VPS:128 exhibit substantially less imbalance with CASL:64 outperforming VPS:128 at Ro=0.1. The difference between the level of imbalance in w in CASL:64 and VPS:128 at Ro=0.5, is minimal.

Isopycnal displacement

The isopycnal displacement field $\mathcal{D}$ is analysed in much the same way as the vertical velocity field. Figure 5.15 contains the full ($\mathcal{D}$), balanced ($\mathcal{D}_b$), and imbalanced ($\mathcal{D}_i$) components of the isopycnal displacement field at time t=10 at Ro=0.1, for each of the three algorithms. Again the cross section here is vertical, at y=0. The general behaviour in each of these cross sections was replicated in all other cross sections of the isopycnal displacement components. Compared to the vertical velocity field w from figure 5.11 the isopycnal displacement field is much smoother and appears to be more balanced for CASL:64 and VPS:128 as the magnitude of the imbalanced fields are 10 times smaller rather than the 5 times smaller for w. As in figure 5.11 the full and balanced components $\mathcal{D}$ of CASL:64 and VPS:128 approximate each other to a good degree but there are major differences in $\mathcal{D}_i$. The imbalance captured by CASL:64 is minimal while most of the field in VPS:128 is populated by a smoothed out field approximated by the structure of the full and balanced fields. Again, PEPS:256 struggles. While $\mathcal{D}$ is of the same order of magnitude as CASL:64 and VPS:128 and appears very broadly to approximate CASL:64 and VPS:128 there are obvious differences in $\mathcal{D}_b$. In PEPS:256 $\mathcal{D}_i$ has the same magnitude as the full and balanced components. Furthermore, as in figure 5.11 the structure of the imbalanced component of $\mathcal{D}$

appears to approximate the full field more than the balanced component of $\mathcal{D}$ does.

In figure 5.16 the same comparison is drawn as in figure 5.15, but for Ro=0.5. As Ro is increased, so the differences in the performance of each algorithm increases. Dipolar structures appear in the $\mathcal{D}$ field of CASL. These structures in the vertical cross sections correspond to cyclonic PV anomalies where the isopycnals are being squeezed together while anticyclonic PV anomalies spread the isopycnals out. The same level of detail is not captured in the $\mathcal{D}$ field of VPS:128. As before, VPS:128 appears to capture more detail in $\mathcal{D}$ than in PEPS:256. It appears that the relatively high value of diffusion needed for the stability of PEPS:256 smooths out all of the meteorologically significant structures that we would expect to see within the flow. The magnitude of $\mathcal{D}_i$ in CASL:64 is minimal, even compared to $\mathcal{D}_i$ from the higher resolution VPS:128 simulation. Therefore, CASL:64 appears to be more accurate when representing the balanced component of the flow. Although important physical IGW activity may be overly dissipated, neither CASL:64, VPS:128 nor PEPS:256 seem appropriate for capturing real features of imbalance. This drawback is manageable due to the accurate capture of the large-scale vortical motion taking priority.

One point of note is that there appears to be evidence of wave packets in the imbalanced component of VPS:128. It is suspected that this structure may be spurious as there is no signal within the corresponding CASL:64 simulation and all other tests appear to indicate that CASL is more accurate.

In figure 5.14, similar to figure 5.13, the evolution of the rms imbalance in $\mathcal{D}$ as a percentage of the full rms isopycnal displacement, namely $100(|\mathcal{D}_i|_{rms}/|\mathcal{D}|_{rms})$ is shown. The percentage imbalance of $\mathcal{D}$ in CASL:64 is minimal at both Ro=0.1 and 0.5 and significantly smaller than the evolution of PEPS:256. While the level of imbalance in PEPS:256 for $\mathcal{D}$ is less than that of w from figure 5.12 there is still a significant level of imbalanced motion in PEPS:256. VPS:128 exhibits a higher level of imbalance than observed in CASL:64. Significantly at Ro=0.5 the percentage imbalance increases from around t=5 and eventually exhibits a higher level of imbalance than is observed in PEPS:256.

Therefore when comparing the three algorithms at Ro=0.1 & 0.5 we conclude that CASL:64 preserves the underlying balanced motions of the flow to a much greater degree than the VPS:128 algorithm which in turn outperforms PEPS:256, all achieved at lower resolutions. This demonstrates the benefits of employing algorithms where the prognostic variables have been transformed to take account of the underlying balance observed in geophysical flows. It emphasises again just how inaccurate at higher resolutions the pseudospectral algorithms are in this flow regime, compared to the contour-advective based CASL algorithm.

5.2.4 Computational efficiency

We have demonstrated some of the relative merits and strengths of each algorithm. We now turn our attention to assessing the computational efficiency of each algorithm. In a numerical forecasting context a compromise has to be made between the accuracy of a solution and the time taken (cost) to obtain the solution. One main factor in the cost of an algorithm is the time-step Δt used to solve the prognostic equations. The time-step of each algorithm is based on the value of Ro initially (see section §5.1.1). This accounts for a portion of the increased computational cost as Ro is increased.

At equivalent resolution the pseudospectral methods have a significant advantage over CASL in the computational cost required to perform simulations at a given Ro. Table 5.1 shows the time in CPU seconds required for each algorithm at the resolution and Ro indicated. When drawing a comparison between the cost of each algorithm we believe this should be done at different resolutions, as indicated by the 'diagonal' in table 5.1. Comparing pseudospectral algorithms, VPS

				t=5					
Resolution	64^3			128^3			256^3		
Ro	0.1	0.3	0.5	0.1	0.3	0.5	0.1	0.3	0.5
PEPS	58.4	58.4	58.4	561.7	561.7	561.7	10476.7	10476.7	10476.7
VorPS	114.3	114.3	114.3	1185.5	1185.5	1185.5	23327.9	23327.9	23327.9
CASL	177.6	177.7	177.8	4610.5	5326.0	7058.4	n/a	n/a	n/a
				t=10					
Resolution	64^3			128^3			256^3		
Ro	0.1	0.3	0.5	0.1	0.3	0.5	0.1	0.3	0.5
PEPS	116.9	116.9	116.9	1123.3	1123.3	1123.3	20953.5	20953.5	20953.5
VorPS	228.5	228.5	228.5	2371.0	2371.0	2371.0	46655.7	46655.7	46655.7
CASL	351.2	352.4	355.8	9060.7	12198.1	19769.1	n/a	n/a	n/a

Table 5.1: Comparison of the computational duration in CPU seconds of a t=5 and t=10 inertial periods, for each algorithm, at varying resolution and Ro_{max}, on an Intel(R) Core(TM) 2 Duo CPU E6850 @3.00GHz. Note that only a single core is used for each run. The computational resources available for this study did not allow CASL to be run at 256^3 resolution.

requires approximately double the computational resources that PEPS requires, at each resolution and Ro. This extra cost in VPS arises from the iterative inversion process required to recover the primitive variables of the system. An increase in the simulation time as resolution increases is due not only to the increase in the total number of grid points N (recall that FFTs have a cost proportional to $N \log N$) but also the time step Δt is halved to maintain a CFL number of $0.25 \sim 0.3$, for resolutions greater than 128^3. The consistency in the cost differential between pseudospectral algorithms is expected due to the Eulerian nature of the numerical method. This is not the case with CASL. As Ro increases CASL becomes significantly more expensive than its pseudospectral counterparts even at lower resolution, as more iterations are required to solve the non-linear double Monge-Ampère equation for the vertical potential, (2.54). One expects that CASL will be more cost effective than the pseudospectral algorithms at low Ro but accepts that the computational effort required as Ro increases will limit the suitability of CASL to model three-dimensional geophysical flows. Therefore we wish to diagnose the value of Ro above which it would be sensible to use a pseudospectral method rather than CASL in the modelling of such flows.

To assess the efficiency of each algorithm we diagnose the convergence rates with increasing resolution (cost) by calculating the error at time t, given by (5.3), defined as the relative rms difference in the vertical velocity field at 128^3 with 64^3, 32^3 and 16^3 normalised by the product of the rms values of each field,

$$\varepsilon(t) = \left(\frac{\frac{\sum_N w_{128} - w_i)^2}{N}}{\left(\frac{\sum_N w_{128}^2}{N}\right)^{1/2} \left(\frac{\sum_N w_i^2}{N}\right)^{1/2}} \right)^{1/2}, \qquad i = 16, 32, 64, \tag{5.3}$$

where N is the number of grid points. These values are shown in figure 5.17. At these coarse resolutions PEPS does not appear to benefit from an increase in resolution at any value of Ro. Therefore when considering which algorithm is the most cost-effective PEPS will be discounted in the following discussion.

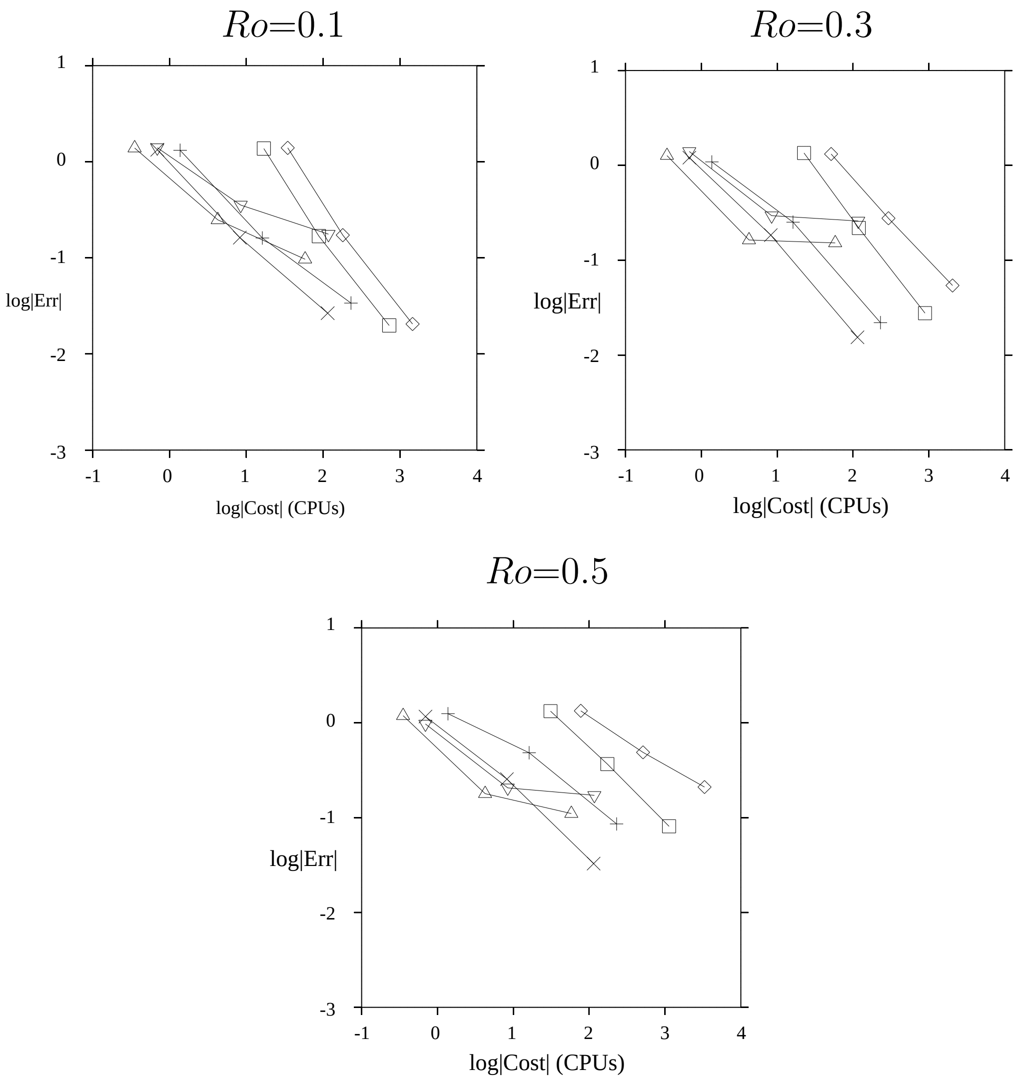

Figure 5.17: A log-log (base 10) plot of the relative rms difference in the vertical velocity field as defined by (5.3). Related symbols indicate the algorithm used: squares and diamonds represent CASL, pluses and crosses represent VPS and triangles and inverted triangles represent PEPS, at t=5 and t=10 inertial periods respectively, at the Ro indicated.

At Ro=0.1, CASL has the strictest convergence with increasing resolution combined with smallest error at each time but at an additional cost compared to the pseudospectral algorithms. If this trend continued at higher resolution CASL would be the most cost-effective algorithm in this regime. At Ro=0.3, CASL no longer has the smallest error at each time at each resolution but still has a convergence rate comparable to that of VPS. At Ro=0.5, CASL has a larger error than VPS at a significantly higher cost. The convergence rate of CASL is no longer superior to that of VPS suggesting that there is limited merit in using CASL at $Ro \geq 0.5$, although table 5.1 suggests that CASL is still orders of magnitude less computationally expensive. It should also be noted here that the reference vertical velocity field in the pseudospectral algorithms are very diffuse, even at t=5 and so a relative rms difference between different resolutions may not be the best possible method of assessing the accuracy of the pseudospectral algorithms.

Of course, the resolution afforded for this study is grossly insufficient compared to the computational power available to major modern forecast centres around the world. By extrapolation it appears that CASL will become more accurate and will cost less than the pseudospectral algorithms at low Ro.

In addition we argued previously that the correct comparison was to be made at differing resolution as CASL at worst replicates, and at best improves upon the representation of the flow, at lower resolution. Even factoring in the extra cost shown in table 5.1, CASL can be used at a much lower resolution and is therefore much more efficient up to Ro=0.3.

5.3 Conclusion

In this chapter we have presented a comparison of algorithms that solve the non-hydrostatic Boussinesq equations. Diffusion impacts on the accuracy of each method, specifically in the representation of PV, a key dynamical field. In pseudospectral terms, the transformation of the prognostic variables of the system to take account of leading order geostrophic and hydrostatic balance decreases the numerical diffusion required for computational stability. In contrast, the diffusion in the contour-advective based CASL algorithm acts at the sub-grid scale allowing a much more detailed and accurate flow, crucially, at much lower grid resolution.

Although this study was restricted by the computational resources available we have demonstrated that CASL performs just as well, or better than VPS and PEPS, at lower resolution in a number of comparisons. Therefore, we believe that we have delivered a convincing case that when comparing the cost of the algorithms, this should be done at CASL:64 - VPS:128 - PEPS:256. CASL is able to model more physically realistic values of Rossby and Froude numbers as the pseudospectral algorithms diffuse much of the significant physical motion. Furthermore, the representation of the balanced component of the flow was by CASL was superior to VPS and PEPS, as diagnosed by the NQG balance routine.

We then observed a limitation of CASL, for initial $Ro \sim \mathcal{O}(1)$, where static instabilities within the flow causes CASL to diverge. From chapter §3 we argue that this should not be a problem providing CASL is employed at the appropriate scale.

We have tried to address the question of which algorithm will be most cost-effective as resolution is increased, in anticipation of operational use. At Ro=0.1 we have demonstrated that CASL appears to converge more rapidly than VPS giving a more accurate solution giving a smaller error, in less time, if, as we argue, the cost comparison is made at differing resolution as CASL:64 outperforms VPS:128, which in turn outperforms PEPS:256.

As Ro is increased CASL still exhibits more detail and fine-scale structure than

PEPS and VPS, the cost of obtaining this solution becomes prohibitive. We discovered that for regimes with predominantly $Ro \leq 0.3$ that the CASL algorithm would give the most efficient, cost-effective solution in operational models.

Chapter 6

Conclusions and further work

This chapter presents a summary of the main findings from this study from the preceding chapters. We also discuss the potential for an extension to the work here.

The aim of this thesis was to undertake a wide-ranging study of the use of properties of balance in an operational NWP context. We investigated three distinct, but related areas.

The first major question we had to address was, if an operational NWP centre, like the UKMO were to use a balanced model operationally, on what horizontal scale in the atmosphere would the model be valid on. It is anticipated that a balanced model of a geophysical flow should 'filter' imbalanced motions from its solution, accurately capturing the large-scale dynamics of the flow. We estimate that a balanced model of the atmosphere should not expect to model a feature of imbalance such as a symmetric instability (SI) for a horizontal grid scale below approximately 20-25km. A determination of this length scale is also of interest to users of the UM as it allows the potential for the detection of errors in the solution of the full model, which can then be rectified to improve the accuracy with which the UKMO delivers its forecasts, benefiting the individual and the wider society as a whole.

Further work on this area may include an expansion of the observational component of the study to gather different, independent evidence from different sources to get a more accurate estimate of the scale at which vortical-based motions persist in the atmosphere. One source of such data would be the British Atmospheric Data Centre (BADC).

We then investigated the robustness of the CASL algorithm in the shallow water context by comparing two formulations, differing by prognostic variables employed, each chosen to try and distinguish the scale separation that exists in the modes of solution of the shallow water model and exists, to a good approximation in geophysical flows. We found that with the appropriate choice of prognostic variable in this context (potential vorticity, divergence and acceleration divergence), denoted as $\mathrm{CA}_{\delta,\gamma}$, CASL adapts favourably to having its three-time-level semi-implicit integration scheme de-centred, mimicking the numerical set-up of the UM. We also investigated the potential for gains in the efficiency of $\mathrm{CA}_{\delta,\gamma}$ by increasing the time-step used and reducing the convergence criteria for the expensive inversion relations that need to be solved to recover the primitive variables of the system.

Further work should involve modeling atmospheric data to assess how the numerical methods deal with real-world flows. Furthermore, the various extensions to the CASL algorithm should be investigated to include forcing and non-conservative effects into the algorithm, Dritschel & Ambaum (2006), Fontane & Dritschel (2009), Dritschel & Fontane (2010) as this will allow a solution which is closer to physical reality.

Lastly, we compared CASL to spectral-based methods in the non-hydrostatic model under the Boussinesq approximation. This was important as it gave a context nearer to reality than the shallow water model in which to test the numerics of the CASL algorithm for the potential use in an operational forecasting context. Also, comparing CASL to two pseudospectral algorithms highlighted the potential gains in efficiency that major forecast centres around the globe could be making if they were to employ numerical techniques such as the CASL algorithm. Compared to the spectral-based algorithms, at $Ro \ll 1$ CASL produces a much less diffuse, more physically realistic solution at much lower resolution, and therefore for much less computational effort, highlighting the potential gains in efficiency.

Further efforts in this area should focus on increasing the computational resources available for such a comparative study. It is noted that we have most likely not seen the full potential of the spectral-based methods due to the relatively low resolution used in the comparison.

Appendix A

Derivation of the quasi-geostrophic model

A key regime of the non-hydrostatic Boussinesq equations (2.50) is the quasi-geostrophic regime. This simplifies the governing equations by assuming that the flow is, at leading order, in geostrophic and hydrostatic balance, where variations in the vertical velocity w can be neglected. The quasi-geostrophic equations are now derived.

Equations (2.50) can be non-dimensionalised by expressing each in terms of the relevant scale. These are $t \sim T,\ x, y \sim L,\ z \sim H,\ f \sim f_0,\ N \sim N_0,\ u, v \sim U,\ w \sim W,\ p'/\rho_0 \sim P$ and $b' \sim B$. The non-dimensional buoyancy and horizontal velocity become, in terms of the Rossby number Ro

$$B = \frac{P}{H} = Ro\frac{(f_0 L)^2}{H}, \qquad \& \qquad U = \frac{P}{f_0 L} = Ro f_0 L, \tag{A.1}$$

while a non-linear timescale T is taken to be

$$T = \frac{L}{U}. \tag{A.2}$$

An estimate of W is taken from (2.50b) to be

$$W = \frac{B}{{N_0}^2 T} = \frac{BU}{{N_0}^2 L} = \frac{P^2}{f_0 {N_0}^2 H L^2} = Ro^2 \frac{{f_0}^3 L^2}{{N_0}^2 H}. \tag{A.3}$$

Non-dimensionalising, the horizontal components of the momentum equations (2.50a) and (2.50b) can be expressed as

$$Ro\left(\frac{\partial u}{\partial t} + u\frac{\partial u}{\partial x} + v\frac{\partial u}{\partial y}\right) + Fr^2 w\frac{\partial u}{\partial z} - fv = -\frac{\partial p'}{\partial x}, \tag{A.4}$$

$$Ro\left(\frac{\partial v}{\partial t} + u\frac{\partial v}{\partial x} + v\frac{\partial v}{\partial y}\right) + Fr^2 w\frac{\partial v}{\partial z} + fu = -\frac{\partial p'}{\partial y}, \tag{A.5}$$

while the vertical momentum equation becomes

$$Ro^2\left(\frac{f_0}{N_0}\right)\left(\frac{\partial w}{\partial t} + u\frac{\partial w}{\partial x} + v\frac{\partial w}{\partial y}\right) + RoFr^2\left(\frac{f_0}{N_0}\right)^2 w\frac{\partial w}{\partial z} = -\frac{\partial p'}{\partial z} + b'. \tag{A.6}$$

Also f_0/N_0 is small at mid-latitudes, typically of order 0.1 in the atmosphere and 0.001 in the oceans. Equation (2.50b) becomes

$$\frac{\partial b'}{\partial t} + u\frac{\partial b'}{\partial x} + v\frac{\partial b'}{\partial y} + Ro^{-1}Fr^2 w\frac{\partial b'}{\partial z} + N^2 w = 0. \tag{A.7}$$

and finally, the isochoric condition becomes

$$\frac{\partial u}{\partial x} + \frac{\partial u}{\partial y} + Ro^{-1}Fr^2\frac{\partial w}{\partial z} = 0. \tag{A.8}$$

At $\mathcal{O}(Ro)$, (A.4) and (A.5) reduce to the statement of geostrophic balance

$$-fv = \frac{1}{\rho_0}\frac{\partial p}{\partial x}, \qquad fu = \frac{1}{\rho_0}\frac{\partial p}{\partial y}, \qquad w = 0, \qquad b = \frac{1}{\rho_0}\frac{\partial p}{\partial z}. \tag{A.9}$$

Introducing $\psi{=}p/\rho_0 f$ we obtain

$$u = -\frac{\partial \psi}{\partial y}, \qquad v = \frac{\partial \psi}{\partial x} \quad \& \quad b = \frac{1}{\rho_0}\frac{\partial p}{\partial z}. \tag{A.10}$$

We now introduce the potential vorticity q:

$$q = \omega_a \cdot \nabla b = (f\mathbf{k} + \omega) \cdot (N^2\mathbf{k} + \nabla b'), \tag{A.11}$$

where ω_a is the absolute vorticity and b is the buoyancy, with b' a small perturbation in the buoyancy. Keeping terms up to $\mathcal{O}(Ro)$ in q creates mean and perturbation components $q{=}q_m + q_p$ where

$$q_m(z) = fN^2 \quad \& \quad q_p(\mathbf{x}, t) = N^2\zeta + f\frac{\partial b'}{\partial z}. \tag{A.12}$$

We now aim to express q in terms of a streamfunction ψ.

Having expressed each term in (A.11) in terms of ψ we now turn our attention to demonstrating the material conservation of q, namely

$$\frac{Dq}{Dt} = 0, \tag{A.13}$$

where $\frac{D}{Dt} \equiv \frac{\partial}{\partial t} + u\frac{\partial}{\partial x} + v\frac{\partial}{\partial y}$ is the material derivative. Retaining terms up to $\mathcal{O}(Ro^2)$ gives

$$\frac{\partial q_p}{\partial t} + u\frac{\partial q_p}{\partial x} + v\frac{\partial q_p}{\partial y} + w\frac{\partial q_m}{\partial z} = 0, \tag{A.14}$$

while rearranging for w in equation (2.50b) and substituting $q_m{=}fN^2$ into (A.14) gives

$$\frac{Dq_p}{Dt} - \frac{1}{N^2}\frac{dN^2}{dz}\frac{Db'}{Dt} = 0. \tag{A.15}$$

Now, in terms of the streamfunction ψ

$$q_p = N^2 {\nabla^2}_h \psi + f^2 \frac{\partial^2 \psi}{\partial z^2}, \tag{A.16}$$

which gives

$$\frac{DQ}{Dt} = 0, \tag{A.17}$$

where

$$Q = {\nabla^2}_h \psi + \frac{\partial}{\partial z}\left(\frac{f^2}{N^2}\frac{\partial \psi}{\partial z}\right). \tag{A.18}$$

Given Q, it can be inverted to find ψ and hence u & v.

The set of quasi-geostrophic equations are commonly expressed in the form

$$\frac{DQ}{Dt} = 0, \tag{A.19a}$$

$$\Delta\psi = Q, \tag{A.19b}$$

$$u = -\frac{\partial \psi}{\partial y}, \qquad v = \frac{\partial \psi}{\partial x}, \tag{A.19c}$$

where z has been scaled by N/f.

The quasi-geostrophic regime is an important limit of the governing equations as, to a good approximation, the large scale behaviour of the atmosphere is in geostrophic and hydrostatic balance with negligible variations in the vertical velocity, compared to the horizontal velocity. Equations (A.19) are also used in the construction of a balancing procedure, non-linear quasi-geostrophic (NQG) balance, McKiver & Dritschel (2008), which is used to diagnose the balance within a flow. Details are given in appendix B.

Appendix B

Derivation of the nonlinear quasigeostrophic (NQG) balance routine

Non-linear quasi-geostrophic (NQG) balance, McKiver & Dritschel (2008), is a procedure which diagnoses the extent to which a given flow is in balance, at an instant in time. Here the formulation of the procedure is reproduced.

NQG balance is a procedure based on the reformulation of the non-hydrostatic equations (2.50), Dritschel & Viúdez (2003). For completeness the transformed prognostic equations in terms of the PV anomaly and the horizontal components of the ageostrophic vorticity are restated here

$$\frac{D\varpi}{Dt} = 0, \tag{B.1a}$$

$$\frac{D\mathcal{A}}{Dt} = -f\mathbf{k}\times\mathcal{A} + (1+c^2)\nabla w + \frac{\boldsymbol{\omega}}{f}\cdot\nabla\mathbf{u} + c^2\nabla\mathbf{u}\cdot\nabla\mathcal{D}, \tag{B.1b}$$

where

$$\varpi = \Pi - 1, \quad \& \quad \Pi = 1 + \frac{\zeta}{f} + \frac{1}{N^2}\frac{\partial b}{\partial z} + \frac{\omega \cdot \nabla b}{f N^2}. \tag{B.2}$$

As discussed in section §2.6 the primitive variables are recovered by inverting $\mathcal{A}_h$ and ϖ through the introduction of a vector potential $\boldsymbol{\varphi}=(\varphi, \psi, \phi)$. The horizontal components of $\boldsymbol{\varphi}$ are obtained by inverting Laplace's operator on $\mathcal{A}_h$ while the vertical component of $\boldsymbol{\varphi}$ is obtained from ϖ through the solution of a double Monge-Ampére equation

$$\mathcal{L}_{qg}\phi = \varpi + (1 - c^{-2})\Theta_z - c^{-2}\mathcal{N}(\boldsymbol{\varphi}), \tag{B.3}$$

where $\mathcal{L}_{qg}$ is the QG operator defined by

$$\begin{aligned} \mathcal{L}_{qg} &\equiv \phi_{xx} + \phi_{yy} + c^{-2}\phi_{zz}, && \text{(B.4)} \\ \Theta &\equiv \nabla_h \cdot \boldsymbol{\varphi}_h, && \text{(B.5)} \\ \mathcal{N}(\boldsymbol{\varphi}) &\equiv \nabla(\nabla \cdot \boldsymbol{\varphi}) \cdot [\nabla^2 \boldsymbol{\varphi} - \nabla(\nabla \cdot \boldsymbol{\varphi})]. && \text{(B.6)} \end{aligned}$$

This reformulation makes explicit the separation between the leading order geostrophic and hydrostatic balance and the departure from these balances.

The NQG balance procedure removes two time derivatives from the horizontal ageostrophic vorticity components. This filters the IGWs. This is similar to the Bolin-Charney balance used in chapter 4 in the shallow water context. The added novelty in this method is the use of an un-approximated form of the full PV to eliminate the IGWs.

To obtain the NQG balance, quasi-geostrophic scaling is applied to equations (2.50) to obtain ageostrophic balanced fields at $\mathcal{O}(Ro^2)$. QG balance is generalised in terms of $\epsilon \equiv |\varpi|_{max}$, a PV-based Rossby number. The dimensionless ageostrophic vorticity $\mathcal{A}_h$ is $\mathcal{O}(\epsilon^2)$ as the flow is assumed to be in thermal-wind balance at leading order. This can be expressed by expanding the vector potential $\boldsymbol{\varphi} \equiv (\varphi, \psi, \phi)$ in ϵ as

$$\boldsymbol{\varphi} = \boldsymbol{\varphi}_1 + \boldsymbol{\varphi}_2 + \mathcal{O}(\epsilon^3), \tag{B.7}$$

taking $\boldsymbol{\varphi}_1$=$\mathcal{O}(\epsilon)$, $\boldsymbol{\varphi}_2$=$\mathcal{O}(\epsilon^2)$ and $\varphi_1 = \psi_1 = 0$. Inserting this expansion into equations (2.50) we obtain, at $\mathcal{O}(\epsilon)$ the standard linearly balanced QG equations

$$\mathcal{L}_{qg}\phi_1 = \varpi, \tag{B.8a}$$
$$\frac{D\varpi}{Dt} = 0, \tag{B.8b}$$
$$u_1 = -f\frac{\partial \phi_1}{\partial y}, \qquad v_1 = f\frac{\partial \phi_1}{\partial x}. \tag{B.8c}$$

At $\mathcal{O}(\epsilon^2)$ there are an infinite number of conditions that which can close this system of equations. Here, the linear component of the PV anomaly must vanish at $\mathcal{O}(\epsilon^2)$. This has been found to capture the greatest proportion of the balance. With this condition equations (B.1b) and (B.3) reduce to

$$c^2\mathcal{L}_{qg}\boldsymbol{\varphi}_2 + (1-c^2)\nabla\Theta_2 = \mathcal{S}, \tag{B.9}$$

where $\Theta_2 \equiv \nabla_h \cdot \boldsymbol{\varphi}_2$ and the vector $\mathcal{S} \equiv (\mathcal{S}_\varphi, \mathcal{S}_\psi, \mathcal{S}_\phi)$ where

$$\mathcal{S}_\varphi = -2J_{yz}(\frac{\partial \phi_1}{\partial x}, \frac{\partial \phi_1}{\partial y}), \tag{B.10a}$$
$$\mathcal{S}_\psi = -2J_{zx}(\frac{\partial \phi_1}{\partial x}, \frac{\partial \phi_1}{\partial y}), \tag{B.10b}$$
$$\mathcal{S}_\phi = 0, \tag{B.10c}$$

where $J_{yz}(a,b)$=$a_y b_z - a_z b_y$ is the Jacobian ($J_{zx}(a,b)$ is analogous). The vertical component of equation (B.9) together with equation (B.10c) express the condition $\zeta_2/f + \frac{1}{N^2}\frac{\partial b_2}{\partial z} = 0$, cf. (B.2).

In a triply periodic domain, these non-linear QG equations are solved most readily in spectral space to give

$$\hat{\varphi}_2 = \hat{\mathcal{F}}[c^2\hat{\mathcal{F}}_{\varphi xx} + \hat{\mathcal{S}}_{\varphi yy} + \hat{\mathcal{S}}_{\varphi zz} + (c^2-1)\hat{\mathcal{S}}_{\psi xy}], \tag{B.11a}$$

$$\hat{\psi}_2 = \hat{\mathcal{F}}[c^2\hat{\mathcal{S}}_{\psi yy} + \hat{\mathcal{S}}_{\psi zz} + \hat{\mathcal{S}}_{\psi xx} + (c^2-1)\hat{\mathcal{S}}_{\varphi xy}], \tag{B.11b}$$

$$\hat{\phi}_2 = \hat{\mathcal{F}}K^2(1-c^2)(\hat{\varphi}_{2xz} + \hat{\psi}_{2yz}), \tag{B.11c}$$

where $\hat{\chi}$ is the spectral transform of the field χ, K is the three-dimensional wavenumber defined as $K^2 \equiv k^2+l^2+m^2$ and $\hat{\mathcal{F}}$=$1/[K^2(c^2(k^2+l^2)+m^2)]$. Thus knowing the $\mathcal{O}(\epsilon)$ fields satisfying equations (B.8) we can solve for the next order using equations (B.11).

This analysis is incomplete if the exact unexpanded definition of PV is used. Here the QG PV inversion equation (B.8a) is replaced by the exact non-linear Monge-Ampére equation (B.3). This provides ϕ not ϕ_1. The latter is recovered by the difference ϕ_1=$\phi - \phi_2$, where ϕ_2 is found from the vertical component of equation (B.9) or equivalently from (B.11c). This implies that the equations at $\mathcal{O}(\epsilon)$ (B.8a) and $\mathcal{O}(\epsilon^2)$ (B.9) are coupled non-linearly.

In practice a solution to these coupled equations is found by iteration. For the initial iteration n=1 both the first- and second-order fields are set to zero ($\boldsymbol{\varphi}^{n-1}$=$\boldsymbol{\varphi}^0$ =$\boldsymbol{\varphi}_1^0$=$\boldsymbol{\varphi}_2^0 = 0$) and then proceed as follows

(1) Invert the PV (B.3) using $\boldsymbol{\varphi}^{n-1}$ in (B.6) and in (B.5) to obtain ϕ^n;

(2) Obtain an approximation to ϕ_1^n from ϕ_1^n=$\phi^n - \phi_2^{n-1}$;

(3) Use ϕ_1^n in (B.10) and (B.11) to obtain $\boldsymbol{\varphi}_2^n$;

(4) Return to **(1)** if $|\phi_1^n + \phi_2^n - \phi^n|$ is greater than a prescribed tolerance.

Hence, starting with ϖ at the time to be diagnosed, step (1) provides ϕ which is equal to ϕ_1 initially. From ϕ_1 the next order fields can be calculated from step (3). Using these fields in (1) again gives a better approximation to the balanced fields to O(ϵ^2). Then (2) gives an improved approximation to ϕ_1 and this is used in (3) to calculate the next order fields. In practice, iteration takes place until the point-wise difference in ϕ^n and ${\phi_1}^n + {\phi_2}^n$ is less than 10^{-7}. Upon convergence $\phi_1 + \phi_2 = \phi$.

Bibliography

[1] Anderson, S.R. & Roulstone, I. Derivation and calculation of unified model potential vorticity and the calculation of potential temperature on PV surfaces. *Unified Model Documentation Paper No.13*, 1993.

[2] Arakawa, A & Lamb, V.R. Computational design of the basic dynamical processes of the UCLA general circulation model. *Methods Comput. Phys.*, **17**, 173-265, 1977.

[3] Arakawa, A & Konor, C.S. Vertical differencing of the primitive equations based on the Charney-Phillips grid in hybrid $\rho - p$ vertical coordinates. *Mon. Wea. Rev.*, **124**, 511-528, 1996.

[4] Asselin, R. Frequency filter for time integrations. *Mon. Wea. Rev.*, **100**, 487-490, 1972.

[5] Bannister, R.N. & Cullen, M.J.P. The implementation of a PV-based leading control variable in variational data assimilation. Part I: transforms. *DARC Technical report no.6*, 2006.

[6] Bell, R.S., Lorenc, A.C., MacPherson, B., Swinbank, R. & Andrews, P. The analysis correction data assimilation scheme. *Unified Model Documentation Paper No.30*, 1993.

[7] Bennetts, D.A. & Hoskins, B.J. Conditional symmetric instability - a possible explanation for frontal rainbands. *Quart. J. Roy. Meteorol. Soc.*, **105**, 945–962, 1979.

[8] Bloom, S.C., Takacs, L.L., Da Silva, A.M. & Ledvina, D. Data assimilation using incremental analysis updates. *Mon. Wea. Rev.*, **124**, 1256-1271, 1996.

[9] Bolin, B. Numerical forecasting with the barotropic model. *Tellus*, **7**, 27–49, 1955.

[10] Bougealt, P., Binder, P., Buzzi, A., Dirks, R., Houze, R., Kuettner, J., Smith, R.B., Steinacker, R. & Volkert, H. The MAP special observing period. *Bull. Amer. Meteor. Soc.* **82**, 433-462, 2001.

[11] Browning, K.A., Blyth, A.M., Clark, P.A., Corsmeier, U., Morcrette, C.J., Agnew, J.L., Ballard, S.P., Bamber, D., Barthlott, C., Bennett, L.J., Beswick, K.M., Bitter, M., Bozier, K.E., Brooks, B.J., Collier, C.G., Davies, F., Deny, B., Dixon, M.A., Feuerle, T., Forbes, R.M., Gaffard, C., Gray, M.D., Hankers, R., Hewison, T.J., Kalthoff, N., Khodayar, S., Kohler, M., Kottmeier, C., Kraut, S., Kunz, M., Ladd, D.N., Lean, H.W., Lenfant, J., Li, Z., Marsham, J., McGregor, J., Mobbs, S.D., Nicol, J., Norton, E., Parker, D.J., Perry, F., Ramatschi, M., Ricketts, H.M.A., Roberts, N.M., Russell, A., Schulz, H., Slack, E.C., Vaughan, G., Waight, J., Wareing, D.P., Watson, R.J., Webb, A.R. & Weiser, A. The Convective Storm Initiation Project. *Bull. Amer. Meteor. Soc.*, 2007.

[12] Charney, J.G. The use of primitive equations of motion in numerical prediction. *Tellus*, **7**, 22–26, 1955.

[13] Clayton, A. Incremental analysis update (IAU) scheme. *Unified Model Documentation Paper No.31*, 2003.

[14] Cullen, M.J.P. *A mathematical theory of large-scale atmosphere/ocean flow. Imperial College Press*, 2006.

[15] Davies, T., Cullen, M.J.P., Malcolm, A.J., Mawson, M.H., Staniforth, A., White, A.A. & Wood, N. A new dynamical core for the Met Office's global and regional modeling of the atmosphere. *Quart. J. Roy. Meteorol. Soc.*, **131**, 1759-1782, 2005.

[16] Dritschel, D.G., Contour dynamics and contour surgery: numerical algorithms for extended, high resolution modeling of vortex dynamics in two-dimensional, inviscid, incompressible flows. *Comp. Phys. Rep.*, **10**, 77-146, 1989.

[17] Dritschel, D.G., A new spherical shallow-water model: building in wave-vortex decomposition. Seminar on recent developments in numerical methods for atmospheric and oceanic modeling, 6-10 September 2004, ECMWF, *http://www.ecmwf.int/newsevents/meetings/annual_seminar/2004* .

[18] Dritschel, D.G. & Ambaum, M.H.P. A contour-advective semi-Lagrangian numerical algorithm for simulating fine-scale conservative dynamical fields. *Quart. J. Roy. Meteorol. Soc.*, **123**, 1097–1130, 1997.

[19] Dritschel, D.G. & Viúdez, A. A balanced approach to modeling rotating stably stratified geophysical flows. *J. Fluid. Mech.*, **488**, 123-150, 2003.

[20] Dritschel, D.G & Ambaum, M.H.P. The diabatic contour advective semi-Lagrangian model. *Mon. Wea. Rev.*, **134**, 2503-2514, 2006.

[21] Dritschel, D.G. & Vanneste, J. Instability of a shallow water potential-vorticity front. *J. Fluid. Mech.*, **561**, 237–254, 2006.

[22] Dritschel, D.G. & Viúdez, A. The persistence of balance in geophysical flows. *J. Fluid. Mech.*, **570**, 365-383, 2007.

[23] Dritschel, D.G. & Fontane, J. The combined Lagrangian advection method. *J. Comp. Phys.*, **229**, 5408-5417, 2010.

[24] Dritschel, D.G., Polvani, L.M. & Mohebalhojeh, A.R. The contour-advective semi-Lagrangian algorithm for the shallow water equations. *Mon. Weather Rev.* , **127**, 1551-1565, 1999.

[25] Dritschel, D.G., Tran, C.V. & Scott, R.K. Revisiting Batchelor's theory of two-dimensional turbulence. *J. Fluid. Mech.*, **591**, 379-391, 2007.

[26] Emanuel, K.A. Observational evidence of slantwise convective adjustment. *Mon. Weather. Rev.*, **116**, 1805–1816, 1988.

[27] Fontane, J. & Dritschel, D.G. The hyper-CASL algorithm: a new approach to the numerical simulation of geophysical flows. *J. Comp. Phys.*, **228**, 6411-6425, 2009.

[28] Ford, R. The instability of an axisymmetric vortex with monotonic potential vorticity in rotating shallow water. *J. Fluid. Mech.*, **280**, 303-334, 1994.

[29] Ford, R., McIntyre, M.E. & Norton, W.A. Balance and the slow quasimanifold: some explicit results. *J. Atmos. Sci.*, **57**, 1236–1254, 2000.

[30] Galewsky, J., Scott, R.K. & Polvani, L.M. An initial-value problem for testing numerical models of the global shallow water equations. *Tellus*, **56A**, 429–440, 2004.

[31] Gill, A.E. *Atmosphere-Ocean Dynamics. Academic Press*, 1982.

[32] Holton, J.R. *An introduction to dynamic meteorology.* 4th Ed. *Elsevier Academic Press*, 2004.

[33] Hoskins, B.J. The role of potential vorticity in symmetric stability and instability. *Quart. J. Roy. Meteorl. Soc.*, **100**, 480–482, 1974.

[34] Hoskins, B.J., McIntyre, M.E. & Robertson, A.W. On the use and significance of isentropic potential-vorticity maps. *Quart. J. Roy. Meteorl. Soc.*, **111**, 877–946, 1985.

[35] Joly, A., Jorgensen, D., Shapiro, M.A., Thorpe, A., Bessemoulin, P., Browning, K.A., Cammas, J-P., Chalon, J-P., Clough, S.A., Emanuel, K.A., Eymard, L., Gall, R., Hildebrand, P.H., Langland, R.H., Lemaitre, Y., Lynch, P., Moore, J.A., Persson, P.O.G., Snyder, C. & Wakimoto, R.M. The fronts and Atlantic storm-track experiment (FASTEX): scientific objectives and experimental design. *Bull. Amer. Meteo. Soc.*, **78**, 1917-1940.

[36] Leith, C.E. Nonlinear normal mode initialisation and quasi-geostrophic theory. *J. Atmos. Sci.*, **37**, 958–968, 1980.

[37] McIntyre, M.E. & Norton, W.A. Potential vorticity inversion on a hemisphere. *J. Atmos. Sci.*, **57**, 1214–1235, 2000.

[38] McKiver, W.J. & Dritschel, D.G. Balance in non-hydrostatic rotating stratified turbulence. *J. Fluid. Mech.*, **596**, 201-219, 2008.

[39] McKiver, W.J. & Dritschel, D.G. Effect of Prandtl's ratio on balance in geophysical turbulence. *J. Fluid. Mech.*, (In Preparation) 2009.

[40] Mohebalhojeh, A.R., & Dritschel, D.G. On the representation of gravity waves in numerical models of the shallow water equations. *Quart. J. Roy. Meteorl. Soc.*, **126**, 669–688, 2000.

[41] Mohebalhojeh, A.R., & Dritschel, D.G. Hierarchies of balance conditions for the f-plane shallow water equations. *J. Atmos. Sci.*, **58**, 2411–2426, 2001.

[42] Mohebalhojeh, A.R., & Dritschel, D.G. Contour-advective semi-Lagrangian algorithms for many-layer primitive equation models. *Quart. J. Roy. Meteorl. Soc.*, **130**, 347–364, 2004.

[43] Mohebalhojeh, A.R., & Dritschel, D.G. Assessing the numerical accuracy of complex shallow water flows. *Mon. Weather. Rev.*, **135**, 3876–3894, 2007.

[44] Mohebalhojeh, A.R., & Dritschel, D.G. The diabatic contour-advective semi-Lagrangian algorithms for the spherical shallow water equations. *Mon. Weather. Rev.*, **137**, 2979–2994, 2009.

[45] Pedlosky, J. *Geophysical Fluid Dynamics. Springer*, 2004.

[46] Persson, A. & Grazzini, F. User Guide to ECMWF forecast products.

[47] Priestley, A. A quasi-conservative version of the semi-Lagrangian advection scheme. *Mon. Weather. Rev.*, **121**, 621-629, 1993.

[48] Proudman, J. On the motion of solids in a liquid possessing vorticity. *Proc. R. Soc. A.*, **92**, 408-424, 1916.

[49] Rawlins, F., Ballard, S.P., Bovis, K.J., Clayton, A.M., Li, D., Inverarity, G.W., Lorenc, A.C. & Payne, T.J. The Met Office global four-dimensional variational data assimilation scheme. *Quart. J. Roy. Meteorl. Soc.*, **133**, 347-363, 2007.

[50] Ritchie, H. Application of the semi-Lagrangian method to a spectral model of the shallow water equations. *Mon. Weather. Rev.*, **116**, 1587-1598, 1988.

[51] Rivest, C., Staniforth, A. & Robert, A. Spurious resonant response of semi-Lagrangian discretizations to orographic forcing: diagnosis and solution. *Mon. Weather Rev.*, **122**, 366–376, 1994.

[52] Robert, A. The integration of a low order form of the primitive meteorological equations. *J. Meteor. Soc. Japan*, **44**, 237-245, 1966.

[53] Schmetz, J., Pili, P., Tjemkes, S., Just, D., Kerkmann, J., Rota, S. & Ratier, A. An introduction to Meteosat second generation (MSG). *Bull. Amer. Meteo. Soc.*, 977-992, 2002

[54] Schultz, D.M. & Schumacher, P.N. The Use and misuse of conditional symmetric instability. *Mon. Weather Rev.*, **127**, 2709-2732, 1999.

[55] Smith, R.K. & Dritschel, D.G. Revisiting the Rossby-Haurwitz wave test case with contour advection. *J. Comp. Phys.*, **217**, 473–484, 2006.

[56] Staniforth, A., White, A., Wood, N., Thuburn, J., Zerroukat, M., Cordero, E., Davies, T. & Diamantakis, M. Joy of UM 6.3 - Model formulation. *Unified Model Documentation Paper No.15.*, 2006.

[57] Tanguay, M., Yakimiw, E., Ritchie, H. & Robert, A. Advantages of spatial averaging in semi-implicit semi-Lagrangian schemes. *Mon. Weather Rev.*, **114**, 113-123, 1992.

[58] Taylor, G.I. Experiments on the motion of solid bodies in rotating fluids. *Proc. R. Soc. A.*, **104**, 213-218, 1923.

[59] Temperton, C. & Staniforth, A. An efficient two-time-level semi-Lagrangian semi-implicit integration scheme. *Quart. J. Roy. Meteorl. Soc.*, **113**, 1025–1039, 1987.

[60] Vallis, G. *Atmospheric and oceanic fluid dynamics: fundamentals and large-scale circulation. Cambridge*, 2006.

[61] Viúdez, Á. & Dritschel, D.G. Vertical velocity in mesoscale geophysical flows. *J. Fluid. Mech.*, **483**, 199-223, 2003.

[62] Viúdez, Á. & Dritschel, D.G. Spontaneous generation of inertia–gravity wave packets by balanced geophysical flows. *J. Fluid. Mech.*, **553**, 107-117, 2006.

[63] White, A.A. A view of the equations of meteorological dynamics and various approximations. In *Large-scale atmosphere-ocean dynamics.* (J. Norbury & I. Roulstone, eds), **Vol.1**, 1–100, 2002.

[64] White, A.A., Hoskins, B.J., Roulstone, I. & Staniforth, A.A. Consistent approximate models of the atmosphere: shallow, deep, hydrostatic, quasi-hydrostatic and non-hydrostatic. *Quart. J. Roy. Meteorl. Soc.*, **131**, 2081–2107, 2005.